Guodong Zhan

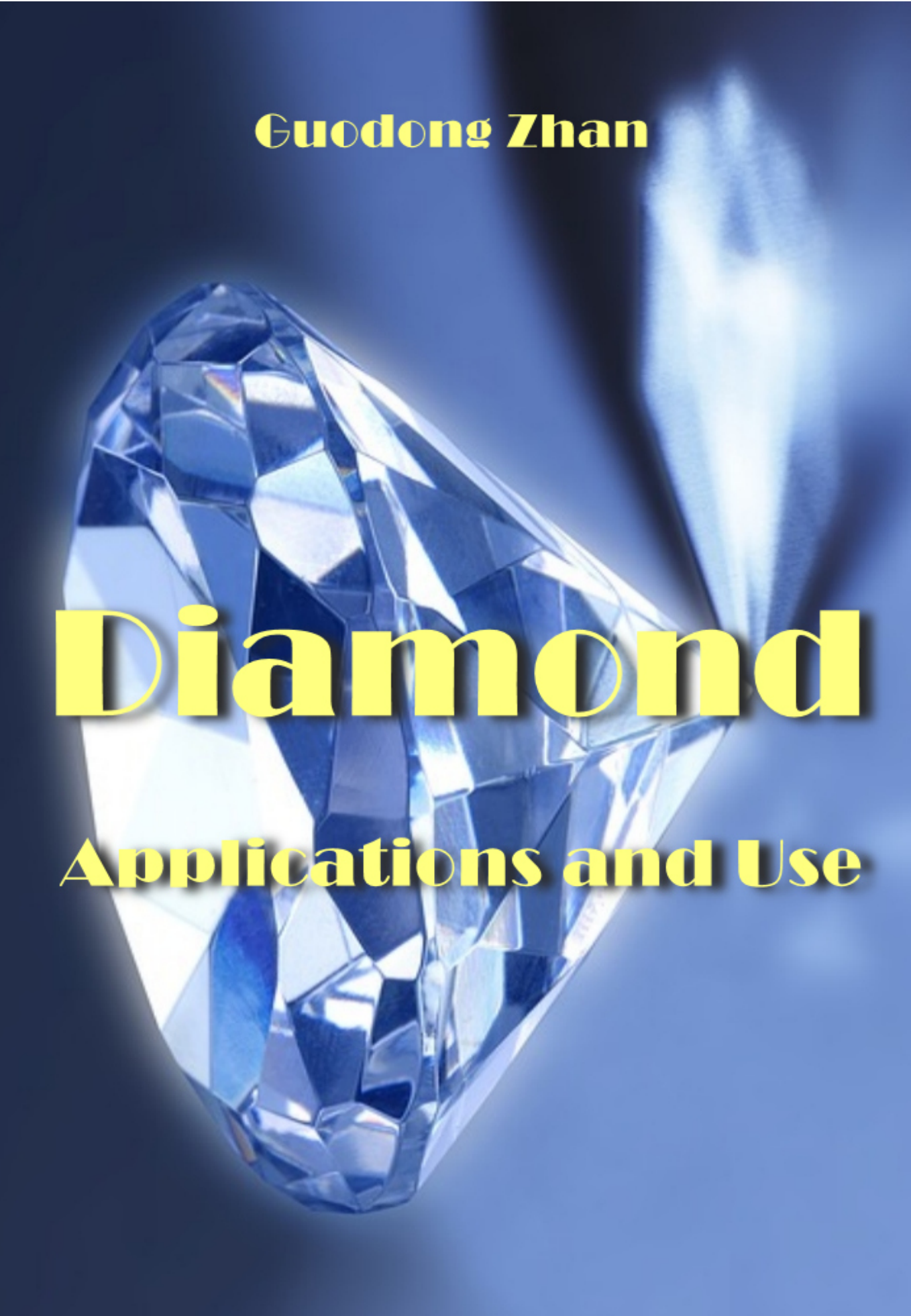

Diamond

Applications and Use

Chapter 1

Diamond as a Precision Cutting Tool

Anuj Sharma

Abstract

Ultra precision diamond turning is one of the advanced techniques to generate highly finished optical grade surfaces. The machining at nano scale requires extremely small material to be removed which poses a severe challenge on the cutting tool. At nanoscale, the material strength becomes multi fold and it becomes extremely difficult to remove the material. A machining rule is that the tool must be harder than the workpiece. Diamond is the hardest known natural material. Thus at nano scale, single crystal diamond is commonly used as a cutting tool to remove the unwanted material from the work-piece. There are different orientations of the diamond cutting tool which are utilized depending on the work-piece being machined. Although diamond is the hardest, still there are various challenges in machining different kinds of materials from metals to semiconductors. Diamond machined work-piece surfaces find applications in a range of sectors from energy sector to biomedical and defense to optics industries. The present chapter covers the various aspects of single crystal diamond tool in ultra- precision machining. Tool-workpiece material interaction, material removal mechanisms and tool wear are some of the issues which have been covered in detail.

Keywords: diamond turning, tool wear, cutting mechanism, precision machining, nanoscale machining, single crystal diamond, diamond tool

1. Introduction

Ultraprecision machining techniques have received much attention owing to the increasing demands for precision components with tight dimensional tolerance, high shape accuracies and excellent surface quality. Single point diamond turning (SPDT) or diamond turn machining is an ultraprecision machining technique used to generate the components with exceptional accuracy and surface finish [1]. The SPDT was first explored in 1960s with the need to advance in various fields such as defense, aerospace, computer, electronics and medical. In 1983, Taniguchi produced a plot which showed the evolution of machining accuracy with respect to every passing decade [2] and predicted the accuracy for the year 2000 as shown in **Figure 1**. After extrapolating, it indicated that the ultraprecision processes at micro/nanoscale would be able to achieve the machining accuracy of 0.01 μm. To achieve this extreme level of accuracy, the processing scale needs to be extremely small of the order of few nanometers, which in turn depends on the accuracies of the machine tool and

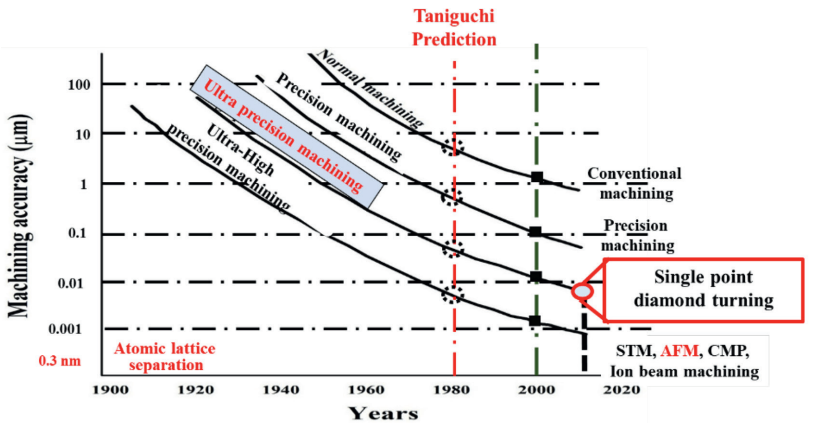

Figure 1.
Taniguchi prediction of machining accuracies [3].

cutting tool being used. Among the various mechanical micro/nano-scale machining processes, diamond turning technology has brought a revolution in the world of precision machining by achieving submicron level accuracies in the size and shape of the machined component. Other than the integrated technologies like granite bed, air bearing spindle, hydrostatic slide bearings, and optical linear scale feedback system in ultraprecision diamond turning technology, single crystal diamond tool is a key factor to obtain a high quality machined surface. Owing to its exceptional properties suitable for cutting tool, the single crystal diamond tool with edge sharpness of the order of nanometers is extensively used in ultraprecision machining.

Based on the material removal mechanisms, various manufacturing processes can be categorized into mechanical, physical and chemical processes (see **Figure 2**). The physical and chemical machining processes are limited to certain materials, mechanical machining processes can be applied to a variety of materials and applications. The mechanical based micro/nano machining processes are classified into mechanical tool based cutting and abrasive based machining. Mechanical tool based machining is deterministic in nature as the tool path can be controlled. Whereas abrasive based machining are force controlled and are random in nature. Size and shape control in abrasive machining are difficult to achieve through abrasive based machining processes. The cycle time is much higher in case of abrasive machining. Therefore, precision of the highest level in terms of size and shape control and surface finish is not achieved through abrasive based material removal process [4]. In addition, the cycle time is relatively higher [5].

Currently, the diamond turning is commonly used for various applications, as some examples are listed below:

- cylinders for video tape recorders
- substrates for magnetic discs in computers
- convex mirrors for high output carbon dioxide laser resonators
- infra-red lenses of germanium for thermal imaging systems

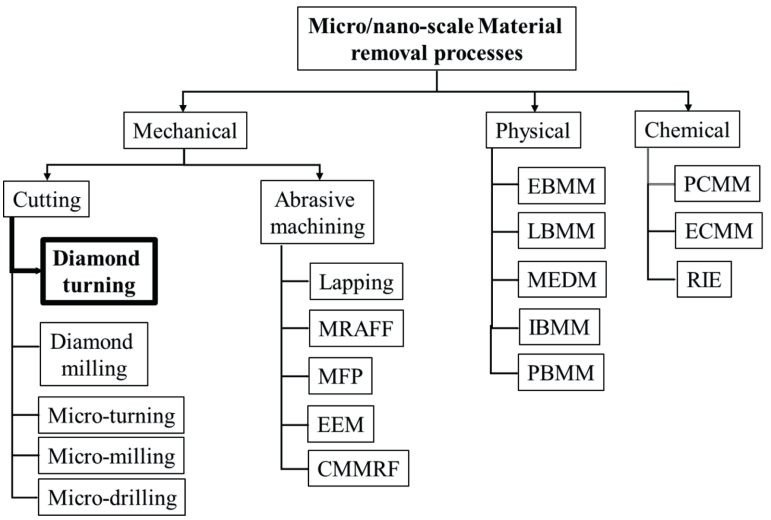

Figure 2.
Classification of various micro/nano scale manufacturing processes. {MRAFF: Magneto-rheological abrasive flow finishing; MFP: Magnetic float polishing; EEM: Elastic emission machining; EBMM: Electron beam micromachining; LBMM: Laser beam micromachining; MEDM: Micro electric discharge machining; IBMM: Ion beam micromachining; PBM: Plasma beam micromachining; PCMM: Photo chemical micro-machining; ECMM: Electro chemical micro-machining; RIE: Reactive ion etching}.

- Contact lenses for human vision
- scanners for laser printers and drums for photo copiers
- elliptical mirrors for YAG (yttrium aluminum garnet) laser beam collectors
- X-ray and ultraviolet optics
- molds for Compact Disc lenses
- AIRS for missile guidance system
- Aircraft windscreens
- Computer disk; photocopying application

Single crystal diamond tool is used in ultraprecision diamond turning of nonferrous materials because of its ability to maintain an extremely sharp cutting edge owing to its wear resistance property. Single crystal diamond tool has a round nose with rake angle ranging from 0^{o} to highly negative and suitable clearance angle (see **Figure 3(a)**) enough to avoid the contact between clearance face and the machined surface. The tool consists of sharp edge with controlled waviness (< 1 μm) along whole edge. The cutting edge radius is in the order of tens of nanometers. The performance of single crystal diamond tools depends on the quality of the diamond, its crystal orientation, edge radius/sharpness (see **Figure 3(b)**), and edge irregularities (see **Figure 3(c)**). Among these, measurement of tool edge radius is a challenge due to the fact that the tool edge is extremely sharp.

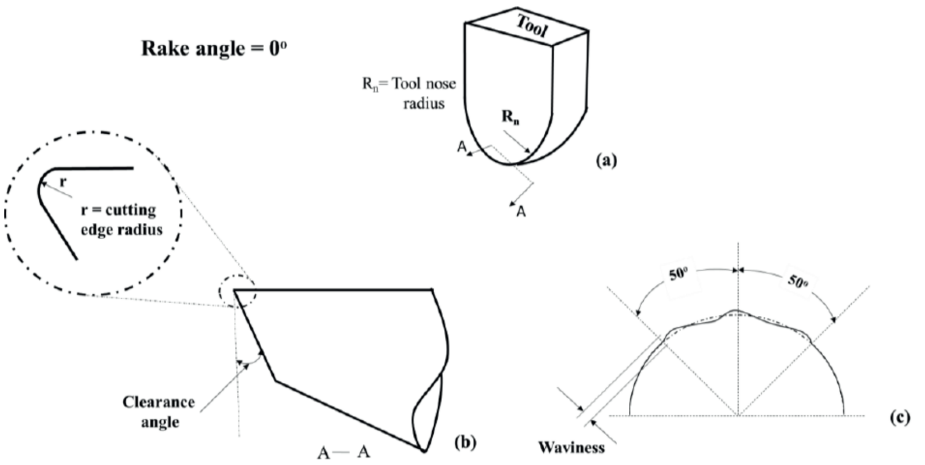

Figure 3.
Cutting tool edge geometry.

Asai et al. [6] put forward a measurement technique for diamond tool edge sharpness. They advanced the conventional SEM by employing two secondary electron detectors. The signals from these detectors are processed to produce the fine cutting edge. This method of measurement is efficient for diamond tool with edge radius of 45 nm or less. Yuan et al. [7] performed experimental investigations on different orientations of single crystal diamond tool to find out the optimum crystal plane for ultraprecision machining. They conducted the friction tests on rake and flank face of the tool, noticed the friction coefficients and observed the effect on shear deformation, tool wear and the machined surface quality. Based on the friction coefficients value on different directions of crystal orientation of (100), (110) and (111), it was found that the (100) plane shows highest anisotropy. The literature has contradictions regarding the optimum crystal planes for the rake and flank surface of the diamond tool.

Ultraprecision machining trials including the shear deformation, tool wear and surface quality has indicated that the (100) plane is most suitable for rake as well as flank surfaces. However, Uddin et al. [8] recommended (100) as rake plane and {110} as flank plane for the diamond tool in machining of Si. With theoretical calculations, Zong et al. [9] proposed that it is possible to achieve 1 nm sharp cutting edge radius for the (110){100} crystal orientation.

2. Structure of diamond

In ultra-precision and nanometric cutting operations, the most preferred tool material is single-crystal diamond due to its extraordinary properties, including highest hardness, very strong resistance to wear, perfect chemical stability and satisfactory service life, as well as the least sharpness, when finished. Due to its extreme strength and hardness, recently diamond has become an attractive choice in engineering processes and in a variety of other technological applications. Considering the morphology and structure of diamond, its mechanical and physical properties vary not only with the different crystallographic planes but also with different crystallographic directions on a plane.

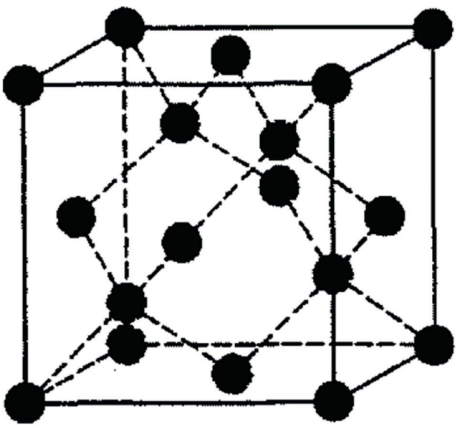

Figure 4.
Crystal structure of single crystal diamond.

Diamond is a crystal allotropic form of Carbon and has diamond cubic crystal structure with a lattice parameter of 0.3567 nm (see **Figure 4**). Each C atom has four neighboring C atoms in a tetrahedron structure with bond angle between the atoms of 109°28′. The C atoms are covalently bonded together with sharing of one of its outer four electrons with each of four other C atoms resulting in sp^3 hybridization. This sharing of electrons results in a strong binding among each pair of C atoms in all three dimensions.

Diamond has some outstanding properties which makes it an obvious choice for the cutting tool material.

i. It is the hardest known natural material and hardest among cutting tool materials (see **Figure 5**).

ii. It possesses extreme strength and stiffness.

iii. It has highest atom-number density.

iv. At room temperature, it has highest thermal conductivity of any solid.

Table 1 shows the mechanical properties of diamond. Diamond is categorized into four categories:

i. Natural Diamond

ii. Synthetic diamond

iii. CVD diamond

iv. Diamond like Carbon (DLC)

Diamond naturally occurs produced in nature at high pressure and temperature in volcanic shafts. With high pressure synthesis, it is able to produce diamond possessing the strength similar to natural diamond. Generally, the natural and synthetic diamond are used for cutting purposes. Diamonds usually exist with other allotropes

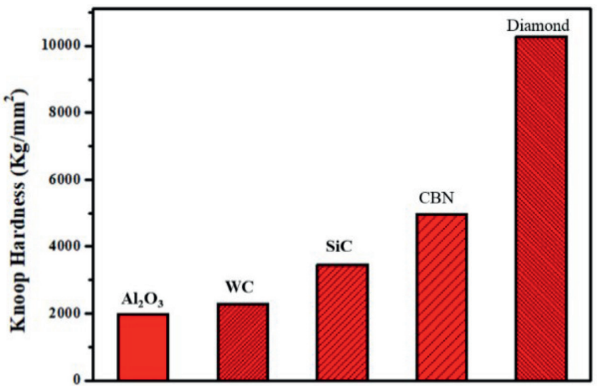

Figure 5.
Hardness of various tooling materials.

Property	Values
Density, (kg/m^3)	3520
Elastic Modulus (GPa)	910–1250
Compressive Strength (GPa)	8.68–16.53
Knoop hardness, (Kg/mm^2)	5700–10,400 (Overall) 7500–10,400 (111 plane) 6900–9600 (100 plane)
Poisson's ratio	0.07–0.16
Diamond-on-diamond Friction coefficient	0.05–0.15 (in air) ~1 (in vacuum)

Table 1.
Mechanical properties of diamond.

of carbon and they can be characterized by knowing the structure, atomic vibration and electronic states. The diamond characteristics are usually determined using X-ray diffraction, electron microscopy and Raman spectroscopy. For diamond to be qualified, it must have the following characteristics:

i. A crystalline morphology revealed by electron microscopy

ii. Crystalline structure with a single phase identified by X-ray diffraction

iii. A sharp peak at 1332 cm^{-1} detected by Raman spectrum

Diamond occurs predominantly in three different forms in cubic (100), octahedron (111) and dodecahedron (110) and their combinations. These three forms are based on the three planes ((100), (110) and (111)) from a simple cubic crystal structure. **Figure 6** shows the schematic of the (100) cubic, the (110) dodecahedral and the (111) octahedral. The octahedral form of diamond crystal is the most common form.

Diamond breaks along {111} crystal planes also known as cleavage planes. Bonding is less strong perpendicular to these planes as compared to the other directions due to lower total number of bonds and hence the diamond fractures favorably along

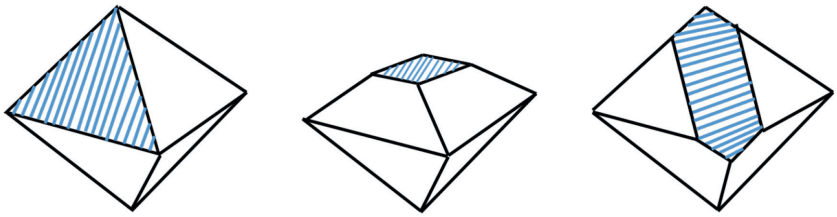

Figure 6.
Schematic diagrams showing the location of {111}, {100} and {110} planes on an octahedron diamond.

Element	Type I		Type II	
	a	b	a	b
Nitrogen (ppm)	200–2400	40	8–40	5–40
Boron (ppm)	Nil	Nil	Nil	0.5
Occurrence of atoms in:	clusters	Isolation atoms	Very little	Considerable boron

Table 2.
Diamond classification based on impurity level [10].

these planes. Diamonds are also categorized into four types based on the presence of nitrogen as an impurity in their crystals. These are: Ia, Ib, IIa, IIb. Majority of natural diamonds (~99%) come in type Ia. Type Ia consists of nitrogen in the form of aggregates in the crystal. All synthetic diamonds are of type Ib with an even distribution of nitrogen atoms in the crystal. Types IIa and IIb are very rare in nature but can be synthesized for industrial purposes. In all natural diamonds, there exist many impurity elements such as nitrogen, hydrogen, boron and oxygen. **Table 2** shows different classifications of diamond.

3. Fabrication of diamond tools

Predominantly there are two methods used for fabrication of single crystal diamond tools. The diamond tool fabrication is performed in such a way that the tool edge radius is maintained in the order of nanometers and a very smooth rake and flank surface are generated. These methods include mechanical lapping, thermochemical polishing, polishing with ion beam, damage-free tribochemical polishing, chemical-assisted mechanical polishing and planarization, chemical polishing with plasma, oxidative etching, and laser ablation.

Mechanical lapping is the most conventional and popular method to mechanically polish the single crystal diamond. Various mechanisms have been proposed in different studies such as: 1) Micro-cleavage or fracture along the (111) plane; 2) thermal wear; 3) Burnout or carbonization will take place at elevated temperature; 4) fracture or micro-chip in hard direction and plastic deformed layer in soft direction; 5) diamond phase transformation; 6) Plastic deformation as a result of brittle-ductile transition. Mechanical lapping is the simplest and most cost effective process method which enables to reach a cutting edge radius of about 70–80 nm [11]. It is

very challenging task to manufacture a diamond tool with cutting edge radius smaller than 50 nm. In order to produce very fine cutting edge profile for diamond tool, it is very important to understand the material removal mechanism in lapping of the diamond cutting tool. It will help in optimizing and help controlling the cutting edge sharpness.

Zong et al. [12] put forward the brittle–ductile transition theory to indicate the material removal nature in lapping of diamond surface layer. It explains that plastic deformation is responsible for the dominant removal mode of the lapped surface layer of the single crystal diamond in both the soft and hard directions on the diamond crystal planes. Plastic deformation in diamond crystal takes place when the embedding depth of diamond grit into the lapped surface layer is less than the corresponding critical depth of the cut, which leads to brittle–ductile transition.

In mechanical lapping, control of contact accuracy is extremely important between the high speed rotating scaife and lapped diamond tool. Accurately controlling the contact helps in better cutting edge sharpness. Lapping set-up is shown by schematic in **Figure 7**. The set up consists of cast iron scaife mounted on air bearing. Diamond tool is placed against the rotating cast iron scaife. Speed of cast iron scaife can be varied from 300 to 3000 rpm. Diamond grits of approximate size of 0.5 μm are used in the scaife for lapping. The relative velocity between scaife and the tool face is approx. 30 m/s. The contact accuracy should be ensured otherwise there will be impacts on the cutting edge and subsequent damages the cutting edge sharpness. Since the variations of the external load will change the number of grits in contact. In fact, only the material removal rate will change, and the mean force of single grit has almost no variations. So the changes of external applied load result in minute influence on the maximal groove depth left on lapped surfaces and are ignored in all experiments. Other variants of lapping are thermo-mechanical lapping, thermo-chemical polishing and chemically assisted mechanical lapping etc. which can also be employed to fabricate diamond tool.

In mechanical lapping, the removal rate takes place in the nanometric level that results in a sharp cutting edge radius ranging from 35 nm to 50 nm. Another common variant of the lapping of diamond tools is thermo-mechanical lapping [13]. Thermo-mechanical lapping is a development over mechanical lapping by using steel scaife in

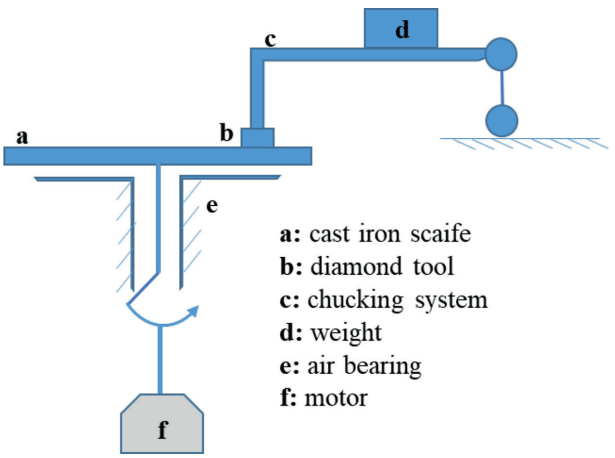

Figure 7.
Schematic representation of the lapping set up [11].

place of cast iron scaife. In thermo-mechanical lapping, material removal mechanisms of diamond are diffusion, graphitization and oxidization. Dominant mechanism is governed by the interface temperature which in turn depends on the lapping compression force and sliding velocity. At low temperature, the dominant mechanism is diffusion of C atoms into the iron matrix. With higher temperature, C atoms from the diamond cubic lattice structure forms dangling bonds and leads to graphitization. On further increased temperatures, oxidization of diamond carbon atoms takes place. The formation of carbon monoxide or dioxide consumes more energy. These deteriorated atomic structures from different mechanisms at different range of temperatures are further worn by the abrasion from the rotating scaife. The material removal rate is in atomic level and thus a highly sharp cutting edge radius of 10 nm or less can be achieved. Considering the machining efficiency and production cost, the mechanical lapping and thermo-mechanical lapping are the best choice to fabricate nanoprecision diamond cutting tools.

4. Mechanisms of material removal in ultraprecision machining with diamond tool

Ultraprecision machining is achieved by reducing the scale of machining process which in turn brings the "size effect" into picture. Difference between conventional machining and ultraprecision machining lies in the ratio of uncut chip thickness and edge radius (see **Figure 8**). Unlike conventional machining process, diamond turning process with a highly sharp single crystal diamond tool exhibits the size effect due to its reduced scale of material removal. Cutting tool edge radius (r) becomes significant with respect to uncut chip thickness during diamond turning process (see **Figure 8(b)**). Resisting shear strength of the material increases considerably as the chip thickness is reduced.

At the macroscale in conventional cutting, while the uncut chip thickness is larger than the tool edge radius, the tool is able to remove cluster of grains. The shearing action takes place along the easy slip plane. The easy slip plane is governed by the stress concentration along the grain boundaries, defects and vacancies in the material. When the uncut chip thickness is reduced from few microns to a few nanometers, cutting within a grain takes place. It requires more energy to cut the solid grain with round edge than to remove a number of grains with sharp edge tool (see **Figure 9**). Therefore, the specific energy is higher in the ultraprecision machining process like

$$r_2 \gg r_1 \;\&\; t_2 \ll t_1$$

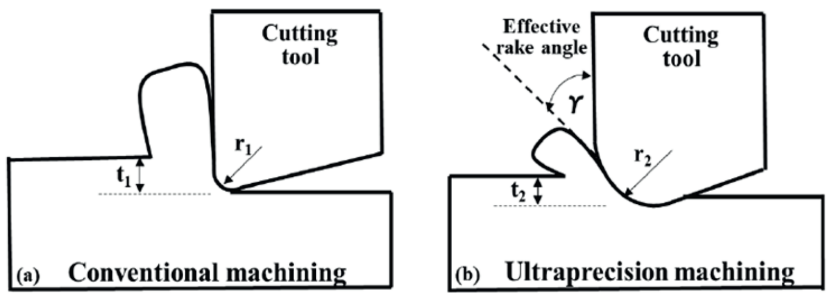

Figure 8.
Schematic of (a) conventional and (b) ultraprecision machining [3].

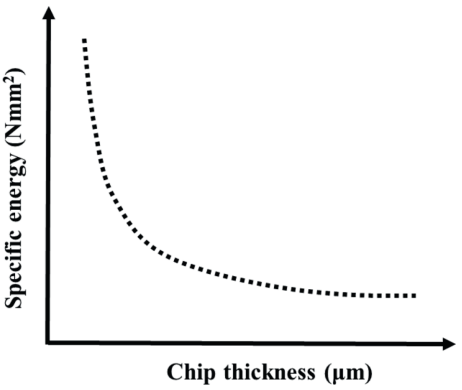

Figure 9.
Size effect in ultraprecision machining.

diamond turning compared to the conventional cutting. With the reduction in chip thickness up to few nano meters, plastic deformation viz. rubbing and burnishing become more dominant than cutting due to very small effective cutting zone. In diamond turning, the tool edge radius is continuously deteriorated and increased with constant uncut chip thickness, which in turn deteriorates the machining process.

5. Cutting mechanism and material deformation in diamond turning

The cutting edge radius of the diamond tool in ultraprecision machining affects the cutting mechanisms. The uncut chip thickness (a) is of usually comparable size as the tool edge radius (r) in diamond turning and their ratio governs the cutting mechanism viz. shear plane cutting, plowing and sliding. These mechanisms in turn decides the resulting surface quality. There exists a 'minimum uncut chip thickness' below which no material removal takes place due to cutting. The minimum uncut chip thickness depends on the tool geometry which includes edge radius, rake & flank plane angle and the workpiece material properties. Sliding at the flank face due to elastic recovery of the workpiece material and plowing due to edge radius of the tool becomes dominant in ultraprecision machining.

5.1 Ductile machining

Figure 10 shows the chip formation and various regions along the chip profile in ultraprecision diamond turning. In the chip profile, ratio of uncut chip thickness (a) to toll edge radius (r) varies from zero to some maximum value. The cutting mechanisms vary with different regions of a/r ratios. At a/r ratio sufficiently higher than 1 (region III), maximum amount of material removal takes place along the rake face of the tool and thus facilitates pure cutting. As a/r ratio approaches to 1 (region II), the tool edge radius and uncut chip thickness become comparable which makes the effective rake angle of the tool negative. The negative rake angle leads to extrusion like squeezing action. As a/r ratio becomes less than 1 (region I), the tool is unable to remove the material as a chip and only sliding and elastic deformation takes place.

As the uncut chip thickness is decreased thrust force increases in comparison to the cutting force and mechanisms like plowing, rubbing and burnishing become

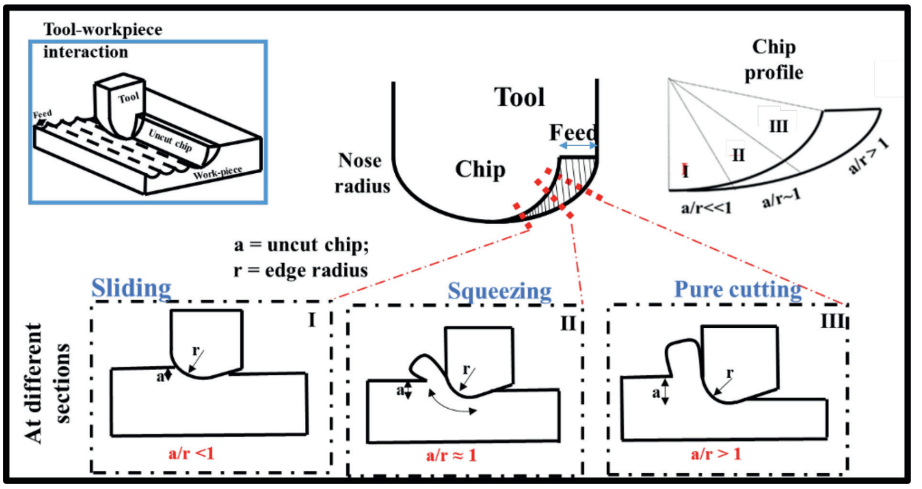

Figure 10.
Cutting mechanism along the chip profile for the workpiece machined with round nose diamond tool.

dominant. This is because as the chip thickness is reduced, the tool edge radius becomes significant in comparison to chip thickness and the effective rake angle thus becomes negative. Higher negative rake angle restricts the chip to flow along rake face and therefore the chip flows sideways of the tool. It can be described as tool plows through the workpiece. Further reduction on the uncut chip thickness causes the tool to rub or burnish the work surface. The mechanism of material removal in diamond turning, thus, primarily depends upon the uncut chip thickness and tool edge radius. Since, the uncut chip thickness along the chip profile varies, the mechanisms tend to vary along it. The tool edge sharpness also degrades during the course of machining, which also affects the cutting mechanisms.

5.2 Ductile regime machining of brittle materials

In conventional macroscale machining process, the brittle materials are subjected to fracture as a result of median and lateral cracks [14] as shown in **Figure 11**. This brittle failure can be prevented using a very low uncut chip thickness. Machining of brittle materials takes place in ductile mode at very low uncut chip thickness and therefore it is known as ductile regime machining. Ductile regime machining of brittle materials leads to crack-free mirror finished surfaces. In case of brittle materials, there exists a critical uncut chip thickness below which ductile regime machining takes place and above which the brittle machining takes place. Blackley and Scattergood [15] proposed a machining model depending on critical depth of cut and subsurface damage depth which indicated that fracture takes place above the critical uncut chip thickness (d_c) and is subsequently propagated in the workpiece material. The chip thickness varies from zero at the tool centre to a maximum at the top of the uncut portion as shown in **Figure 11**. If the fracture does not penetrate into the cutting plane, the brittle mode machining will take place. Thus the critical chip thickness is a deciding parameter between the two machining modes.

Smooth, damage free and optical quality surface is generated if the uncut chip thickness along the tool nose is below critical chip thickness. This transition of mechanism from brittle to ductile machining is also known as brittle - ductile transition. According

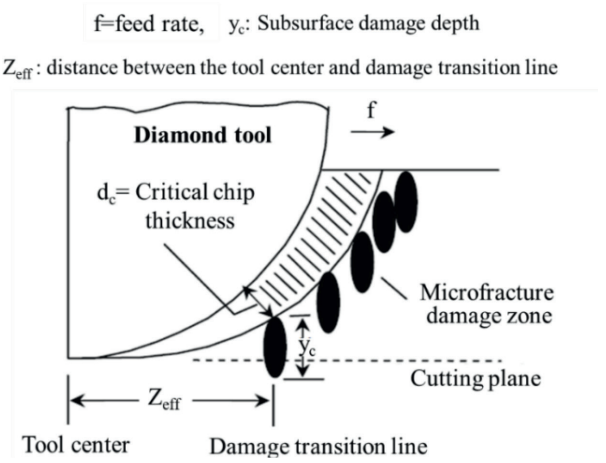

Figure 11.
Schematic of brittle and ductile regime machining in brittle materials [15].

to another ductile regime machining model proposed by Nakasuji et al. [16], the brittle to ductile transition takes place from in the diamond turning process of brittle materials. For the larger uncut chip thickness, the stress zone is such that it contains a number of defects which nucleate to expand the cracks and cause brittle fracture. With the extremely small uncut chip thickness, the defects are too less in the stress zone to form cracks and therefore, it enables the material removal in ductile mode (see **Figure 12**).

Shimada et al. [17] used a different model to elaborate the brittle-ductile transition and suggested that there are two ways of material removal: one is the ductile machining due to plastic deformation in the slip direction on the characteristic slip plane and the other is the brittle mode machining owing to cleavage fracture on the characteristic cleavage plane. When the resolved shear stress τ_{slip} in the slip direction on the slip plane exceeds a certain critical value τ_c inherent to the workpiece material, plastic deformation occurs in a small stressed field in the cutting region of a specified scale. On the other hand, a cleavage occurs when the resolved tensile stress normal to the cleavage plane σ_{cleav} exceeds a certain critical value σ_c. The mode of material removal depends on which criteria dominates or precedes $\tau_{slip} > \tau_c$ or $\sigma_{cleave} > \sigma_c$ for the stress state under a particular machining condition (see **Figure 13**).

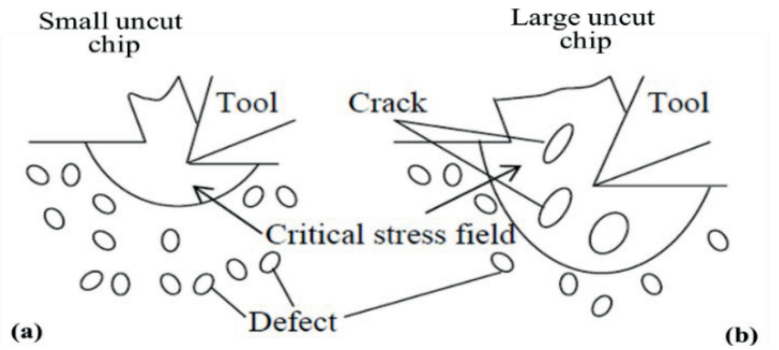

Figure 12.
Model of chip removal with a size effect in terms of defects distribution [16].

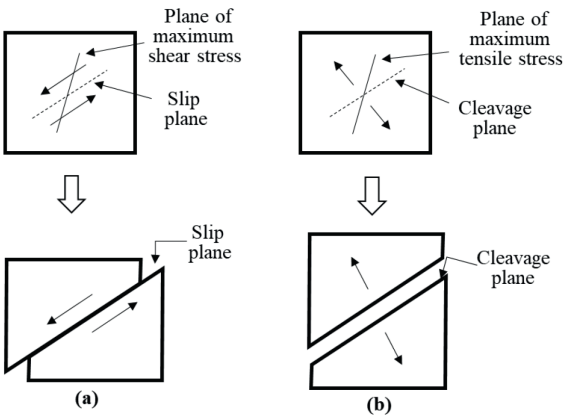

Figure 13.
Ductile and brittle regime models of chip removal [17].

6. Diamond tool and workpiece material interactions during machining

With the tool wear, the cutting edge radius at every section of the tool edge interacting with the work material increases and it changes the a/r ratio which in turn shifts the range of these regions. Therefore, it is not only the chip thickness which varies along the chip profile but the tool edge radius also continuously changes with increasing tool wear. **Figure 14(a-d)** shows a schematic which shows the variation in cutting edge sharpness (r) at any uncut chip thickness (a) as the tool wear takes place. **Figure 14(b-d)** shows the condition of tool edge at three different stages of tool wear. In initial cutting stages when the tool is fresh, it possesses a sharp cutting edge with a very small radius (r_1) for an uncut chip thickness '*a*' as shown in **Figure 14(b)**. During the intermediate stages of cutting, as the tool wears and the edge becomes blunt, the cutting edge radius increases from 'r_1' to 'r_2' as shown in **Figure 14(c)**. The increased edge radius causes a decrease in the a/r ratio. This is a stage where uncut chip thickness and edge radius become approximately comparable i.e. a/r ~ 1 at that section. With a further increase in cutting edge radius from 'r_2' to 'r_3', the a/r ratio decreases to

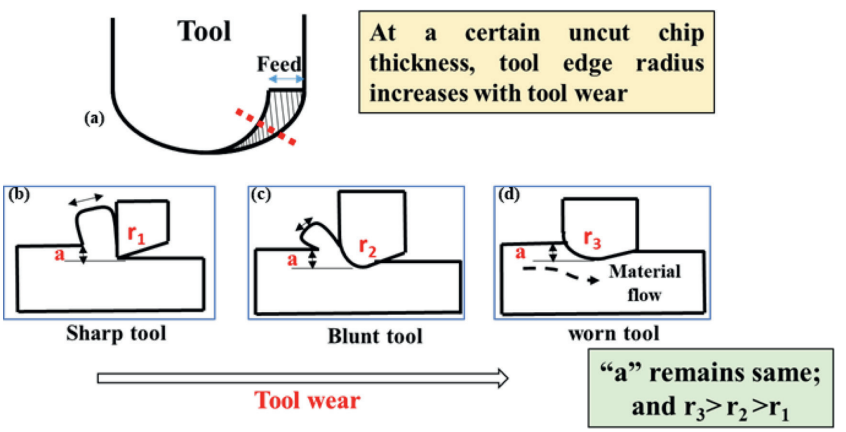

Figure 14.
Schematic of tool edge condition and cutting mechanism with tool wear [3].

a value less than 1. The material removal becomes difficult and thereby no chips are removed from the workpiece material at the final stages of cutting (**Figure 14** (**d**)).

6.1 Wear characteristics of the diamond tool

Tool wear influences the cutting forces, chip formation and the surface roughness. Tool wear in diamond turning of ductile and non-ferrous materials is considerably low whereas it is very high in case of hard and brittle materials. Wear on the diamond tool deteriorate the machined surface quality. In general, flank wear is observed to be the most dominant wear in single crystal diamond tool. There are various effects of the tool wear on the machining parameters which are concluded in **Table 3**.

Tool wear in machining vary depending upon the tool and workpiece material combination. In ultraprecision diamond turning, the tool being used is diamond, and the workpiece material is the solely responsible for change in mechanisms. Diamond tool wear is different for different class of materials. In machining the class of materials are categorized in easy to machine and difficult to machine materials. The easy to machine materials are Al, Cu, brass, and Al & Cu alloys. For instance, the single crystal diamond tool is very useful in machining nonferrous and easy to cut materials such as aluminum, copper, gold, brass, electroless Nickel and plastics. In these materials, diamond tool does not wear out for a few hundreds of kilometers of cutting distance and still achieves a surface finish in the order of few nanometers. In these materials, diamond tool wear out slowly and abrasive wear take place more predominantly. The wear mechanisms become complicated while machining difficult to cut materials. The wear pattern consists of crater and flank wear. Impurities in alloys causes initial microchipping on the tool edge. The dominant wear mechanism in easy to machine materials is abrasive type. **Table 4** shows the wear pattern and wear mechanisms for easy to machine materials in diamond turning.

Wear mechanism of a single crystal diamond tool is highly complicated which may involve one or multiple mechanism types. These can be chemical, physical, thermal and mechanical interactions between the diamond tool and the workpiece. Depending on the tool and workpiece material combination, the wear mechanisms can vary. Diamond tool wear can be characterized into mechanical, chemical and physical wear. Mechanical wear comprise of abrasive wear, fatigue, and adhesive

No.	Parameters	Effects
1	Surface roughness	Increases
2	Form error	Increases
3	Force	Increases
4	Mechanism	Increases
5	Chip thickness	Decreases
6	Brittle to ductile transition	Increases
7	Surface quality	Decreases
8	Material properties	Decreases
9	Plowing/side flow	Increases

Table 3.
Effect of tool wear on various parameters [18].

Materials	Wear patterns	Mechanisms / Causes
Aluminum	Flank wear Crater wear	Mechanical abrasion
Copper	Flank wear Crater wear	Mechanical abrasion
Al alloy	Flank wear Crater wear Microchiping	• Mechanical abrasion • Impurities
Al359	Flank wear	Abrasive wear
RSA 905	Flank wear Crater wear	• Abrasion • Thermo-chemical erosion
Cu-Cr-Zr	Chipping Grooving	• Mechanical abrasion • Thermo-chemical wear

Table 4.
Wear patterns and mechanisms in easy to cut materials [18].

wear. Chemical wear includes chemical reaction, graphitization, amorphization, and diffusion. Physical wear is comprised of thermo-chemical wear, tribo-electric wear, anisotropy, and defect.

6.2 Wear mechanism in difficult-to-machine materials with diamond tool

When it comes to cutting difficult to machine materials with diamond tool, ferrous materials are first among several. Diamond turned ferrous materials are generally used

Materials	Wear pattern	Mechanisms / Cause
Si	Chipping Microcracking Micro/nanogrooves	SiC Formation Abrasion Thermochemical wear Graphitization Diffusion
SiC	Grooves	Abrasion Graphitization
Titanium	Micro-Chipping Flank wear	Graphitization Adhesion
Copper beryllium	Micro-Chipping Flank wear	Abrasion Amorphization
Glass	Uniform wear Micro grooves	Thermochemical wear Diffusion Abrasive wear
Steel	Ridges Grooves	Chemical wear Diffusion Abrasion Graphitization

Table 5.
Wear patterns and mechanisms in difficult to machine materials [18].

as precision dies and molds. The other class of materials are glass, crystal materials like silicon, silicon carbide, germanium, selenide, and zinc sulfide. Rapid tool wear rate limits the diamond turning applications in machining of difficult to machine materials. In machining ferrous metals for high precise and complex surfaces, diamond tools are subject to catastrophic wear, which subsequently downgrades surface quality. The diamond tool wear rate is very high in case of machining ferrous materials and it is 10,000 times higher than that in case of machining brass [19].

In difficult to machine materials, the wear pattern is flank wear assisted with micro/nano grooves. Initially the microchipping is also observed. In Difficult to machine materials dominant wear mechanism is chemical wear based on the interface temperature. The interface temperature decides the type of wear mechanism which is predominantly categorized into diffusion, graphitization and oxidation. **Table 5** shows the wear pattern and wear mechanisms for difficult to machine materials in diamond turning.

7. Conclusions

In this chapter, the application of diamond tool in ultraprecision machining has been covered. The chapter highlights the applicability of single crystal diamond tool in ultraprecision machining. The cutting mechanisms are explained for both ductile and brittle materials. The tool wear mechanisms are elaborated for different class of materials. Following conclusions can be drawn from the chapter:

i. Single crystal diamond tool is the best cutting tool in terms of hardness, strength and wear resistance for ultraprecision machining.

ii. In ultraprecision machining with the diamond tool, the material removal mechanism varies from pure cutting to plowing and then sliding depending upon the ratio of uncut chip thickness to cutting edge radius. In brittle materials, there is brittle to ductile transition when the uncut chip thickness is below the critical chip thickness.

iii. Tool wear mechanisms are distinct for different class of materials. In case of easy to machine materials, the dominant mechanism is abrasion, whereas in case of difficult to machine materials, the dominant wear mechanism is chemical which could be diffusion, graphitization and oxidation.

Acknowledgements

Author would like to thank his supervisor during Ph.D. 'Dr. R. Balasubramaniam' from BARC Mumbai, under whom the knowledge in ultraprecision machining and single crystal diamond tool was gained.

Conflict of interest

The author declares no conflict of interest.

Diamond as a Precision Cutting Tool
DOI: http://dx.doi.org/10.5772/.108557

References

[1] Balasubramaniam R, Sarepaka RV, Subbiah S. Diamond Turn Machining: Theory and Practice. Boca Raton, Florida: CRC Press; 2017

[2] Goel S, Luo XC, Agrawal A, Reuben RL. Diamond machining of silicon: A review of advances in molecular dynamics simulation. International Journal of Machine Tools and Manufacture. 2015;**88**:131-164. DOI: 10.1016/j.ijmachtools.2014.09.013

[3] Sharma A. Numerical and Experimental Investigations of Tool-Workpiece Interaction in Diamond Turning of Copper Beryllium. Mumbai, India: Homi Bhabha National Institute; 2019

[4] Brehm PD. Single point diamond machining As an optical manufacturing process. In: Optical Specifications: Components and Systems. Vol. 406. SPIE; 1983. pp. 92-97

[5] Gerth HL. Introduction to precision machining of metal optics. In: Reflecting Opt. Synchrotron radiation. Vol. 315. SPIE; 1982. pp. 225-230

[6] Asai S, Taguchi Y, Horio K, Kasai T, Kobayashi A. Measuring the very small cutting-edge radius for a diamond tool using a new kind of sem having two detectors. CIRP annals. 1990;**39**(1):85-88

[7] Yuan ZJ, He JC, Yao YX. The optimum crystal plane of natural diamond tool for precision machining. CIRP annals. 1992;**41**(1):605-608

[8] Uddin MS, Seah KHW, Li XP, Rahman M, Liy K. Effect of crystallographic orientation on wear of diamond tools for nano-scale ductile cutting of silicon. Wear. 2004;**257**:751-759. DOI: 10.1016/j.wear.2004.03.012

[9] Zong WJ, Sun T, Li D, Cheng K, Liang YC. XPS analysis of the groove wearing marks on flank face of diamond tool in nanometric cutting of silicon wafer. International Journal of Machine Tools and Manufacture. 2008;**48**:1678-1687. DOI: 10.1016/j.ijmachtools.2008.06.008

[10] Pierson HO. Handbook of Carbon, Graphite, Diamonds and Fullerenes: Properties, Processing and Applications. Norwich, NY: William Andrew; 1993. ISBN 978-0-8155-1339-1

[11] Zong WJ, Li D, Cheng K, Sun T, Wang HX, Liang YC. The material removal mechanism in mechanical lapping of diamond cutting tools. International Journal of Machine Tools and Manufacture. 2005;**45**:783-788. DOI: 10.1016/j.ijmachtools.2004.11.014

[12] Zong WJ, Li D, Sun T, Cheng K. Contact accuracy and orientations affecting the lapped tool sharpness of diamond cutting tools by mechanical lapping. Diamond and Related Materials. 2006;**15**:1424-1433. DOI: 10.1016/j.diamond.2005.10.066

[13] Zong WJ, Li D, Sun T, Cheng K, Liang YC. The ultimate sharpness of single-crystal diamond cutting tools—Part II: A novel efficient lapping process. International Journal of Machine Tools and Manufacture. 2007;**47**:864-871

[14] Komanduri R, Chandrasekaran N, Raff LM. Effect of tool geometry in nanometric cutting: A molecular dynamics simulation approach. Wear. 1998;**219**:84-97. DOI: 10.1016/S0043-1648(98)00229-4

[15] Blackley WS, Scattergood RO. Ductile-regime machining model for diamond turning of brittle materials. Precision Engineering. 1991;**13**:95-103. DOI: 10.1016/0141-6359(91)90500-I

[16] Nakasuji T, Kodera S, Hara S, Ikawa N. Diamond turning of brittle materials for optical components. Pdf. CIRP Annals - Manufacturing Technology. 1990;**39**:89-92

[17] Shimada S, Ikawa N, Inamura T, Takezawa N, Ohmori H, Sata T. Brittle-ductile transition phenomena in microindentation and micromachining. CIRP Annals - Manufacturing Technology. 1995;**44**:523-526. DOI: 10.1016/S0007-8506(07)62377-4

[18] Zhang SJ, To S, Zhang GQ. Diamond tool wear in ultra-precision machining. The International Journal of Advanced Manufacturing Technology. 2016;**88**(1):613-641

[19] Thornton AG, Wilks J. Clean surface reactions between diamond and steel. Nature. 1978;**274**:792-793

Chapter 2

Applications of Polycrystalline Diamond (PCD) Materials in Oil and Gas Industry

Guodong (David) Zhan, Jianhui Xu and Duanwei He

Abstract

Polycrystalline diamond possesses high hardness and wear resistance, among other superior properties, such as low coefficient of friction, high thermal conductivity, high corrosion resistance and low electrical conductivity. Some of these properties favor the application of polycrystalline diamond in oil & gas industry. PDC cutters are the primary and key components in the PDC drill bits to cut various formations. However, drilling very hard and highly abrasive formations poses a big challenge for today's PDC drill bits. The weakness in the current technology is due to the unavoidable use of metallic catalysts to bond the diamond grains that comprise the PDC cutters in traditional high-pressure and high-temperature (HPHT) manufacturing. Development of catalyst-free PDC cutters would be a game changing technology for drill bits to potentially realize the goal of "One Run to Total Depth" in drilling technology. This chapter will cover the development and applications of both catalyst-synthesized and catalyst-free polycrystalline diamonds in oil and gas industry including latest breakthrough on ultra-HPHT manufacturing technology to make the hardest diamond on earth for drilling and completion. Besides the application of polycrystalline diamond as PDC cutters, this chapter will also cover its applications in bearing or drilling system.

Keywords: high pressure and high temperature (HPHT), ultra HPHT, polycrystalline diamond compact (PDC) cutter, PDC drill bit, oil and gas, bearings

1. Introduction

Polycrystalline diamond compact (PDC) drill bits are critical drilling tools for most formations in oil and gas exploration and drilling, with annual market size of more than $4.5 billion. PDC cutters are the main and critical component in PDC drill bits that cut these formations because of their excellent properties such as high hardness, thermal conductivity, impact resistance and wear resistance. PDC drill bits equipped with PDC cutters have gained widespread popularity in oil and gas drilling due to their long bit life and ability to maintain a high rate of penetration (ROP). The shearing effect caused by the fixed PDC cutter has been shown to be more effective than the crushing effect of the tooth or insert on the rollcone drill bits. Most PDC drill bits consist of a body either milled from a solid steel block or infiltrated by a metallic binder into tungsten carbide particulars. The bit body has blades, in which the actual PDC cutter is mounted in the

form of flat or shaped diamond table, as well as open areas or slots where cuttings and mud streams can escape to the annulus. **Figure 1** shows a typical 5–7/8″ diameter PDC bit. In **Figure 1**, the PDC cutters are brazed and placed on the blades. The flow pathways are used for mud and cuttings removals. However, when drilling very hard and abrasive formations, PDC drill bits on the market face very high challenges [1–3]. PDC cutters currently available on the market do not provide sufficient wear resistance, impact resistance, or thermal stability to cope with this challenging drilling environment. Low penetration rates (ROP) and short bit life have led to the use of multiple bits to drill a single interval, which is not optimal for well economy [4–6].

The main weakness in the current technology comes from the unavoidable use of a metallic catalyst (typically cobalt) during the manufacturing of the PDC cutters [4]. **Figure 2** shows a typical SEM microstructure of PDC cutter showing Co catalyst

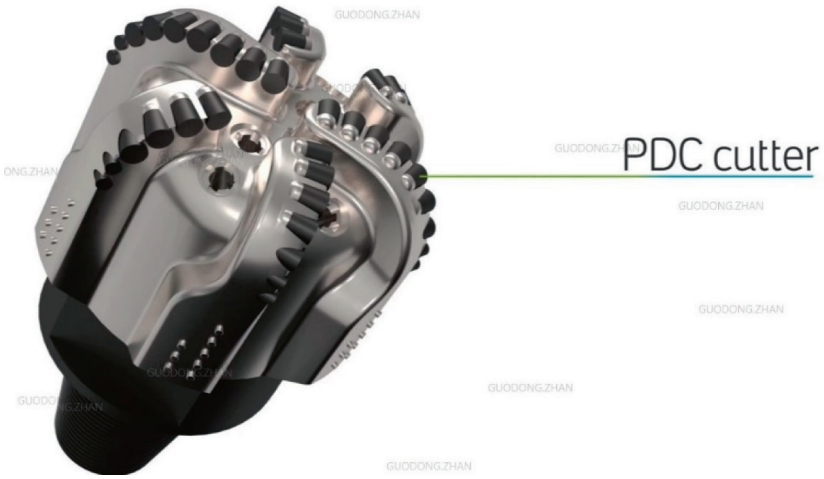

Figure 1.
PDC Drill bit equipped with PDC cutters.

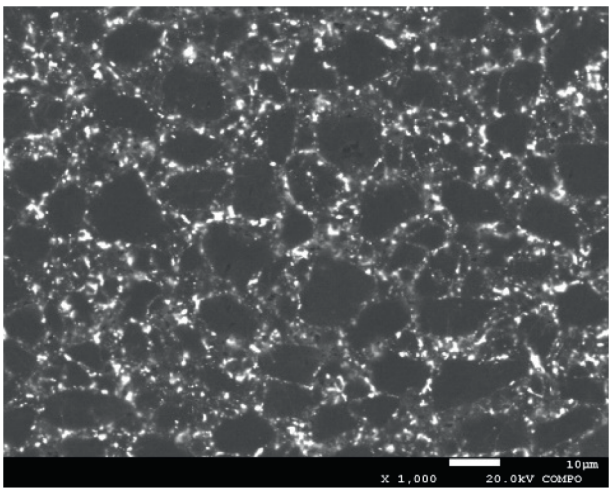

Figure 2.
A typical SEM microstructure of conventional PDC cutters with Co.

distribution in the diamond structure. Traditionally, PDC cutters can be manufactured at relatively low pressures and temperatures, around 5.5 GPa and 1400°C, respectively, due to metal catalysts. However, these metal binders reduce the hardness of polycrystalline diamond (PCD) materials to approximately 50–70 Gpa [7]. More seriously, when the formation or rock drilling operation generates high frictional heat, the metal catalyst binder in the PCD layer will unfavorably help the diamond turn back into graphite. In addition, the cutting and drilling process exposes the PCD material to high stresses, where PDC cutting edges with cobalt binders tend to produce microcracks and diamond particles fall/collapse when the stress is greater than the binding strength of the diamond grains in the PDC cutters at a specific temperature. The reason for this can be explained by differences in the modulus of elasticity and coefficient of thermal expansion between the cobalt metal binder and the diamond, which can lead to a mismatch between the volume change of the diamond and the binder in a high-stress and high-temperature operating environment. As a result, large stresses are created inside the PDC material, leading to early failure. Therefore, the whole drill bit industry tried to leach out the metallic binder from the diamond structure to improve the thermal stability. But this can reduce the fracture toughness of the PDC cutting structures and shorten the drill bit life. Developing a catalyst-free or binderless PDC cutter for drill bits would be an ideal and game-changing technical solution that has the potential to achieve the goal of "one run to total depth" in drilling technology.

This chapter will highlight their own research and development of binderless or catalyst-free micro polycrystalline diamond (MPD) PDC tools and related drill bit technologies in the oil and gas industry. Ultra-high pressure and ultra-high temperature (UHPHT) technologies make this possibility a reality. UHPHT technology is cutting-edge technology developed for many advanced superhard materials. Currently, the technology is mainly focused on the study of nanocrystalline diamond (NPD). However, their industrial applications are limited by small sizes and/or high costs. In Japan, researchers [8] developed a Kawai type 2–6-8 large-cavity hydrostatic pressure device that successfully achieved a high pressure of about 15 GPa when synthesizing millimeter-scale nanocrystalline PDC materials. Since then, after nearly 10 years of further development, the size of synthetic NPD has been successfully increased to the centimeter level. Larger tonnage high-pressure units are required to obtain larger sample sizes and ensure reasonable high-pressure efficiency. In anvil design, high reliability and efficiency are mainly affected by load losses during the transmission process, of which the structural design of the anvil assembly and the strength of the anvil material in the final stage are the most important. The progress of our UHPHT technologies will be introduced.

2. Diamond basic

Diamond, with a Vickers hardness of more than 100 GPa, is one of the most commonly used superhard materials for industrial applications because it has short and strong covalent bonds between carbon atoms in cubic crystal structures. It is a metastable allotrope of carbon, with atoms arranged in a modified surface-centered cube (fcc) crystal structure called a "diamond cube" or "diamond lattice." Currently, there are two approaches, either using graphite as a starting powder, or using diamond in the industry to produce catalyst-free or binderless PCDs, and two carbon allotropes – diamond and graphite (**Figure 3**) will be focused on, which have very different mechanical properties from superhard and supersoft materials, respectively.

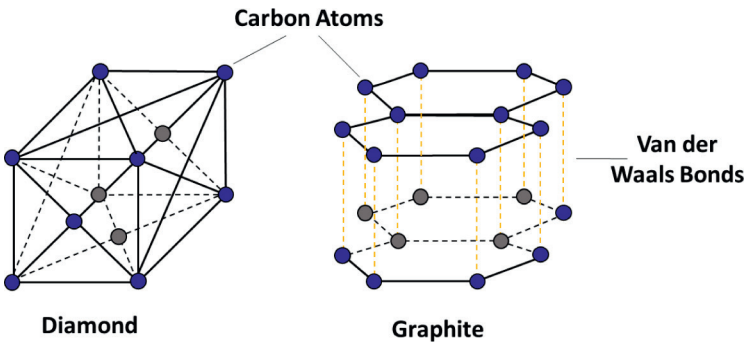

Figure 3.
Two carbon allotropes - diamond (left) and graphite (right) [9].

Diamonds are the hardest known phases in natural and synthetic materials, with a face-centered cubic lattice (space group #227, a = 3.56679 Å). In this compact structure (density of 3.51 g/cm3), the atoms are covalently bonded to four other atoms due to sp3 orbital hybridization, with an average bond length of about 1.54 Å. Graphite has a hexagonal structure (space group #194, a = b = 2.456 Å, c = 6.696 Å), formed by stacks of layers composed of regular hexagonal carbon. Each atom of a given layer is covalently bonded to three other atoms to form a sp2 hybridization type, while the bonds between the layers are weaker, by van der Waals type. The stable form of crystalline carbon at standard temperature and pressure (STP) is graphite, while at higher temperatures and pressures above the well-known Berman-Simon line [10], the cubic form of diamond is stable. Because the diamond is processed using the high temperature and pressure technology above the Berman-Simon line, the diamond retains its unique superhard cube structure when lowered to STP. The formation of diamond from graphite is only a phase transition under HPHT, given by the following equation:

$$C_{graphite} <=> C_{diamond} \quad (1)$$

At atmospheric pressure, the Gibbs energy change from graphite to diamond at all temperatures is greater than zero, which means that graphite is a stable phase at all temperatures at atmospheric pressure. However, since diamonds are a denser form of carbon, one would expect increased pressure to make diamond formation more likely. Both diamond powder and graphite powder can be used as raw materials to create bulky, superhard-cutting structures for drilling tools. However, the sintering mechanism is completely different, which has a great impact on the properties of the material.

Due to its extremely high hardness, diamond is widely used in industrial applications that require very high wear resistance. It can be processed as a single crystal in the form of large blocks, or as a powder for grinding, polishing, and grinding operations, or as a PDC tool, where individual grains are joined together by a high pressure and high temperature (HPHT) process. Until the 1950s, only natural diamonds could be used for niche abrasive applications. With the introduction of the HPHT process for synthetic PCDs by GE in 1955 [11], the use of synthetic diamond abrasive materials has increased dramatically. While the performance of natural diamonds varies greatly due to differences in defect density and impurity

levels, the performance of synthetic or man-made diamonds is more controllable and consistent. Therefore, synthetic diamonds (grit or bulk) are the first choice for most industrial applications. Another reason is that they cost relatively little. One of the most successful tools for using synthetic diamond is the PDC cutter for oil and gas drill bits, which significantly improves drilling economy by increasing drilling speed (ROP) and tool life, as shown in **Figure 4**. Although PCDs have been successfully used in oil and gas drilling tools, they still suffer from catastrophic failures from time to time due to their inherent low fracture toughness compared to other cutting materials such as cemented carbide. In the course of oil and gas exploration, many different rock formations may be encountered. Some will be coarser than others, while others will consist of a mixture of hard and softer phases, which will have a significant impact on the tool when drilling. These shocks can cause micro-cracks, fragmentation, or spalling, which can seriously impair the drilling schedule. It is also thermally unstable at high temperatures, which is likely to occur during drilling, especially in hard formations. When the PDC cutter heats up due to strong rock/cutter friction during the drilling process, the expansion of the metal Co far exceeds that of the diamond grain, resulting in extensive thermal stress and further cracking.

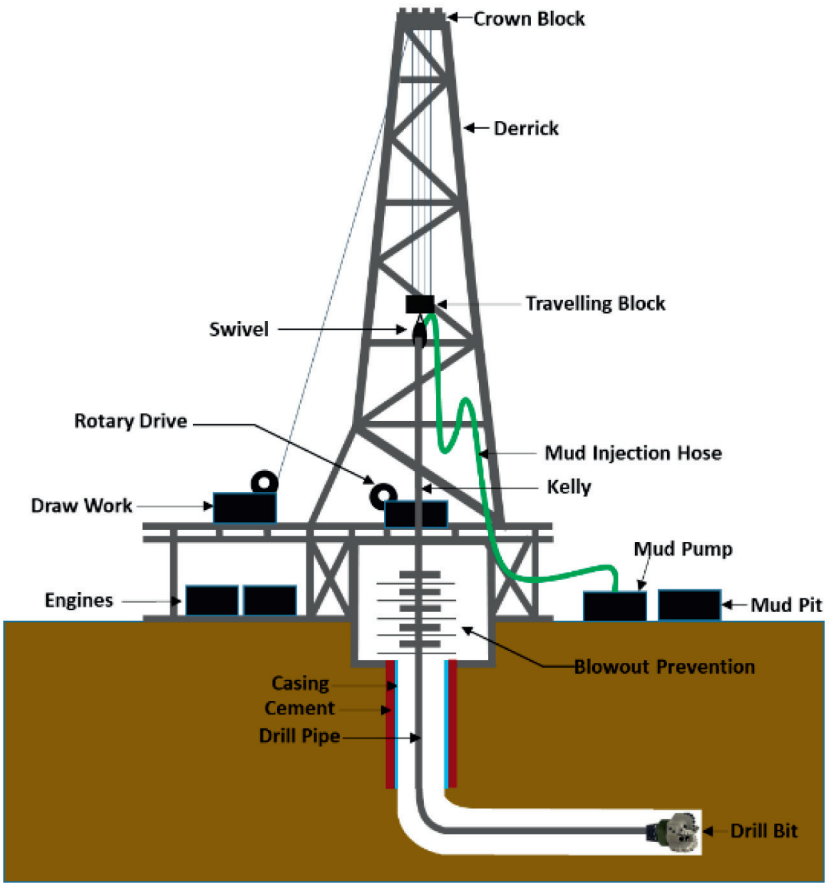

Figure 4.
PDC drill bit applications in oil & gas exploration and drilling [9].

3. Diamond synthesis and PDC manufacturing technologies

3.1 Conventional high-pressure high-temperature (HPHT) technology

The PCD material produced using traditional HPHT technology creates a unique superhard engineering tool material with high hardness, high wear resistance, and high impact resistance. PDC drill bits equipped with PDC cutters are widely recognized in oil and gas drilling due to their long drill life and ability to maintain high penetration rates (ROP) because the shear action of the fixed cutter on penetrating rock is more effective than crushing action of the roller cone bits. There are two main pressing technologies, including belt press and cubic press, which are currently used in the production of almost all synthetic diamond powders and sintered PCDs. Other techniques also exist, but due to the small size of the samples, their use is limited to research and development. The belt press was developed in the 1950s when GE successfully synthesized historically first man-made diamond crystals. Another important HPHT press technology is cubic press technology, which was originally developed as an alternative to generating diamond synthetic conditions, but it has been becoming the primary PDC manufacturing method. Diamond sintering requires extremely high heat and extremely high pressure, and metal systems use catalytic solvents to make the sintering process more economical (**Figure 5**). Typically, diamonds are sintered at temperatures around 1400°C. The source of the catalytic/solvent metal can be enhanced by an in-situ process that directly adds the original diamond powder or infiltrates from the substrate in a state where the catalytic/solvent metal can flow with capillary force. The gap spacing of the diamond raw material is filled with a catalyst or solvent from the matrix, which sinters to bond adjacent diamond crystals together. Cobalt is commonly used as an adhesive phase for PDC presses.

At high temperatures and pressures, diamond-to-diamond bonding occurs, and the metal is relieved into diamond abrasive particles, which helps to catalyze the binding process. For catalytic/solvent metals to be effective, the temperature at which the carbon dissolves and re-precipitates must be reached. These temperatures typically exceed 1200°C [4, 12]. For catalytic solvent systems at active temperatures, diamonds are easily and significantly degraded to graphite at temperatures close to atmospheric pressure;

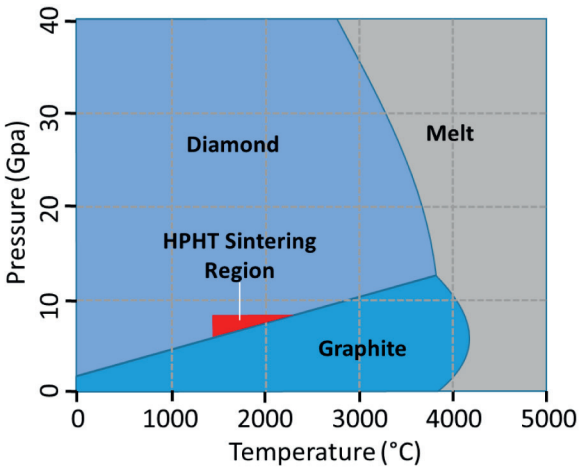

Figure 5.
P–T phase diagram of carbon showing conventional HPHT sintering region [4].

that is, these extreme temperatures can cause diamonds to return to graphite. High pressure is also necessary for the success of diamond sintering. In order to maintain the stable phase of the diamond, high pressure must be maintained during the sintering process. This usually requires a pressure of about 5.5 GPa or more. In this state, the diamond is stable in the sp^3 structure and can be sintered without considering the significant degradation of the diamond raw material. In the design and operation of the HPHT system, the system will reach the required pressure of 5.5 GPa and 1427°C while maximizing the life expectancy of expensive hard metal tools such as anvils and molds. PDC cutters and synthetic diamond manufacturers are constantly striving to improve the performance and cost-effectiveness of their HPHT systems so that more extreme sintering conditions can provide the next generation of high-performance drilling products. In order to achieve these high temperatures and pressures at the same time, cubic pressure technology development is the key. The cube press consists of six large pistons, each of which can provide thousands of tons of force. Each piston pushes a small tungsten carbide anvil, which in turn compresses a cubic pressure unit containing the starting material (cemented carbide and diamond powder). Once the cube is pressed to reach the desired pressure, the current generates the desired high temperature through a resistance heater embedded in the pressure unit. These conditions are maintained long enough to ensure that a complete diamond-diamond bond is formed among diamond particulates to make the diamond bulk. However, the pressure is limited to a maximum of 10 GPa because the graphite heater will be transferred to the insulated diamond and lose its heater function.

One of the challenges in improving PDC cutter performance through traditional HPHT processes is the removal of Co, a key component in the formation of a robust diamond-to-diamond bond structure during PDC cutter manufacturing but is also the main cause of these problems in drilling applications. The entire industry has been researching and improving leaching methods or other methods to reduce the adverse effects of Co. On the bright side, the removal of Co improves the thermal stability of PDC tools by reducing the tendency to graphitization at high temperatures and preventing accelerated cracking caused by the above thermal stresses. On the downside, removing the Co phase tends to reduce the fracture toughness of PDC tools. Therefore, PDC cutter suppliers often offer Co leaching at different depths depending on the application requirements. Currently, there are no "standard" tools, but a range of tool leaching designs that suit different drilling requirements. The industry's best desire is to raise the degradation temperature from the usual 750–1200°C through cobalt leaching. Zhan et al. [4] made the thin film with a scanning electron microscope (SEM) showing what happens when the PDC sample is heated under mimic reservoir conditions. The end result is thermal failure, darkening the material when irregular cracks appear, turning the once uniform surface into something similar to the cracked mud seen at the bottom of a dry pond. There is a solution to this problem, called the deep leaching technique, which leaches most of the cobalt by immersing the PDC in the acid. But it also has its limitations, as some metals are sealed in spaces that liquids cannot reach and are left behind. The industry as a whole is researching (improving) leaching methods or other methods to further reduce the impact of cobalt. Across the industry, PDC cutters aim to be able to withstand the resulting high temperatures when cutting hard, variable formations. The industry's rule of thumb is that high temperatures can damage PDCs above 750°C, and leaching pushes this limit up to around 1200°C. One of the emerging technologies identified as technological breakthroughs is that through UHPHT technology that can manufacture PDC cutters without the use of metal catalysts [13, 14]. In this chapter, a range of new ultra-strong catalyst-free PDC cutting materials using innovative UHPHT technology has been

successfully synthesized and tested. These catalyst-free or binderless PDC cutting materials are more than twice as hard as current PDC cutting machines. As a result, new industry records for wear resistance are more than three times higher than traditional PDC cutters used in the oil and gas drilling industry. The new material also has fracture toughness close to that of metals. In addition, these catalyst-free PDC cutters do not require any expensive and time-consuming leaching process to remove the Co catalyst. With these super-strong catalyst-free PDC cutting elements on PDC drill bits, the possibility of achieving the game-changing goal of "one run to total depth", especially in drilling, hard formations is explored.

3.2 Ultra-high pressure and ultra-high temperature (UHPHT) technology

Ultra-high pressure and ultra-high temperature technology is a cutting-edge technology. At present, the technology is mainly focused on the research of nano-polycrystalline diamond (NPD). However, their industrial applications are limited by tiny sample sizes. This chapter will introduce new UHPHT techniques to create centimeter-sized samples that are large enough for industrial and scientific applications. Expanding the sample chamber is an important goal in UHPHT device development, and its record is constantly being refreshed. In 2003, Irifune et al. successfully synthesized millimeter-scale nanocrystalline polycrystalline diamonds using a hexagonal large-cavity hydrostatic pressure device [8, 15] under high pressure conditions of about 15 GPa. After nearly 10 years of improvement, the size of synthetic NPD has been increased to the centimeter level. Large tonnage high pressure devices are required to obtain larger sample sizes and to ensure reasonable high-pressure efficiency. The high-pressure occurrence efficiency is mainly affected by the load loss in the transmission process, whether it is the mechanical structure of the assembly or the strength of the final stage of anvil material. Please refer to the reference [12] for more details in NPD development and their performance. In a combination of multi-stage loading, for the first time a two-stage loading device that is integrated directly into the first six-sided cubic pressure chamber was developed [16], eliminating the intermediate conversion process of loading by a single axis. Compared to type 2–6-8 loading based on belt press technology, tri-axial loading significantly improves the transmission efficiency of loads. The utility of a new type of superhard material, such as NPD and cubic boron nitride, depends heavily on the sample size and pressure required for bulk materials, typically around 14 GPa. Therefore, the challenge in developing a large cavity static pressure device should be to increase the pressure limit while expanding the cavity. Ultra-high-pressure technology is based on a hinge six-sided cubic press, with a single cylinder load capacity of about 50MN (5000 tons) in the centimeter cavity. On the other hand, the technology capable of producing large tonnage six-sided cubic presses is cost-effective, which will expand its range of applications. Millimeter-scale samples are still limited to the physical properties studied. The application prospect of centimeter-level samples in comprehensive physical characterization and tool device preparation is broad. Therefore, the ability to integrate the production of centimeter-level samples on a single-axis (double-sided) press and the development of centimeter-level high-pressure chambers with pressures greater than 14 GPa are of great significance for the high-pressure research and application of new superhard materials.

3.3 Shaped cutters

PDC cutters are key components of the drill bit. Most PDC cutters in drill bits have flat diamond cutting tables or layers. Recently, due to advances in cutter material

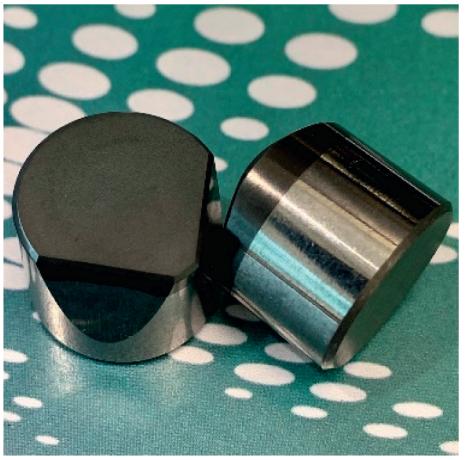

Figure 6.
Examples of shaped PDC cutters.

development and geometry cutting technology, special-shaped PDC cutters, for example ax-shaped cutters (ASC) (**Figure 6**), have been warmly welcomed by drilling engineers to drill many hard and abrasive formations [17]. The shape of the PDC cutter has a great influence on the impact resistance of the component and the mechanism of cutting the formation, which greatly affects the performance of the PDC drill bit.

4. Catalyst-free or Binderless Micro polycrystalline diamond (MPD)

4.1 Experimental procedures and materials characterization

For the synthesis, characterization and their applications of NPD materials, see the review journal paper in [12]. This chapter will focus on our own work on the basis of micro-polycrystalline diamond (MPD) or catalyst-free polycrystalline diamond (CFPCD), based on a newly developed hinged six-sided cubic press [18]. Drilling very hard, abrasive and sandwich formations presents a significant challenge for today's PDC drill bits. Current PDC tools on drill bits do not provide sufficient wear, impact, or thermal stability to withstand this drilling environment, resulting in low penetration rates (ROP) and short drill life. The weakness of existing PDC cutters is due to the inevitable use of cobalt catalysts to bond diamond grains manufactured by traditional HPHT techniques with a combined capacity of about 5.5 GPa and a temperature of about 1400°C. In our study, ultra-high pressure and high temperature (UHPHT) technology was developed by an innovative two-stage multiple anvil that is capable of producing ultra-high pressure of 14–35 GPa, which is three to seven times that of traditional PDC cutting machine manufacturing techniques. In addition, extreme heat from 1900–2300°C was achieved. Using this UHPHT technology, new PDC materials with super strength and no catalyst at two high pressures of 14 and 16 GPa have been successfully produced in order to study the different responses of material properties under different processing parameters. As the starting material for the experiment, the average particle size of commercially available high-purity diamond powder is 10 microns, and the particle size distribution is 8 to 12 microns. Then these

diamond powders were pressed in the newly developed and innovative UHPHT press. Details of the processing can be found in the references [13]. The preparation of NPD from graphite involves a phase transition mechanism [15]. This results in a significant volume change of more than 35% due to density changes (under ambient conditions, graphite density ~ 2.25 g/cc to diamond density ~ 3.52 g/cc). Large shrinkage is known to make pressure and temperature control more unstable or difficult (heater deformation), especially under extreme HPHT conditions. On the other hand, our CFPCD synthesis or fabrication process uses diamond powders with micron, sub-micron or nanoscale grains available on the market as raw materials to solve all of the above problems and challenges, as there is no phase transition when pressing diamond powder into diamond blocks under UHPHT. As a result, the microstructure of CFPCD materials and the resulting mechanical properties are more controllable between hardness and toughness. This is important for large-scale industrial tool manufacturing applications. Essentially, this work provides a new strategy or approach to developing the next generation of super-hard or super-hard diamonds. **Figure 7(a)** and **(b)** show the typical microstructure of a PDC tool with pressures of 14-GPa and 16-GPa, respectively, showing the full detection of diamond structures without a metal binder.

Scanning electron microscopy (SEM) was used to study the morphology and microstructure of polished samples. Samples prepared at 16 GPa and 2300 °C are characterized by transmission electron microscopy (TEM) with an acceleration voltage of 200,000 volts for microstructures at high magnifications. **Figure 8** shows the HRTEM nanostructure features in a 16-GPa CFPCD material that are produced by severe plastic deformation of a single diamond grain during UHPHT. Extensive twins and stacked faults in the particles were observed. This is due to the high-pressure work hardening mechanism [13], which can greatly improve the strength of UHPHT CFPCD materials. Typically, CFPCD materials consist of a diamond skeleton consisting of micron-sized particles and an isolated Y-zone. Each micron-sized particle has a substructure of stacked nanoplates, while the Y-zone consists of NPDs embedded in turbo graphite and amorphous carbon. This unique micro-nested structure stems from the plastic deformation of the diamond particles and the mutual transformation of the diamond produced during the high temperature and high-pressure process.

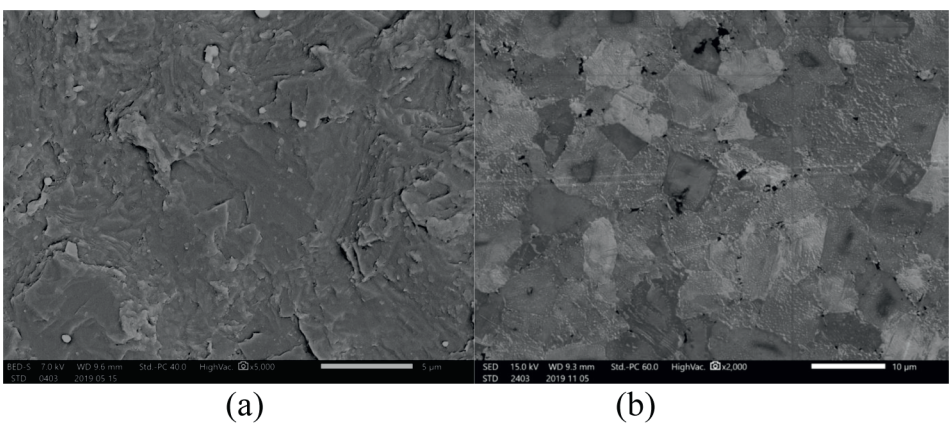

Figure 7.
SEM microstructures of (a) 14-GPa CFPCD, and (b) 16-GPa CFPCD showing fully dense catalyst-free microstructure [19].

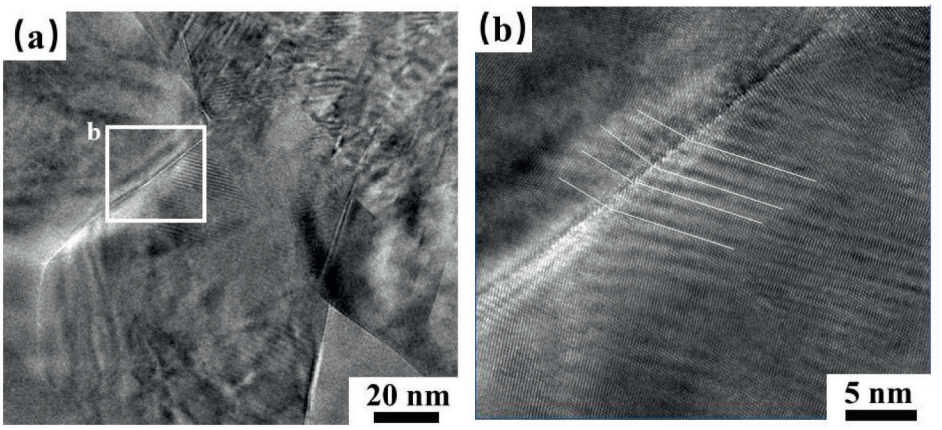

Figure 8.
The HRTEM showing nanostructure features (substructure) of twin and stacking fault in grains [9].

Crystallization defects prevent grain alignment during deformation and play a preventive role, which is conducive to its mechanical properties. In addition, during processing, the particles form plastic deformations in the substructure by squeezing the diamond particles, and the hardness is further increased due to the Hall–Petch effect [20].

4.2 Mechanical properties - hardness and fracture toughness

Hardness is a key performance index of materials and is mainly tested by the indentation method. The Vickers hardness indentations were performed on the polished samples of these materials under an applied load of up to 9.8 N and a dwelling time of 15 s. **Figure 9(a)** and **(b)** show the Vickers hardness (Hv) indenter before testing with a standard indenter made of a single crystal diamond, and the indenter that is damaged after pressing it into a CFCD sample, respectively. The tests were

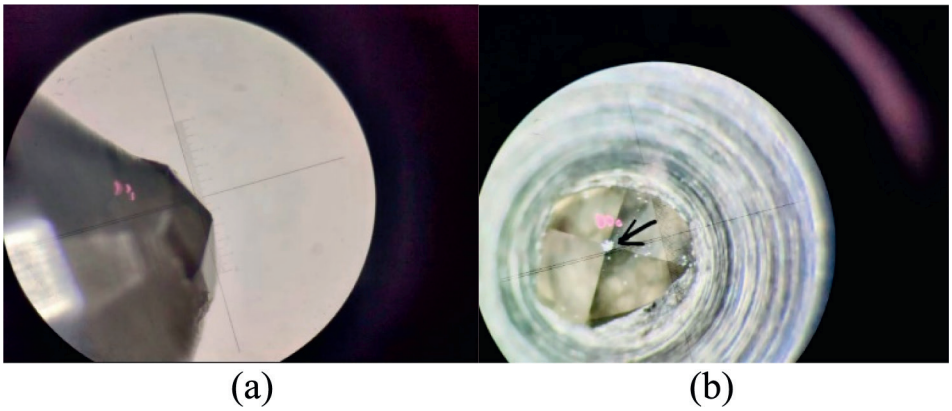

Figure 9.
The optical images of single crystal diamond indenters (a) before the hardness testing and (b) after the testing on CFPCD material, showing the hardness of the CFPCD material is higher than single crystal diamond (120 GPa). Arrow in **Figure 4b** *indicates the damage on the indenter tip [19].*

repeated on 4 different specimens and all 4 new indenters made of single crystal diamond were broken in the same pattern as shown in **Figure 9(b)**. The study found that even when the load was increased from 1 N to 9.8 N, the Vickers indentation on the polished CFPCD sample was too small to be accurately measured. As a good comparison, standard diamond indenters remain in good shape after commercial PDC sample testing. The comparison results showed that the hardness of the CFPCD sample exceeded the Vickers hardness limit of single crystal diamond (120 GPa) and was by far the hardest material in the world. The hardness of commercial PDC materials is only about 64GPa.

The ultra-high hardness of microcrystalline diamond materials can be attributed to nanostructural defects such as stacked nanoplate layers, stacked faults, and twin microstructures caused by high-pressure hardening. A schematic diagram of the mechanism of microstructural change of pressure increase is given, as shown in **Figure 10**.

The fracture toughness of MPD samples has been characterized and calculated by the following equation [21].

$$K_{IC} = \xi \left(E / H_V\right)^{1/2} \left(P / c^{3/2}\right)\left(MPa\,\mathrm{m}^{1/2}\right), \tag{2}$$

where ξ is the calibration constant of 0.0166 (±0.004), E is Yong's modulus (GPa) (in the experiment Young's modulus, 1050 GPa, is used for diamond), P is the loading force (N), and c is the length of the crack.

The K_{IC} of MPD prepared at 14 GPa and 1900°C is 18.7 MPa $m^{1/2}$, the highest in the world of diamond materials. This is 3.7 to 5.5 times higher than a single crystal diamond. Interestingly, microcracks are mainly generated on diamond microcrystallines and terminated at the grain boundary (Y-zone). The Y-region of the nanostructure is composed of nanocrystallines, turbo graphite, and amorphous carbon, which can significantly prevent further propagation of cracks, thereby greatly improving the fracture toughness of the prepared sample. For 16-GPa CFPCD materials, it is difficult to measure indentation fracture toughness due to the previously-mentioned indenter damage. However, other ways are explored to assess the fracture toughness of materials and will report in the future.

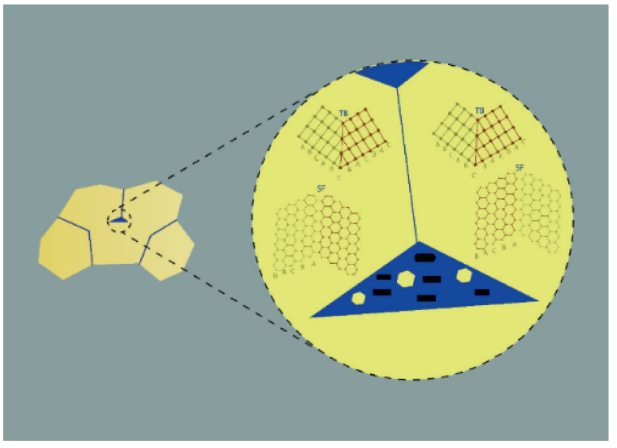

Figure 10.
Schematic deformation micro-mechanism of UHPHT superstrong diamond.

4.3 Wear resistance

The cutting performance of a sample is the most widely used method to evaluate the cutting performance on a turned granite log by cutting it on a CNC lathe. Granite has high hardness and abrasion resistance, as well as low thermal conductivity. The cutting parameters of the granite log turning test are as follows: cutting speed (*Vc*) of 100 m/min, depth of cutting (*Ap*) of 0.5 mm, and feed rate (*f*) of 0.4 mm/rpm. CFPCD and commercial PDC samples are processed into cylindrical cutting tools with a diameter of 11 mm and a height of 6 mm. *G* ratio is the ratio of rock loss volume to wear flat volume, which is used to evaluate the wear resistance of the material to granite. The reference HPHT cutter is also carefully selected from the best PDC cutters currently used in drilling hard formations. The wear resistance of the CFPCD and commercial PDC samples is quantified using the abrasion wear ratio, *G*, and the wear rate or ratio is calculated using the following equation:

$$G = \frac{V1}{V2} \tag{3}$$

Where V1 is the volume loss from granite, (mm^3); V2 is the volume loss from cutting tools (mm^3). The higher *G* means the higher wear resistance of the material.

Figure 11 shows an optical image of the cutting edge of a CFCD sample and a commercial PDC sample after cutting the granite by length of 1260 m. It can be clearly seen that the wear area of the commercial PDC sample is uneven and significantly larger than the wear area of the CFPCD sample, especially when the turning length reaches 1260 m. The study found that the average wear ratio of CFPCD samples is more than four times that of commercial PDC samples, making it the best diamond material currently used in the industry. Previously, it took a decade for PDC tools to improve their wear resistance by 30 to 50 percent. This breakthrough represents a 50-year technological leap in the development of PDC cutting machine technology. As the cutting length increases, the CFPCD sample is at a stable level because the diamond blocks do not fall off during turning granite testing. The extraordinary wear

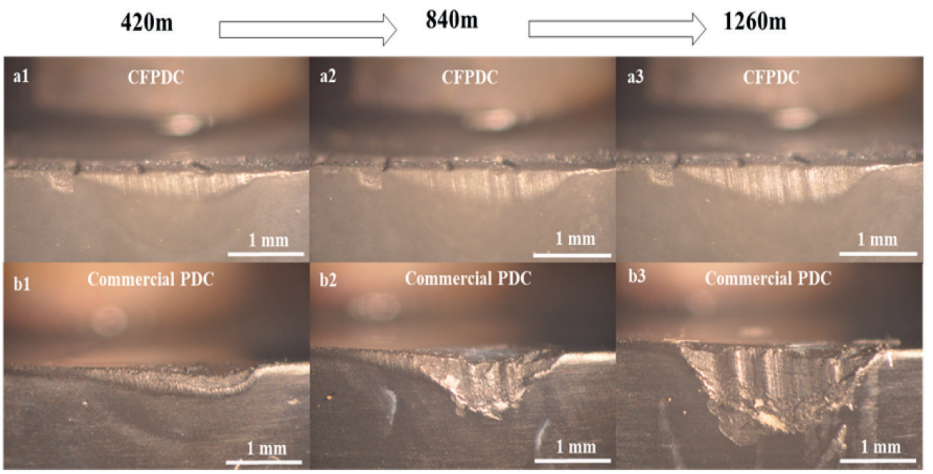

Figure 11.
Wear flats development of (a1-a3) UHPHT 16-GPa synthesized CFPCD, and (b1-b3) reference cutter [14].

resistance of CFPCD materials is directly related to their ultra-high hardness, which is due to the fact that it is catalyst-free.

4.4 Thermal stability

Thermal stability and oxidation resistance at high temperatures are important for applications of PDC cutters, especially in hard and abrasive formation drilling in the oil and gas industry. Thermal stability and oxidation resistance tests are performed at different temperatures from room temperature to 1400°C by an in-situ XRD. The in-situ X-ray diffraction (XRD) using Cu kα radiation at a wavelength of 0.15406 nm, a step rate of 0.01°/s, and a scanning range of 2θ = 10°-100°, is used to characterize the phase transition of CFPCD samples from room temperature to up to 1400°C. For comparison, commercial PDC materials were also tested. As can be seen from **Figure 12(a)**, the initial oxidation temperature of commercial PDCs at around 806°C is harsh. On the other hand, the new CFPCD material shows no oxidation until 1400°C (**Figure 12b**) and is found to be even stable at 1200°C – the highest recorded in the industry, well above natural diamond (~800°C), nanoparticle diamond (~680°C), unowned diamond (~1056°C) and commercial PDC (~600°C).

5. Conclusions and future direction

In short, ultra-strong and catalyst-free PDC cutting materials have been successfully synthesized through innovative UHPHT technologies. These new CFPCD materials set new industry records in the diamond family for hardness, toughness, abrasion resistance, and thermal stability. Using these unique properties of the new CFPCD material as a combination of PDC cutters in drill bits, can help achieve the goal of "one run to TD" game-changing drilling techniques. Future research directions (**Figure 13**) continue to explore much higher pressures and higher temperatures domains and produce larger size UHPHT CFPCD cutting materials in preparation for further breakthroughs in drilling technology.

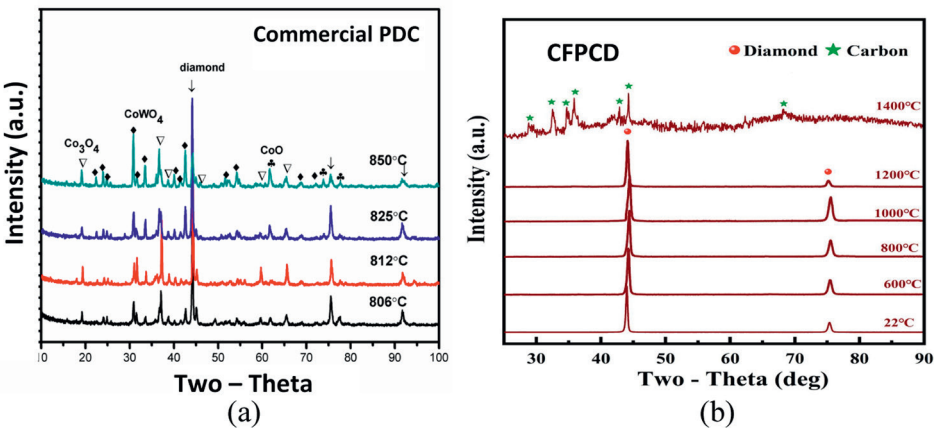

Figure 12.
High-temperature in-situ XRD spectra of (a) a commercial PDC material, and (b) a 16-GPa UHPHT CFPCD material at temperatures up to 1400°C [14].

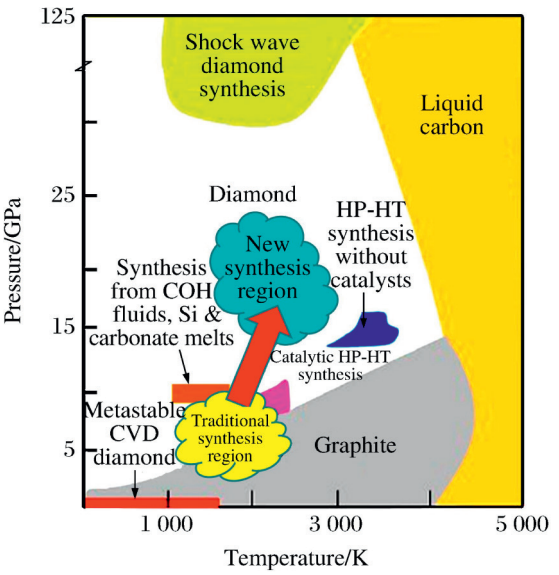

Figure 13.
Future research directions for ultra-high pressure and ultra-high temperature [18].

6. Other applications

Bearings have been used in various industries in a variety of forms and shapes. They are crucial in tribology to reduce friction between objects. For oil and gas drilling operations, different types of bearings are used, from the surface to the bottom of the wellbore. There are several types of bearings in which surface-to-surface rubbing is involved, such as thrust bearings (as shown in **Figure 14**) and plain bearings, as shown by examples in **Figure 15**. In these examples, the surface-to-surface contact between the counterparts prevailed. Such types of bearings are used in drilling rotary control device (RCD), mud motors, rotary steering system (RSS), powder generating turbines, mud pulse tools, coring tools, electric submersible pumps, etc.

One of the tools is shown as an example in **Figure 15**. The materials of the thrust and plain bearings include bronze, brass, lead-based metal, cast iron, zirconia, tungsten carbide, silicon carbide, and PCD.

The PCD materials currently used in these applications are made of PCD grains bonded by metallic binders, such as cobalt, nickel, iron, or silicon. These metallic binders (Co, Ni, or Fe) are used as catalysts to facilitate diamond manufacturing so that the diamond grains can be obtained at traditionally high temperatures and high pressure. In the above-mentioned bearing applications, PCD materials typically outperform the rest of the materials, mainly due to their high hardness, high compression strength, high thermal conductivity, and very low coefficient of friction.

Electric Submersible Pumps (ESPs) are one of the primary artificial lift methods for oil and gas industry. The system is a complex electro-hydraulic system consisting of a centrifugal pump, a protector and an electric motor in addition to a sensory unit and a power delivery cable. The pump is used to lift well fluids to the surface. The motor converts electric power to mechanical power to drive the pump via the shaft. The power delivery cable provides a means of supplying the motor with the needed electrical power from the surface. The protector absorbs the thrust load from the

Figure 14.
Thrust bearings using catalyst-free and ultra-strong PCD materials [22].

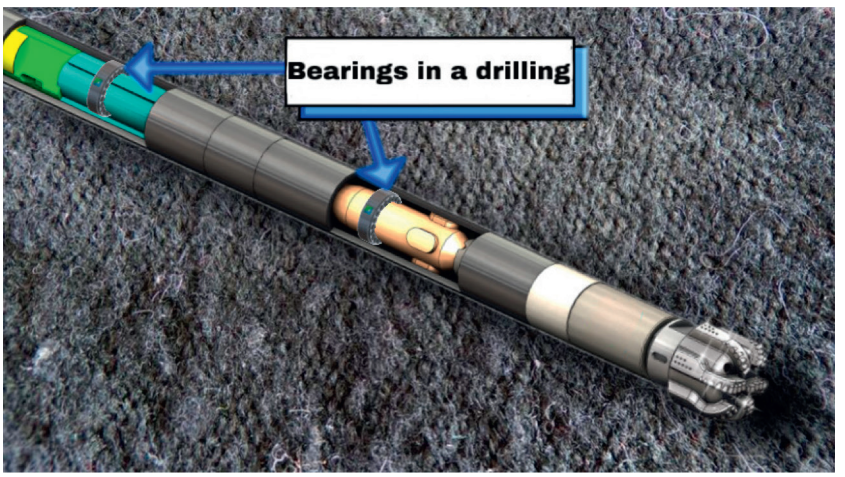

Figure 15.
A downhole tool uses the new catalyst-free, ultra-strong PCD materials [23].

pump, transmits power from the motor to the pump, equalizes motor internal and external pressures, provides/receives additional motor oil as temperature changes and prevents well fluids from entering the motor. The pump consists of stages, which are made up of impellers and diffusers. The impeller, which is rotating, adds energy to the fluid as kinetic energy, whereas the diffuser, which is stationary, converts the kinetic energy of fluids into head. The pump stages are typically stacked in series to form a multi-stage system that is contained within a pump housing. The sum of head generated by each individual stage is summative; hence, the total head developed by the multi-stage system increases from the first to the last stage. The monitoring sub/tool is installed onto the motor to measure parameters such as pump intake and discharge pressures, intake and motor oil temperature, and vibration. Measured downhole data is communicated to the surface via the power cable. The ESP industry faces two main challenges with this legacy technology: reliability and intervention cost. Low reliability is attributed to the system complexity both mechanically and electrically, compounded by the harsh operating environments. High intervention cost is a result of rig dependency of the system for deployment, retrieval and replacement. Improving reliability and developing rigless deployment are the two ongoing battle fronts that the industry is currently engaged in intensely. Both radial and thrust bearings use

Figure 16.
Examples of protector thrust bearing/runner damages.

liquid film to prevent metal-to-metal contact. Erosion, corrosion, vibration, impact force, and heat are all detrimental to the performance of bearings. Bearing failures (**Figure 16**) can lead to vibration, low efficiency, broken shaft, shaft mechanical seal damage, fluid invasion to the motor, and motor electrical failure.

Bearings can be made of our new-generation catalyst-free, ultra-strong polycrystalline diamond (PCD) material synthesized by the novel ultra-high pressure and ultra-high temperature techniques without using any catalyst to greatly enhance the reliability of bearings used in ESPs [22].

Nomenclature

PDC	Polycrystalline diamond compact cutter
PCD	Polycrystalline diamond
CFPCD	Catalyst-free polycrystalline diamond
NPD	Nano-polycrystalline diamond
MPD	Micro-polycrystalline diamond
HPHT	High pressure and high temperature
UHPHT	Ultra high pressure and ultra high temperature
ROP	Rate of penetration
XRD	X-ray diffraction
TEM	Transmission electron microscopy
SEM	Scanning electron microscope

References

[1] Scott DE. The history and impact of synthetic diamond cutters and diamond enhanced inserts on the oil and gas industry. Industrial Diamond Review. 2006;**1**:48

[2] Bruton G et al. PDC bit technology for the 21st century. Oilfield Rev. 2014;**26**:48-57

[3] Bellin F, Dourfaye A, King W, Thigpen M. The current state of PDC bit technology. World Oil. 2010;**9**:41-46

[4] Zhan GD, et al. SPE 168004 In-Situ Analysis of the Microscopic Thermal Fracture Behavior of PDC Cutters Using Environmental Scanning Electron Microscope. IADC/SPE Drilling Conference and Exhibition. Fort Worth, Texas, USA. 2014

[5] Zhan GD, et al. IPTC 2020 IPTC-19764-MS New Ultrastrong and Catalyst-Free PDC Cutting Element Technology. International Petroleum Technology Conference. Dhahran, Saudi Arabia. 2020

[6] Rassenfoss S. Seeking ways to make better diamonds by tending to the tiniest details. Journal of Petroleum Technology. 2014;**66**:P38-P47

[7] Wilks J, Wilks E. Properties and Applications of Diamond. Oxford: Butterworth-Heinemann; 1991

[8] Irifune T, Kurio A, Sakamoto S, Inoue T, Sumiya H. Materials: Ultrahard polycrystalline diamond from graphite. Nature. 2003;**421**:599

[9] Zhan G, Gooneratne C, Moellendick TE, He D, Xu J, Alalsayyednassir A. Ultra-Strong and Catalyst-Free Polycrystalline Diamond Cutting Materials for "One-Run-to-TD" Game-Changing Drilling Technology, 2021 International Petroleum Technology Conference, IPTC-21342-MS. Society of Petroleum Engineering, Houston, USA. 2021

[10] Kennedy C. The equilibrium boundary between graphite and diamond. Journal of Geophysical Research. 1976;**81**:2467-2469

[11] Hall H. Diamond Synthesis, US Patent, 2947608A. 1955

[12] Guignard J, Prakasam M, Largeteau A. A review of binderless polycrystalline diamonds: Focus on the high-pressure-high-temperature sintering process. Materials. 2022;**15**:2198

[13] Liu J, Zhan G(D), Wang Q, Yan X, Liu F, Wang P, et al. Superstrong micro-grained polycrystalline diamond compact through work hardening under high pressure. Applied Physics Letters. 2018;**112**:061901

[14] Li Q, Zhan G(D), Li D, He D, Moellendick TE, Gooneratne CP, et al. Ultrastrong catalyst-free polycrystalline diamond. Nature Scientific Reports. 2020;**10**:22020

[15] Shatskiy T, Katsura KD, Litasov AV, Shcherbakova YM, Borzdov D, Yamazaki A, et al. Ito, high pressure generation using scaled-up Kawai-cell. Physics of the Earth and Planetary Interiors. 2011;**189**:92-108

[16] Liu Y, Zhan G, Wang Q, He D, et al. Hardness of polycrystalline Wurtzite boron nitride (wBN) compacts. Scientific Reports. 2019;**9**(1):10215-10221

[17] Crane D, Zhang Y, Douglas C, Song H, Gan X, Lin Z, et al. Innovative

PDC cutter with elongated Ridge Combines shear and crush action to improve PDC bit performance, SPE-183984-MS

[18] Zhan GD, Moellendick TE, Lin B, Gooneratne CP, He D. New ultrastrong and catalyst-free PDC cutting element technology. The Aramco Journal of Technology. 2020;**3**:2-11

[19] Zhan GD, Li B, Moellendick TE, He D, Xu J. New catalyst-free polycrystalline diamond with industry-record wear resistance. In: MEOS Middle East oil & gas Show and Conference, SPE-204855. Society of Petroleum Engineering, Houston, USA. 2021

[20] Petch NJ. The cleavage strength of polycrystals. The Journal of the Iron and Steel Institute. 1953;**174**:25-28

[21] Chantikul P et al. A critical evaluation of indentation techniques for measuring fracture toughness: II, Strength Method, Journal of American Ceramic Society. 1981;**64**(9):539-543

[22] Xiao J, Zhan GD, Bearing assembly with catalyst-free ultra-strong polycrystalline diamond (PCD) material, US patent application (Application #20210381519)

[23] Zhan GD, Moellendick TE, Li B, Gooneratne C, He D, Producing catalyst-free PDC cutters, USA patent application 20210370396

Chapter 3

Nanodiamonds and Its Applications

Aiswarya Thekkedath and Karthiyayini Sridharan

Abstract

One of the most futuristic and unique carbon materials which is formed from detonation method is nanodiamond. Nanodiamonds below 100 nm size popularly known as attracting crystal or ultrafine dispersed diamonds (UDD) have exceptional optical, mechanical, and biological properties. The structure of nanodiamonds resembles diamond structure. Due to the peerless properties, Nanodiamonds make itself potential to several applications. Nanodiamonds became demand in medical field. Currently, Nanodiamonds acquired substantial recognition in all areas particularly nanomedicine. This chapter opens a detailed review about the evolution of Nanodiamonds, their properties, applications and future perspectives in research. Researchers are still doing their studies on nanodiamonds to make an effective tool in various sectors.

Keywords: Nanodiamonds, structure, synthesis, properties, laser ablation

1. Introduction

The narration of discovery of Nanodiamonds is highly interpreted by the inventor V.V. Danilenko. Over a period of two decades, Nanodiamonds accidently produced three times by Russian scientists through explosion. Initially, Nanodiamonds developed as single diamond particles (having diameter 4–5 nm). Later on Nanodiamonds used as an alternative for semiconductor quantum dots for biomedical imaging. Subsequently, Nanodiamonds used as magnetic sensors, composites, biomolecules and drugs, surface chemistry, other areas in medicines also. At the end of twentieth century, Nanodiamonds or ultrafine-dispersed diamonds (UDD) originated through an ignition of larger masses [1]. Nanotubes, fullerene, 3D, 2D, 1D nanosheets composed of carbon materials captivate young researchers toward wide range of applications. Recently Nanodiamonds (NDs) which is also carbon based material fascinating the world of science. Nanodiamonds is basically composed of carbon having sp^3 hybridization possess elevated chemical and physical properties [2].

Nanodiamonds can be produced through different process namely diamond microcrystals, high pressure high temperature (HPHT), chemical vapor deposition (CVD), laser ablation, detonation technique, autoclave synthesis, electron irradiation of carbon onions, chlorination of carbides, and ultrasound cavitation. Laser ablation, detonation technique, and high energy ball milling of diamond by HPHT methods were using economically. We require large quantities of Nanodiamonds for research and application level studies. In this chapter we are discussing about Nanodiamonds, production of Nanodiamonds, its structure and properties, applications in major areas.

2. Nanodiamonds

2.1 Structure of the Nanodiamond

Diamonds are known as the hardest material and transparent electrical insulator. The structure can be studied in detail by separating the complex structure of Nanodiamond into three ways namely core, an intermediate and the surface layer. Nanodiamonds consists of carbon atoms which are sp^3 hybridized and all form distinctive large crystals. The core of the Nanodiamonds (size approximately range from 2 to 3 nm) looks similar to the diamond structure (sp^3 C-atoms), but the surface be like graphite (sp^2 C-atoms) having hanging bonds edges with functional groups. The inner core holds about major percentage of carbon. The middle sheet which is usually examined as nonhomogeneous translational carbon shell (lesser than 1 nm width). The innermost facet of the shell is detached with onion like carbon rings and the coating composed of graphitic monolayer carbon. The most frequent Nanodiamond outer layer models are (1) a layer of sp^2 carbon atoms which are amorphous in nature and (2) a sheet which is graphitic sp^2 nature in the form of fullerene, known as "Bucky Diamond" (**Figure 1**) [3].

The most distinguishable feature of the Nanodiamond is its core which is distinct from other carbon materials. The high refractive index of the core creates Nanodiamonds useful in polymer coatings and sunscreen as it robust light scattering. Diamonds are non-conducting material with an optical bandgap of 5.5 eV which shows lucidity from ultraviolet to infrared regions. Still their optical properties can be changed by instituting the dopants or imperfections. Chemical elements like (a) boron introduced as dopant will change its lattice thereby boost electrical conductivity applicable in thin film electronics, (b) nitrogen as a dopant increases the vacancy site inside the lattice improve the fluorescence properties and also used in quantum computing, (c) tritium an allotrope of hydrogen introduced in diamond lattice is applicable in biodistribution application and biolabelling [3].

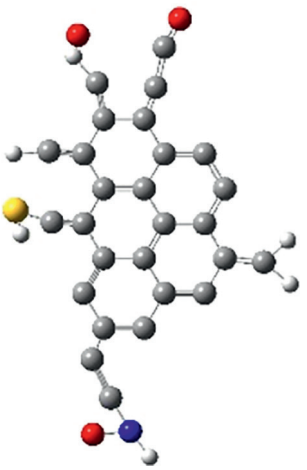

Figure 1.
Structure of the nanodiamond.

2.2 Properties of Nanodiamonds

The properties of the nanomaterials depend on their size. In Nanodiamonds also, depending on the size the properties vary. When the size of the cluster changes, the discrete electronic energy levels become visible at the edges of the bands. As a result the band gap increases as a consequence of separation of frontier orbitals' energy which follows the quantum confinement effect. Quantum confinement will occur when the diameter of the Nanodiamond becomes trivial say 2–3 nm thereby structure variation possible (Bucky diamonds or fullerene structure). When the diameter of the cluster of Nanodiamond increases, the surface carbon atoms reduces and hence the characteristics of the Nanodiamonds improves. During the development of the dangling bonds on the outer layer of the Nanodiamond accords the stabilization of the material. The surface terminations have influence on the stabilization of carbon compounds drained the center of attention to several studies. For good functionalization and surface termination, the surface of the Nanodiamond can be enhanced with the organic functional groups. These groups can be easily identified by FTIR studies.

The surface functionalization and size studies make Nanodiamonds a potential material in drug delivery, biomolecule conjugation, uploading sorbent molecules, catalytic application and polymer matrix. At room temperature, the nitrogen vacancies in Nanodiamonds provide red emission spectrum and visible emission spectrum. Nanodiamonds also favors the fluorescent properties empowers the nanoelectrometry, nano-magnetometry, etc. Nanodiamonds can tune their magnetic and optical properties by adjusting the surface chemistry of the material.

Nanodiamonds have high hardness, thermal conductivity, biocompatibility, Young's modulus, chemical stability, high electrical resistivity, resilience to a dictatorial setting. Nanodiamonds are known for their exceptional mechanical and optical qualities, as well as their large surface areas and tunable surface topologies. They're also nontoxic, making them ideal for biological applications [4]. The most featured properties are fluorescence and biocompatibility which are depicted below.

2.2.1 Fluorescence

Introducing a nitrogen vacancy in the lattice is known as NV center or nitrogen vacancy center which dominance the fluorescence properties in Nanodiamonds. A nitrogen vacancy is created by bombarding elevated particles and vacuum annealing between 600 and 800°C. During the irradiation vacancy will form at the centers and during annealing the vacancies will emigrated and confined by the nitrogen atoms. During this process two types of vacancy center forms namely negatively charged nitrogen vacancy and neutral nitrogen vacancy center. In addition, both vacancy centers will have distinct emission spectra. Among these, peculiarity falls into negatively charged nitrogen vacancy center as it has a spin S = 1 ground level results in spin polarization through optical pumping and controlled by electromagnetic resonance. The spin coherence time for this vacancy center is quite long. Nitrogen vacancy became highly capable for bioimaging, magnetic sensing, and fluorescence resonance high energy transfer.

Under high temperature and pressure synthesis, blazing photo luminescent Nanodiamonds can be produced in materials later squeeze down to nano sized particles. The concentration of NV imperfections developed from electron irradiation, does not depend upon the size of the Nanocrystals but they can decrease the size of the Nanodiamonds as the electrons might get pin down at the surface.

Recent studies picturizes the interest on imaging applications from nitrogen vacancy centers. In a bare Nanodiamond (~5 nm) developed from trinitrotoluene (TNT) and hexagon precursor, the intermittent luminescence is emanated from nitrogen vacancy center is reported [5]. Nanodiamonds which are considered larger (>20 nm) grown from TNT, graphite precursors show the presence of stable luminescence [6]. When fluorophores are linked or adsorbed with Nanodiamond fluorescent particles are formed. This fluorophore linked Nanodiamond can pass through different cell chambers (variable pH) without changing the cell feasibility [7]. When octadecylamine is covalently linked with carboxylic acid on a nanodiamond surface a bright blue fluorescent Nanodiamond is produced and reported [8].

2.2.2 Biocompatibility of Nanodiamonds

Diamond is known as a non-toxic material. The toxicity of Nanodiamonds is investigated through in-vivo as well as in-vitro studies. Both studies scrutinize the characteristics of a cell feasibility, cell mechanism and behavior. Through in-vitro cytotoxicity, carbon nanomaterials like nanotubes (single as well as multi walled), carbon black the toxicity were studied. They also examined with Nanodiamonds. The studies concluded the carboxyl nanotubes are more toxic rather than Nanodiamonds as carboxyl Nanodiamonds shows relatively less toxicity [9].

In human beings, in-vivo toxicity is deeply developed with the help of animal models. By the detonation techniques Nanodiamonds are formed in a powder form (low density) which will be easily spread in the environment. The respiratory tracking is much more efficient in human beings to study the toxicity. To know more about the tracking of the toxicity intratracheal instillation can be selected. Nanodiamonds controlled by intratracheal instillation is examined by biomedical measurement is diffused into spleen, liver, heart and bones [10]. The interaction of nanomaterials introducing to living system is monitored through adsorption, distribution, metabolism and excretion process (ADME process). As nanomaterials are very small, it is arduous to spot the interaction through a microscopic method. One of the most promising technique for good reliability, high sensitivity, and easy detection is radionuclide tracer technique. Gallium, Indium, Copper are used for labeling carbon nanoparticles. Rhenium Nanodiamonds are appropriate Nanodiamonds used for experimental research.

3. Synthesis of Nanodiamonds

Nanodiamonds can be synthesized using different techniques and also artificial synthesis also available nowadays. Diamonds are allotropes of carbon. Diamonds are natural and found in the Earth's mantle having high temperature and pressure. Once a diamond phase is formed, there is a chance to move to graphitic phase. In order to prevent this phase, it has to undergo a high energy barrier phase transition that will overcome the change of sp^2 to sp^3 which makes diamond in a metastable phase. Several techniques for the synthesis of Nanodiamonds are depicting here. The most common methods are CVD, detonation technique, laser ablation and HPHT methods (**Figure 2**).

3.1 Chemical vapor deposition technique (CVD)

This method is among the most used thin film coating methods, and it was utilized to make nanocrystalline diamond layer. More specifically, carbon atoms

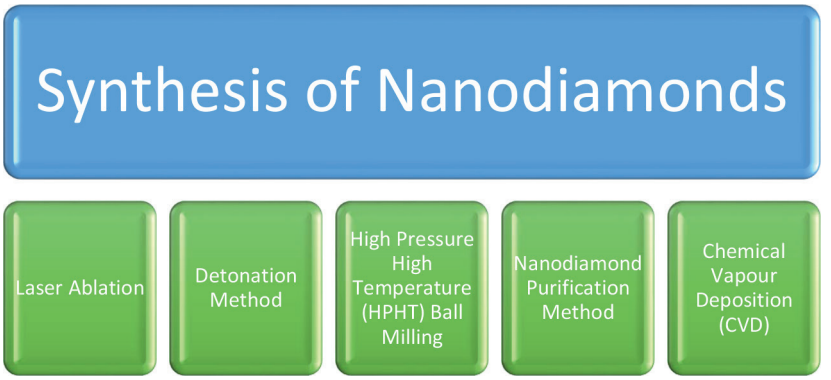

Figure 2.
Synthesis of Nanodiamonds.

are deposited during the breakdown of a gaseous mixture and carbon-containing molecules, most commonly methane CH_4 (excess hydrogen). The gas phase decomposes into radicals like H• and CH3•, which are required for diamond formation, via a heated filament or microwave plasma. A continuous ND film is created on a membrane, usually a thin layer of silicon covered with a μm powder that functions as a nanodiamond deposition seed. Depending on the relative concentration of CH_4/H_2, the size of the coils wrapping the film ranges from 10 microns to a few nanometers.

Microcrystalline diamonds are formed by a low concentration of CH_4, while a large quantity of CH_4/H_2 lowers particle size to the order of 10 of nm at 15% CH_4/H_2. After the hydrogen is absorbed by H• radicals, the carbon atoms on topmost of the diamond seeds are left with their bonds dangling. The CH_3 molecules are then used to fill these bonds. New carbon can be caught together and finally bound in a diamond chains when this process occurs in two nearby regions [11].

3.2 Detonation technique

The most popular method of producing high dosages of ND is detonation synthesis, which involves bursting an explosion mix of substances composed of in a metallic chamber under a mixture of nitrogen, water and carbon dioxide. The diamond fragments effect is afterwards recorded in the chambers [12]. Explosive molecules serve as a carbon supply while also providing energy through fusion method. The following are the several stages of detonation synthesis:

a. Explosions cause panic waves.

b. The decomposition of an explosive substance.

c. Temperature and pressure build rapidly in the room made up of steel to reach point A, called as C-J point (Chapman-Jouguet point).

d. Blasting products begin to increase as pressure and temperature decrease.

e. Carbon nanocluster formation.

f. As crystal growth proceeds, the temperature and pressure drop lower than point C-J, resulting in the generation of liquid nanodroplets from the synthesis of carbon nanoclusters.

g. Assembled Nanodiamonds are gathered from the room's floor and walls.

A reduction in pressure under the diamond-graphite measuring line can affect diamond development through graphite production, hence precise control of room pressure is necessary during the detonation process. The diamond shaft is the result of the blasting strategy, which is made up of 75% NDs (sized 4–5 nm) and the rest of carbon or fossil fuels. Only explosive NDs (length 3.5–6 nm) have already been widely sold among the many forms of UNCDs. Different cooling media, the blasting method produces a carbon production of 4–10% of the explosives weight. The blasting procedure begins with the use of a connection. The complex is the source of many metallic contaminants found in the blast.

The room's walls are covered in dirt (including such metal and other metals). The diamond powder that results is made up of NDs with a mean size of 4–5 nm. These diamonds nanoparticles are commonly arranged in clusters of a few hundreds of nanometers to micrometers in size. The nucleus of the sp^3 carbon atom is put together in a three dimensional cubic lattice in each diamond particle, which explains the NDs' special properties. Contaminants could be found (i) within the ND aggregates or (ii) on the ND's exterior surface. In many of their applications, disassembling the ND levels is required to eliminate any trapped contaminants. Exploding ND combos with random explosives should be the focus of future research. Artificial explosives are used to clarify the assembling method and certify effective headed over the ND particle sizes that result. Explosive NDs with a magnitude of 2.8 nm are produced by using explosives particles (as thin as 40 nm) [13].

3.3 HPHT and high energy ball milling

HPHT is a really appealing method of preserving ND fluorescent Nanodiamonds through electron radiation and subsequent high pressure high temperature microdiamond integration. The incorporation of irradiation and removal of mature HPHT diamonds for the creation of NV center in the diamond lattice are the two primary processes in this approach. The N_2 melts the molten metal in the HPHT reactor and is then injected into the diamond for subsequent crystal formation. For thermos-kinetic reasons, the changed atoms of N_2 remain isolated inside the diamond crystal and are bonded to neighboring atoms in a diamond sequence.

Strong particles drive carbon atoms out of their regular lattice positions upon irradiation by elevated fragments such as neutrons, ions, photons or electrons, creating voids (V) in the diamond line. Annealing, which is usually done at 800°C below vacuum, aids in the transferring of spaces to N_2 atoms, resulting in the formation of N-vacancy centers. By choosing the right time and acceleration separator, separated nanodiamond sizes created for the HPHT technique via ultracentrifugation can be modified (from 4 to 25 nm). Using nitrogen-rich type Ib diamond powders, it is able to enhance the percentage of N-void centers in Nanodiamonds. As a result of decreased spin contamination within and surrounding the nanocrystal, the HPHT technique can create NDs of ultrasmall fluorescent NDs with substantially longer durations of infidelity [14].

3.4 Laser ablation (LA)

With the invention of the ruby laser, the era of laser ablation commenced. In 1987, employing rising pulsing laser beams of water interfaces, to mix nanoparticles (iron oxide) LA was utilized. PLAL (Pulsed laser ablation in liquids) is quickly becoming one of the most popular ways to test pure liquids. Carbon powder is used to physically generate nanodiamonds in areas of contact with solids, liquids, or solids. The PLAL approach merges the advantages of pulse laser deposition with soft chemical lines to generate nanoparticles in the nature of stable colloidal suspensions. This approach entails the laser treatment of an object immersed in a liquid (either one solitary piece of material or crushed powder) (e.g., ether, ethanol, acetone and its compounds). It can combine plasma expansion and contraction with the delivery of specific conditions (such as pressure and temperature) via atomic fluids and liquids. The strength of the laser generated on the target surface is usually greater than 108 W/cm^2, resulting in the target object being released and evaporation. In comparison to carbon wafers or crystal graphite wafers, microcrystalline graphite is often favored as a target. Plasma plume sealing happens after laser plume collision and consequent coagulation cooling to facilitate the production of crystalline nanodiamond. Shock wave and extinguishing operations can be employed to provide suitable conditions for nanodiamond production. The features of effect NDs can be altered by a number of factors, including (a) laser uncontrollable compulsion, laser intensity, and excitation wavelength; (b) solvent; and (c) system temperature and pressure [15]. PLAL is a method that has the potential to be cost-effective. The capillary influence of the curvature of a nanoscale crystalline nucleus on the nucleation and development of nanocrystals is explained using a kinetic way of theory [16].

3.5 Nanodiamond purification method

Nanodiamond integration frequently includes performance and after process procedures designed at purification residues. To deal with two of the most prevalent and most common pollutants, some types of carbon (particularly graphitic) and associated metals and oxides, a number of approaches have been devised. The overall purpose of carbon emissions refining is to discharge selective oxidation by characterized sp^2 carbon reactivity in comparison to sp^3 carbon in the diamond phase. Sustaining a maximum temperature of 400–430°C was used to select sp^2 carbon [17]. In the situation of PLAL NDs, where metal contamination is avoided but the fraction of sp^2 carbon is so high that it becomes a main reaction product, this approach provides a simple and effective solution. The most extensively utilized processes are liquid-phase oxidation reactions. Strong acids are typically used in these processes, which have the additional benefit of removing certain metal-based contaminants. Perchloric acid, concentrated nitric acid, sulfuric acid, hydrochloric acid coupled with nitric acid, and hydrogen fluoride are some examples. Because these therapies demand temperatures between 80 and 200°C, additional equipment is required, adding to the complexity and cost. However, particularly in detonation methods, when metal-based contaminants are included in substantial levels, this is important due to the equipment used in such processes, such as metal blasting rooms [18].

4. Applications of Nanodiamonds

The controlled explosive detonation of carbon-containing explosives is used to produce diamond soot on a wide scale. Manufacturers of ND preludes are actively centering on cost cutting of producing ND sediments by repurposing obsolete devices. There are several methods for producing ND particles with a high sp^3 content from Nanodiamond fragment. These integrate acid treatment of selected sp^2 carbon oxidation in the exploding diamond assistance and detonation release of Nanodiamond sediment in high amount of oxygen environment. In the recent several years, there has been a surge in the use of NDs. The amount of Nanodiamond combinations (e.g., Nanodiamond with graphene, Nanodiamond with polymer, Nanodiamond with metal) confirmed to contain several alluring features such as magnified strength, resistance influence, and heat resistance is particularly impressive.

4.1 Photovoltaic devices

Nanodiamonds compounds have received notable observation in DSSCs (dye-sensitive solar cells). A spectral sensitivity of diamond areas with natural dyes containing-photocurrent of ca. 120 nA/cm^2 under visible light is being reported [19]. The link between the diamond (electron donor) and receiver levels was created using oligothiophene and Suzuki (complete). In addition, photocurrent hire of around 4–6 mA/cm^2 was measured in boron-doped NDs using the same arrangement. Polymer dye-functionalized polycrystalline B-doped Nanodiamonds provide a high density of the current image when used as electrodes in dye sensitized solar cells in a liquid electrolyte solution [20]. The photovoltaic devices which are based on B-doped diamonds shows good current density and open circuit voltage thereby indicating that Nanodiamonds might be used as solar photo-electrodes. Utilizing NDs as optical scatterers in DSSCs enhanced performance significantly at a greater current density. Furthermore, power conversion efficiency has also increased while comparing with pure TiO_2 photo-electrodes [21]. As a result, diamond-based composite materials could be utilized in flat panel displays and solar utensils (**Figure 3**).

4.2 Thin film electronics

Because of their unusual physical and mechanical features, ND-reinforced polymers have recently received a lot of attention. A translucent and bendable fluorinated polymer nanohybrid film with high heat resistance and improved mechanical properties was created using a dissipated ND organo-modified Nanodiamond refill. The existence of tiny lamellae in a fluorinated polymers resulted in the formation of a dense amorphous phase with high brightness. The outer layer of NDs must be covered to ensure structural stability. Electrostatic interactions involving Nanodiamonds and the membrane, regardless of the substrate's structure and shape, are critical for ND replication and similarity. Detonation ND seeds are a good alternative to silicon or glass substrates for CVD diamond films [22]. The effects of bulk ND particles on polymer nano- and micro-fibers had studied [23]. Comparing with polyamide 11, the electrospun nanofibers with elevated Nanodiamonds on these substances (polymer) was assembled into tiny layers results in high mechanical properties. Furthermore, lens in Nanodiamond films are a key matter that cause unacceptable degeneration of Nanodiamond film structures like thermal conductivity, bright light, Young's modulus,

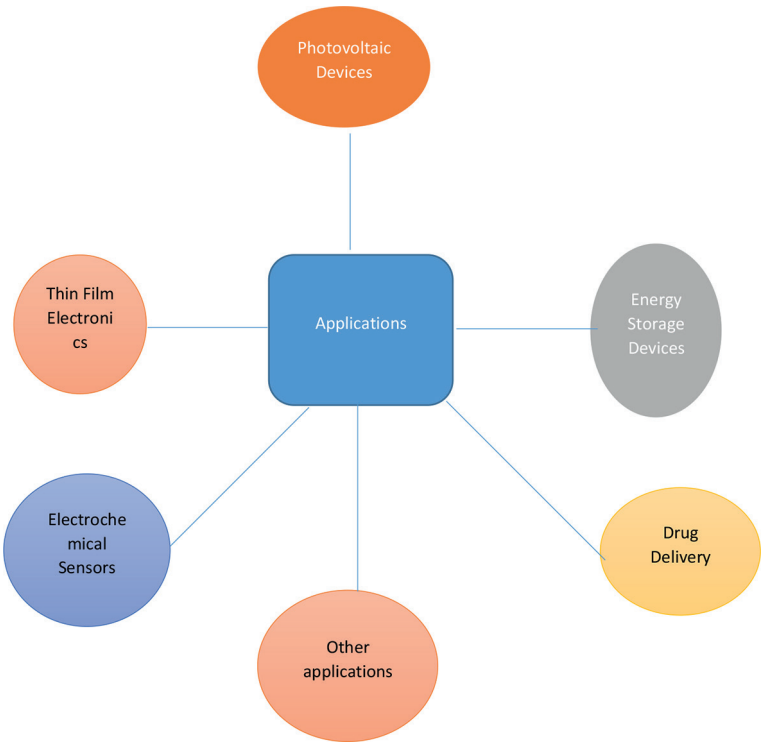

Figure 3.
Applications of Nanodiamonds.

and piezoresistivity [24]. Carbon/carbide interlayer formation, substrate scratch, improved nucleation bias, and electrostatic seeds carrying ND colloid have all been developed for the manufacture of ND films without pinhole ultra-thin ND. Among all of these strategies, the implantation method has demonstrated considerable benefits regarding delivering homogeneous high density and nucleation sites via optimized electrostatic interactions between ND particles and substrate. In a wide range of situations, these reflective coatings even provide UV protection and scratch resistance, particularly in systems which need a unique mix of dielectric, thermal, and mechanical qualities. Based on layer and layer production procedures, detonation Nanodiamond dispersions and ploy vinylalcohol were utilized as 3D printing novels for materials of various shapes. In the consumer electronics business, this three dimensional printing of ND-based polymer compounds leaves the panel open to the creation of tiny solids with complicated forms [25]. Due to the high N-incorporated UNCD feature, ND films additionally include field output elements (i.e., 10 V/mm open field) in addition to these uses. The goal of the research was to pinpoint the precise position (e.g., grain characteristics) of field retrieval in the same nanodiamond environment. The pre-requisite for a high temperature of substrate growth (>800°C) in order to support the n-doping type process is a fundamental restriction of these ND films [26].

4.3 Energy storage devices

The popularity for relatively speaking high power and energy density values, as well as good cycle life, has grown massively in the field of energy storage to assist the

fast expanding businesses of mobile and adaptable digital equipment, e-mobility, and machine tools, and also the growing economies of power grid applications. Due to their flexible applicability, conductivity, surface area, aspect rations, stability, electrochemical potential windows are relatively high in Nanodiamonds which will make this material a desirable choice in energy storage systems. The advancement of ND-based electrode materials has been hastened by the discovery of effective methods for growth of Nanodiamond on conducting layers under sub-atmospheric environments. The Nanodiamond's nature can be changed by using an acceptor type doping substance (boron). Boron-doped diamond electrodes are extremely stable over a long range of operating potentials, even in water. HPHT, PECVD, and ion-implantation procedures are commonly used to dope NDs, with PECVD being the favored method for device construction as it allows both n and p-type Nanodiamonds to manage impurity concentrations [27]. In comparison with carbon containing electrodes or metals, Nanodiamond electrodes (conducting) doped substantially with boron have several interesting properties. Moreover, oxidized Nanodiamond electrodes has a higher capacitive current than hydrogen terminated Nanodiamond electrodes [28]. Surface functionalization of NDs can also be used to boost the ion-storage capacity of Nanodiamond-based electrodes by introducing extra pseudo-capacitive processes [29]. Different techniques, like as plasma and electrochemical treatments, can be used to terminate the surface of NDs with H_2, O_2, or OH groups, allowing for adjustable aqueous and due to the hydrophobic water sorption in anti-adherent scalpels and self-cleaning protective coatings [30]. In other words, the electrical characteristics of ND/electrolyte interfaces can be changed by aligning the energies of interaction levels properly. As a result, NDs have been used in energy-related applications as electrodes.

4.4 Electrochemical sensors

Recently, research has focused on the utilization of NDs to construct new electrochemical nerves for applications like as drug detection, gas monitoring, genetic sequence diagnostics, etc. The high level of electrochemical reaction accuracy, photo-stability and resolution is one of the most important parameters in any sensory system. NDs are a good choice for the sensitivity of electrochemicals because of have unique features, such as durability, chemical resistance, biocompatibility, spin break, fluorescence, and catalytic structures [31]. Different conversion approaches have been developed to improve the sensory function of NDs, including turning NDs into self-assembled monolayers, oxygen plasmas, liquid chemical procedures, metal catalysis and so on. Modified NDs provide optimal melting, as well as special binding to targeted sensory analysts. Using square-wave voltammetry, a sensor (electrochemical) based on scattered Nanodiamonds with glassy carbon electrode (GCE) was reported on pyrazinamide (PZA) sensors [32]. In a typical way, carbon black nanoparticles modified-NDs are constructed to monitor based electrochemical transmitter using cyclic voltammetry, which produces a dopamine sensor with a detection limit of 0.06 mM [33].

4.5 Drug delivery

Biocompatibility, the capacity to hold a wide scope of treatments, water dissipation, and reliability are all requirements for a drug delivery platform. It is also vital to consider the possibility of tailored therapy, which might be used in conjunction with images. A combination of Nanodiamond with Duxorubin (drug used in cancer

treatment) were now used for the treatment in lung cancer, breast cancer, and also it reduced the circulation half time of Nanodiamond Duxorubin complexes [34].

Nanodiamonds are covered with polyethylenimine 800 (PEI800), which has been researched for delivering nucleic acids in addition to delivering tiny molecules. These studies indicated a 70-fold improvement in GFP plasmid transfection efficiency while keeping PEI800's minimal maintenance hazardous properties [35]. In body circumstances, the administration of ND-PEI800 of siRNA suppressing GFP expression was more efficient than lipofectamine (a widely utilized delivery platform). Other loads have been delivered, including combinations of medicines, proteins, tiny molecules in acidic conditions (common in tumors), and cancer-specific siRNA. Although nanodiamonds have mostly been studied as prospective injectable therapeutic agents for broad drug administration, sheets of parylene–nanodiamond composites have been shown to be effective for localized release of drug for durations ranging from 2 days to 1 month.

4.6 Other applications

NDs can provide a suitable foundation for improving the utilization of drug carriers to cure skin cancer because of their great biocompatibility. The inclusion of NDs to beauty products can also allow active compounds to perform to their full capacity due to their high adsorption rate. NDs are able to transport more active chemicals and dive deeper into the skin layers than standard formulations. The higher moisture content capacity of NDs keeps the skin moisturized for longer, in addition to being fully and quickly absorbed by the skin. NDs may also help with healing process and can be used to dress wounds. Because NDs have an elevated surface chemistry that can be modified to aid carry genes and impact cell entrance, ND-based gene delivery systems for healing process seem appealing. Gene transfer is being researched in wound healing to overcome the limited availability of growth factors to the injury site. As an example, Bovine collagen is a biocompatible matrix that acts as a cofactor for tissue repair and serves as a supportive gene therapy vector [36].

A fast-emerging area of research is nanodiamond nanocomposite/polymer with improved thermal and mechanical properties. The nanocomposites that are quickly developing with distributed nanodiamonds were created utilizing a variety of processes, and they are promising for future applications (aeronautical, automotive, membranes, coatings, lubricants). Microelectromechanical systems (MEMS), quantum coherent devices, quantum computing have used nitrogen doped detonation ND nanocomposite. Scanning electron microscopy (SEM), Raman scattering spectroscopy cyclic voltammetry measurements and electrochemical response were used to investigate nanocrystalline diamond nanocomposite. These materials also contain boron doped nanodiamond. Because of its biocompatibility and bioresorbability, nanocomposite has been used to transport medicines and physiologically active compounds. The ability to transport a wide range of treatments is part of the drug delivery podium. In the desired medium, dispersibility and scalability are important. These materials have the potential to be used in bioimaging [37].

The medical applications of a Nanodiamond include imaging (MRI image, fluorescent Nanodiamonds,), tissue engineering (dental applications, bone tissue engineering, skin tissue engineering), drug delivery (cytotoxic drugs, anti-tubercular drugs, anti-diabetic drugs), binding biomolecules (siRNA, β-galacsidase, lysozyme proteins, poly-phenolic compounds). Modified Nanodiamonds can be used as a nucleic acid complexion platform and as a gene delivery vectors. Despite its unique properties, the

Name of the material	Brief description on the area	Reference
Nanodiamonds	Skin treatment, wound healing	[36]
Boron doped Nanodiamond	Transport medicines, physiologically active compounds and bioimaging	[37]
Modified Nanodiamonds	Nucleic acid complexion platform and gene delivery vectors	[38]
Fluorescent molecules with Nanodiamonds	Targeted drug transportation, cancer treatment, protein separation	[39]

Table 1.
Other applications of Nanodiamonds.

idea of improving its compatibility with various solvents and polymers has not been fully investigated. Furthermore, it has been difficult to distribute NDs in a mixture for successful application in the biomedical field until now, thus future research should look into particle complexes for this reason [38].

Some fluorescent molecules have been observed to bind to the NDs for transport, including proteins, antibodies, growth hormones, siRNA and DNA molecules. These are applied in many areas like cancer treatment, targeted drug transportation, protein separation and purification by appropriately modifying NDs. This lays a solid platform for the future development of NDs and their potential clinical application. NDs' biocompatibility and toxicity should be tested on a variety of cell types. More study is needed to understand the potential ramifications on the design of biocompatible Nanodiamonds in order to fulfill the demands of safe nanomedical applications [39].

NDs could be used in a variety of medical and biological applications, including biosensor components, targeted drug delivery, biocompatible composited and implants, and strong solid supports for synthesis of peptides. However, three main applications of NDs have been reported: protein immobilization, fluorescent markers for cell imaging, and medication administration (**Table 1**) [2].

5. Conclusion

Nanodiamonds obtained more attention from the researchers and young scientists in science and technology. Nanodiamonds protrude as an eccentric in several areas. The size and shape of the independent Nanodiamonds are solely responsible for the reproducibility and reliability of Nanodiamond-based products. Without structural or microstructural deterioration, semi or doped ND electrodes can perform successfully in harsh solution conditions. Diamond-based energy-saving machines' ideal performance, which is dependent on their huge window with specific high strength, also has tremendous promise for broad usage in the storage technology community in the near future. Nanodiamond is an essential structural material in addition to being a good functional material. As a structured material, nanodiamond, for instance, has a wide range of uses, including in the oil and gas, semiconductor, and development sectors for tool surface modification, grinding, and polishing. The numerous applications for Nanodiamonds will continue to drive research ahead. Nanodiamonds' structure and surface chemistry will be better understood, which will lead to even more uses.

Nanodiamonds and Its Applications
DOI: http://dx.doi.org/10.5772/.108326

References

[1] Danilenko VV. On the history of the discovery of nanodiamond synthesis. Physics of the Solid State. 2004;**46**(4):595-599. Translated from Fizika Tverdogo Tela. 2004;46(4):581-584

[2] Chauhan S, Jain N, Nagaich U. Nanodiamonds with powerful ability for drug delivery and biomedical applications: Recent updates on in vivo study and patents. Journal of Pharmaceutical Analysis. 2020;**10**:1-12. DOI: 10.1016/j.jpha.2019.09.003

[3] Kumar S, Nehra M, Kedia D, Dilbaghi N, Tankeshwar K, Kim K-H. Nanodiamonds: Emerging face of future nanotechnology. Carbon. 2019;**143**:678-699

[4] Mochalin VN, Shenderova O, Ho D, Gogotsi Y. The properties and applications of Nanodiamonds. Nature Nanotechnology. 2012;7(1):11-23. DOI: 10.1038/NNANO.2011.209

[5] Bradac C et al. Observation and control of blinking nitrogen-vacancy centres in discrete nanodiamonds. Nature Nanotechnology. 2010;**5**:345-349

[6] Vlasov II et al. Nitrogen and luminescent nitrogen-vacancy defects in detonation nanodiamond. Small. 2010;**6**:687-694

[7] Schrand AM, Lin JB, Hens SC, Hussain SM. Temporal and mechanistic tracking of cellular uptake dynamics with novel surface fluorophore-bound nanodiamonds. Nanoscale. 2011;**3**:435-445

[8] Mochalin VN, Gogotsi Y. Wet chemistry route to hydrophobic blue fluorescent nanodiamond. Journal of the American Chemical Society. 2009;**131**:4594-4595

[9] Zhu Y, Li J, Wenxin Li Y, Zhang XY, Chen N, Sun Y, et al. The biocompatibility of Nanodiamonds and their application in drug delivery systems. Theranostics. 2012;**2**(3):302-312. DOI: 10.7150/thno.3627

[10] Zhang XY, Yin JL, Cheng K, et al. Biodistribution and toxicity of nanodiamonds in mice after intratracheal instillation. Toxicology Letters. 2010;**198**:237-243

[11] Basso L, Cazzanelli M, Orlandi M, Miotello A. Nanodiamonds: Synthesis and application in sensing, catalysis, and the possible connection with some processes occurring in space. Applied Sciences. 2020;**10**:4094. DOI: 10.3390/app10124094

[12] Pichot V, Risse B, Schnell F, Mory J, Spitzer D. Understanding ultrafine Nanodiamond formation using nanostructured explosives. Scientific Reports. 2013;**3**:2159

[13] Pichot V, Comet M, Risse B, Spitzer D. Detonation of nanosized explosive: New mechanistic model for nanodiamond formation. Diamond and Related Materials. 2015;**54**:59-63

[14] Su LJ, Fang CY, Chang YT, Chen KM, Yu YC, Hsu JH, et al. Creation of high density ensembles of nitrogen-vacancy centres in nitrogen-rich type Ib Nanodiamonds. Nanotechnology. 2013;**24**:315702

[15] Amans D, Chenus AC, Ledoux G, Dujardin C, Reynaud C, Subtlemontier O, et al. Nanodiamond synthesis by pulsed laser ablation inn liquids. Diamond and Related Materials. 2009;**18**:177-180

[16] Wang CX, Liu P, Cui H, Yang GW. Nucleation and growth kinetics of nanocrystals formed upon pulsed laser ablation in liquid. Applied Physics Letters. 2005;**87**:201913

[17] Bradac C, Osswald S. Effect of structure and composition of nanodiamond powders on thermal stability and oxidation kinetics. Carbon. 2018;**132**:616-622

[18] Aleksenskii A. Technology of preparation of detonation Nanodiamond. In: Detonation Nanodiamonds. Singapore: Pan Stanford Publishing; 2014. pp. 37-72

[19] Zhong YL, Loh KP, Midya A, Chen ZK. Suzuki, coupling of aryl organics on diamond. Chemistry of Materials. 2008;**20**:3137-3144

[20] Krysoca H, Kavan L, Zivcova ZV, Yeap WS, Verstappen P, Maes W, et al. Dye sensitization of boron-doped diamond foam: Champion photo electrochemical performance of diamond electrodes under solar light illumination. RSC Advances. 2015;**5**:81069-81077

[21] Tafti MH, Sadeghzadeh SM. Novel use of nanodiamonds light-scattering material in dye-sensitized solar cells. Journal of Materials Science: Materials in Electronics. 2016;**27**:5225-5232

[22] Montes-GutierrezJA, Alcantar-PenaJJ, de Obaldia E, Zuniga-Rivera NJ, Chernov V, Melendrez-Amavizca R, et al. Afterglow, tehrmoluminescence and optically stimulated luminescence characterization of micro-nano- and ultrananocrystalline diamond films grown on silicon by HFCVD. Diamond and Related Materials. 2018;**85**:117-124

[23] Behler KD, Staravato A, Mochalin V, Korneva G, Yushin G, Gogotsi Y. Nanodiamond-polymer composite fibers and coatings. ACS Nano. 2009;**3**:363-369

[24] Poghossian A, Abouzar MH, Razavi A, Backer M, Bijens N, Williams OA, et al. Nanocrystalline-diamond thin films with high pH and pencillin sensitivity prepared on a capacitive Si-SiO2 structure. Electrochimica Acta. 2009;**54**:5981-5985

[25] Angjellari M, Tamburri E, Montaina L, Natali M, Passeri D, Rossi M, et al. Beyond the concepts of nanocomposite and 3D printing: PVA and nanodiamonds for layer- by-layer additive manufacturing. Materials and Design. 2017;**119**:12-21

[26] Janssen W, Turner S, Sakr G, Jomard F, Barjon J, Degutis G, et al. Substitutional phosphorous incorporation in nanocrystalline CVD diamond thin films. Physica Status Solidi RRL: Rapid Research Letters. 2014;**8**:705-709

[27] Tsubouchi N, Ogura M, Mizouchi N, Watanabe H. Electrical properties of a B doped layer in diamond formed by hot B implantation and high temperature annealing. Diamond and Related Materials. 2009;**18**:128-131

[28] Liu Y, Kim DY. Enhancement of capacitance by electrochemical oxidation of Nanodiamond derived carbon nano-onions. Electrochimica Acta. 2014;**139**:82-87

[29] Wei L, Yushin G. Nanostructured activated carbons from natural precursors for electrical double layer capacitors. Nano Energy. 2012;**1**:552-565

[30] Miele E, Malerba M, Dipalo M, Rondanina E, Toma A, Angelis FD. Controlling wetting and self-assembly dynamics by tailored hydrophobic surfaces. Advanced Materials. 2014;**26**:4179-4183

[31] Baptisa FR, Belhout SA, Giordani S, Quinn SJ. Recent developments in carbon nanomaterial sensors. Chemical Society Reviews. 2015;**44**:4433-4453

[32] Simoni NB, Silva TA, Oliveira GG, Fatbello-Filho O. A Nanodiamond-based electrochemical sensor for the determination of pyrazinamide antibiotic. Sensors and Actuators, B: Chemical. 2017;**250**:315-323

[33] Jiang L, Nelson GW, Abda J, Foord JS. Novel modifications to carbon-based electrodes to improve the electrochemical detection of dopamine. ACS Applied Materials & Interfaces. 2016;**8**:26338-28348

[34] Chow EK et al. Nanodiamond therapeutic delivery agents mediate enhanced chemoresistant tumor treatment. Science Translational Medicine. 2011;**3**:73ra21

[35] Zhang XQ et al. Polymer-functionalized Nanodiamond platforms as vehicles for gene delivery. ACS Nano. 2009;**3**:2609-2616

[36] Namdar R, Nafisi S. Nanodiamond applications in skin preparations. Drug Discovery Today. 2018;**23**(5):1152-1158

[37] Kausar A. Properties and applications of nanodiamond nanocomposite. American Journal of Nanoscience & Nanotechnology Research. 2018;**6**:46-54

[38] Martel-Estrada S-A. Recent progress in biomedical applications of Nanodiamonds. Nanoscience and Nanotechnology. 2018;**8**(1):11-24

[39] Qin J-X, Yang X-G, Lv C-F, Li Y-Z, Liu K-K, Zang J-H, et al. Nanodiamonds: Synthesis, properties, and applications in nanomedicine. Materials & Design. 2021;**210**(15):110091

Chapter 4

Surface Analysis of Graphene and Graphite

Wenjing Xie and Chi-Ming Chan

Abstract

Graphene and graphite are two widely studied carbon materials. Due to their particular properties and structure, graphene and graphite have been used in a variety of fields such as electronic devices and sensors. The surface properties of graphene and graphite as well as their derivatives are strongly connected to the performances of devices and sensors. Thus, it is necessary to choose appropriate surface analysis techniques for characterization, which are not only useful in the understanding of the surface composition and structure but also in the design and development of these types of materials. X-ray photoelectron spectroscopy (XPS) and time-of-flight secondary ion mass spectrometry (ToF-SIMS) have been two of the key surface analysis techniques that are widely used to characterize these surfaces. In this chapter, an overview of the applications of XPS and ToF-SIMS in the study of the surfaces of graphene and graphite is present. We hope that the information provided will simulate more exciting and inspiring research on graphene and graphite and promote practical applications of these carbon materials in the future.

Keywords: graphene, graphite, surface, XPS, ToF-SIMS

1. Introduction

Carbon materials have been widely used to promote technological advances in various applications such as energy storage, catalysis, and sensors. These materials which are mainly composed of carbon atoms exhibit diverse structures and properties depending on the valence bond hybridization of carbon. As a new member of carbon materials, graphene exhibits extraordinary physical and chemical properties. Graphene is a zero-bandgap semiconductor and exhibits room temperature electron mobility, which is much higher than those of silicon or other semiconductors and weakly affected by temperature and doping effect [1]. These properties impart the rapid development of graphene-based transistors or integrated circuits which are considered as a promising alternative to silicon electronics [1, 2]. The first graphene-based circuit was developed by Lin *et al.* in 2011 [3]. The graphene integrated circuit operates as a broadband radio-frequency mixer at frequencies up to 10 gigahertz and exhibits outstanding thermal stability. Graphene is highly optically transparent and absorbs only 2.3% of the incident white light [4]. Graphene also displays the highest thermal conductivity compared to other carbon materials [5]. Thus, graphene has applications for transparent touchscreens, organic light-emitting diodes as well

as solar cells. Large-area, continuous, transparent, and highly conductive graphene, which can be produced by chemical vapor deposition (CVD) method, is used as an anode in photovoltaic devices with a power conversion efficiency of up to 1.71% [6]. The large specific surface area, flexibility, and high electrical conductivity of graphene make it an ideal material for sensors [7]. In particular, the graphene sensor for COVID-19 detection can detect viruses faster and more accurate [7]. For example, a graphene-based field-effect transistor biosensing device was created to detect spike protein on COVID-19 with a limit of detection of 1 fg mL^{-1} [8]. Graphene has a unique two-dimensional (2D) single-sheet structure and is considered a building block of other carbon allotropes. It can be wrapped up into zero-dimensional (0D) fullerene, rolled into one-dimensional (1D) carbon nanotube, or stacked into three-dimensional (3D) graphite [1]. In the graphite structure, each carbon atom is sp^2 hybridized. The highly oriented pyrolytic graphite (HOPG) is a highly-ordered and high-purity form of synthetic graphite. A new HOPG surface can be generated *via* simple tape cleavage. It is an ideal model to be used as a calibration standard for microscopic imaging [9, 10], and a substrate for chemical reactions [11] and surface modifications by laser irradiation and ion beam bombardment [12].

It is well known that the surface physical and chemical properties of materials are quite different from those of their bulks. Many critical physical and chemical reactions occur on surfaces of materials, such as oxidation, contamination, corrosion, and adsorption. As surface properties are governed by the atomic structure and composition of the outermost layer of the surface of a material, it is necessary to use appropriate surface analysis techniques for its characterization. X-ray photoelectron spectroscopy (XPS) is a widely used surface analysis technique with a sampling depth of 2–10 nm because of its simplicity in use and straightforward in data interpretation [13, 14]. It provides nondestructive quantitative information with an accuracy of up to 0.1 at% on the elemental composition and the chemical state of the elements present on the surface of a material. When high-sensitivity elemental analysis and spatial distribution information of chemical species on a surface are needed, an extremely surface-sensitive technique with a sampling depth of approximately 1 nm, the spatial resolution of about 0.1 μm, and low detection limit up to ppm called time-of-flight secondary ion mass spectrometry (ToF-SIMS) is applied [13, 14]. The secondary fragments generated from the surface of a material are related to its surface chemical structure, such as defects and the functional groups at its edges. However, quantitative information can hardly be deduced from the ion intensities and data interpretation is more complicated. Therefore, a combination of XPS and ToF-SIMS can provide complementary details about the chemical information of the surface of a material.

The objective of this chapter is to present an overview of the applications of XPS and ToF-SIMS in the surface characterization of graphene and graphite, including their preparation processes, impurities, surface defects as well as their surface reactions. We hope this chapter will drive a deeper understanding of graphene and graphite surfaces for faster development and wider applications of these types of materials.

2. Synthesis of graphene

The high spatial resolution imaging and chemical specificity of ToF-SIMS make it a suitable tool to investigate the uniformity of graphene and determine the number of graphene layers. The high spatial resolution map using the C_2^- ion as a marker for

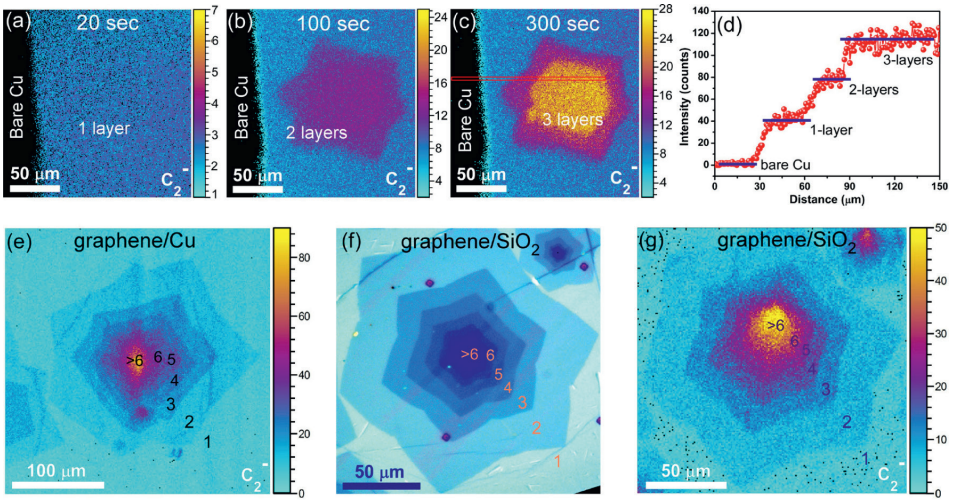

Figure 1.
The C_2^- ion map was reconstructed by accumulating the signals for (a) 20 s, (b) 100 s, and (c) 300 s of Cs^+ sputtering, respectively. (d) A plot of the C_2^- ion intensity integrated from the area line scan is shown in (c). (e) ToF-SIMS C_2^- ion image of graphene on a Cu substrate. (f) Optical image and (g) corresponding ToF-SIMS C_2^- ion image of graphene on a SiO_2/Si substrate [15].

the hexagonal graphene domains provides information about the uniformity of its domains [15]. In addition, ToF-SIMS analysis of multilayer graphene was achieved by cycles of high lateral resolution imaging followed by slow Cs^+ ion sputtering to remove the graphene materials [15]. As shown in **Figure 1**, with 20 s of sputtering time, a uniform graphene layer can be observed, while it takes approximately 100 s of sputtering for the removal of the first layer of graphene. Prolonging the sputtering for a longer time exposes all the buried adlayers underneath the top layer, and thus a total of three layers of graphene can be observed after accumulating C_2^- signals for 300 s of sputtering. The intensity of the C_2^- ion shows a stepwise increase with the number of graphene layers. Particularly, the C_2^- ion intensity at each step shows a linearly proportional increase to the number of graphene layers, and up to six layers of graphene can be distinguished. These results are validated with analogous optical images showing six layers of graphene. The ToF-SIMS chemical image shows its capability of identifying the layer number of graphene on both Si/SiO_2 and Cu substrates.

CVD has been commonly used to grow large-area graphene sheets on various metal substrates [16]. Cu foil is often chosen as a substrate and also a catalyst for monolayer graphene growth [17]. The weak interaction between the graphene and Cu foil allows the graphene films to expand over the grain boundaries with minimal structural disruption, resulting in electron transfer from the Cu foil to the graphene [16, 18]. ToF-SIMS is a suitable technique to determine the chemical structures created from this interaction. It was found that peaks related to the interaction between the graphene and Cu foil substrate, such as C_2Cu^- and C_4Cu^- ions, are present in the ToF-SIMS negative ion spectrum obtained at 450°C [19]. The ToF-SIMS images further verify that the C_2Cu^- ion shows a distribution pattern similar to that of the C_2^- ion, which is a characteristic ion for graphene (**Figure 2**). Two areas (60 μm × 60 μm) from the ToF-SIMS image of the C_2^- ion corresponded to areas with high graphene and Cu concentrations were then picked for analysis. Both the graphene-related peaks, i.e., the C_x^- and C_xH^- (where x=1, 2, 3...) ion series, and

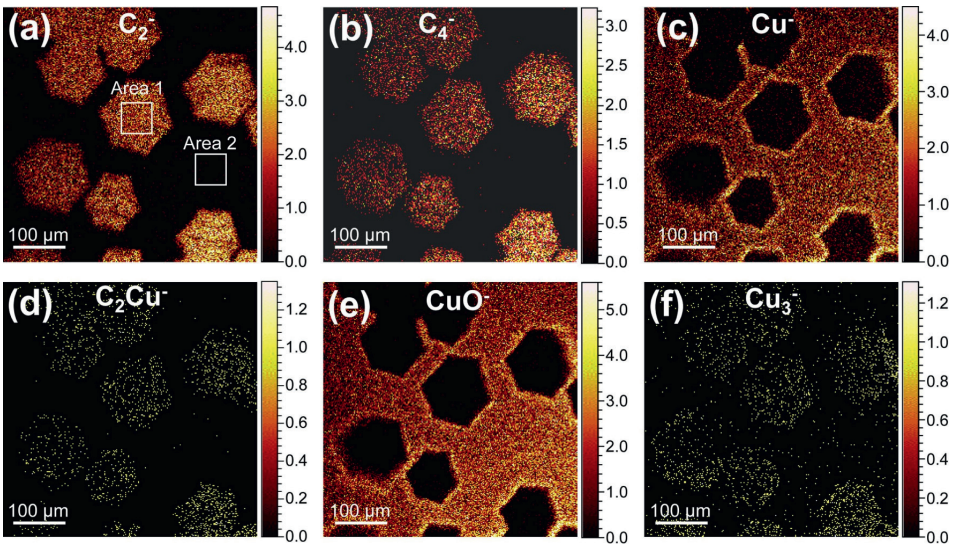

Figure 2.
ToF-SIMS images of different ions of graphene on a Cu foil substrate: (a) C_2^-, (b) C_4^-, (c) Cu^-, (d) C_2Cu^-, (e) CuO^- and (f) Cu_3^- ions [19].

peaks related to the interaction between the graphene and Cu foil substrate (C_xCu^- ion series) have higher intensities in the areas with a higher graphene concentration, confirming the existence of the graphene-Cu interaction at the interface of the graphene and Cu foil substrate.

Moreover, the oxidation protection of graphene for the Cu foil substrate was found when comparing the ToF-SIMS negative ion spectra obtained from the areas with and without graphene coverage [19]. The intensities of the peaks related to the oxidation of the Cu foil substrate, such as the CuO^- and Cu_2O^- ions, are significantly higher in the spectrum obtained from the area without graphene coverage. On the contrary, the ion intensity ratios of Cu cluster ions to the Cu^- ion, such as the Cu_3^-/Cu^- and Cu_4^-/Cu^-, are higher in the area with a higher graphene concentration. The Cu_3^- ion shows a distribution pattern similar to that of the C_2^- ion but complementary to that of the CuO^- ion (**Figure 2**). As the metal cluster ions are usually generated during the sputtering process by direct ejection from a metal surface, it can be anticipated that more Cu cluster ions are formed from pure metal than from its oxides. Therefore, the higher ion intensity ratios of Cu cluster ions to the Cu^- ion in the areas with a high graphene concentration also confirm that less oxidation occurred in the graphene-covered Cu foil substrate than in the uncovered areas. The above results confirm that the growth of graphene on a Cu foil substrate can prevent oxidation of the Cu foil substrate during storage and annealing processes. The graphene on the Cu foil substrate can inhibit the diffusion of small molecules, such as O_2 and H_2O, into the interface between the graphene and Cu foil substrate, thus preventing the oxidation of the copper.

3. Impurities in graphene and graphite

To better measure the optical and electronic properties of graphene, the graphene grown on a Cu foil needs to be transferred onto another target substrate, such as Si wafer or glass. During the transfer processes, a polymer such as poly(methyl methacrylate)

(PMMA) is commonly used as a membrane support to prevent folding or tearing of graphene [20, 21]. Studies have shown that there is still some residual PMMA remaining on the surface of graphene after cleaning by chemical or thermal treatment [22, 23]. When exposed in the air or during XPS and ToF-SIMS measurements at room temperature, the adsorption of hydrocarbon and oxygen contaminants on the graphene and graphite surfaces is very likely. Xie *et al.* developed a process to produce a very clean graphene surface through annealing a graphene sample at 500°C in an ultra-high vacuum chamber without creating any additional defects [24]. XPS was used to estimate the residual PMMA and hydrocarbon contaminants on the graphene surface before and after annealing at different temperatures based on the curve-fitting results. The XPS results indicate that a clean surface was produced after annealing the sample at 500°C for 45 min. A similar experiment was repeated, and the sample was analyzed by ToF-SIMS. After selecting representative ions of PMMA and hydrocarbons from ToF-SIMS spectra, such as $C_2H_3O_2^+$ and CH_3O^- for PMMA and $C_4H_5^+$ for hydrocarbons, and calculating their normalized intensities under different annealing conditions, the results confirmed that the residual PMMA can be removed from the surface of graphene at 400°C, while hydrocarbon contaminants require a higher temperature of 500°C to remove.

Furthermore, by using deuterium isotope-labeled PMMA and ToF-SIMS, the residual PMMA on a graphene surface was identified, located, and quantified. **Figure 3** shows ToF-SIMS depth profiles and high lateral resolution maps of C_3^- ion representing graphene and $^2H^-$ ion representing deuterated-PMMA [25]. As shown in the depth profiles, the $^2H^-$ ion is concentrated on the top surface and its intensity drops when penetrating into the graphene structure. The C_3^- ion increases gradually and reaches a maximum at the depth of about 0.2 nm ($^2H^-$ ion with relatively low intensity), and then gradually decreases when going into the SiO_2 substrate layer. The mapping results, as shown in **Figure 3b** and **c**, indicate that the $^2H^-$ ion appears mainly in the same areas where the C_3^- ion is present, confirming that the residual PMMA is present on the graphene surface.

In addition, metallic impurities introduced during the transfer process can lead to contamination of fabrication devices. The out-diffusing of these impurities toward the substrate during the device processing can result in degradation of the device parts located beneath graphene. ToF-SIMS was used to detect Cu and Fe residuals originating from the transfer process of graphene [26]. The ToF-SIMS images of transferred graphene showed the presence of Cu and Fe residuals on the areas covered with graphene. A comparison of ToF-SIMS mass spectra between the SiO_2/Si

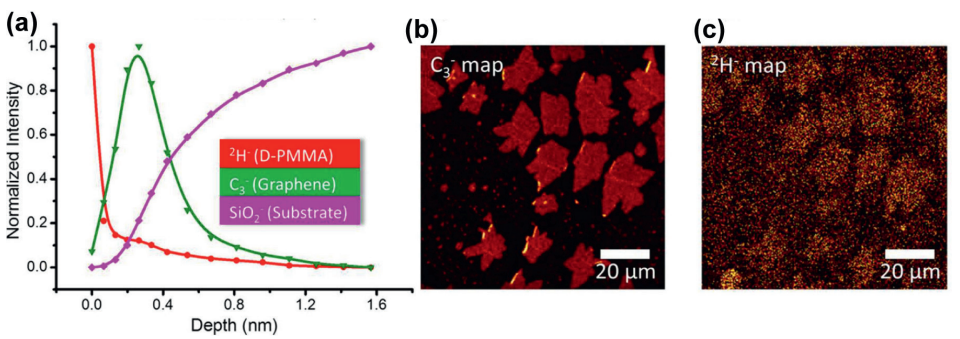

Figure 3.
(a) ToF-SIMS depth profiles of $^2H^-$, C_3^- and SiO_2^- ions. ToF-SIMS images of (b) C_3^- and (c) $^2H^-$ ions [25].

substrates with and without graphene confirmed that the presence of residual metals is related to the graphene transfer process. Combined with total reflection X-ray fluorescence, the residual metal (Cu and Fe) concentrations were calculated to be approximately 10^{13}–10^{14} atoms cm^{-2} regardless of the transfer method.

4. Defects in graphene and graphite

Studies have shown that defects can arise during the preparation process of graphene. The defects in graphene exist in the form of sp^3 carbons with more or less than six carbon atoms in a ring [27]. Usually, one or two H atoms are attached to the sp^3 carbons. The presence of defects in graphene can change its electrical, mechanical and magnetic properties as well as surface chemical reactivities, thus having a significant impact on the performance of graphene-based devices. On the contrary, the surface of HOPG is almost defect-free with only delocalized sp^2 carbons and can be used as a standard model for the study of surface defects on graphene. XPS has been the preferred choice for determining the structures of graphene and graphite surfaces [28]. **Figure 4a** shows an XPS C1s spectrum of HOPG, revealing a narrow main carbon peak with the binding energy at 284.5 eV, accompanied by a broad and asymmetric tail toward higher binding energy [28]. The asymmetry is due to the low energy electron-hole pair excitation as the valence electrons respond to the presence of the core hole. Two empirical approaches have been used to curve fit this asymmetric line shape. The first approach uses an asymmetric Doniach-Sunjic function, which was originally developed for analyzing the asymmetric line shapes of XPS spectra of metals [29], while the other considers HOPG as a neutral alternant hydrocarbon and fits its C1s spectrum with five symmetric components [30]. Xie *et al.* obtained clean HOPG and graphene surfaces by annealing the samples at 500°C in an ultra-high vacuum chamber [28]. A combination of Doniach-Sunjic and Gaussian-Lorentzian functions was used to curve fit the asymmetric C1s spectrum of HOPG. An asymmetric parameter of 0.035 was determined after considering the left full-width-at-half maximum ($FWHM_{left}$) and the right FWHM ($FWHM_{right}$) of the C1s peak. The C1s spectrum of clean HOPG was fitted with two components including the sp^2 carbon peak and the π-π^* shake-up peak (**Figure 4a**). However, for the curve-fitting of C1s spectrum of graphene, a sp^3 carbon peak representing the defects at the binding energy varying between 285.0 and 285.5 eV also appears (**Figure 4b**). To confirm the nature of the sp^3 peak, defects were introduced on the surface of HOPG. An effective way of inducing defects on the surface of HOPG is ion bombardment, in which the defect density can be controlled by varying the ion dose density. Defects created on a HOPG surface can broaden the FWHM of its XPS C1s spectrum and make the line shape on the high-binding-energy side of the peak more asymmetric due to the disorder of its delocalized sp^2 structure and the development of the sp^3 component. **Figure 4c** shows that the FWHM of the C1s peak becomes broader and the sp^3 carbon peak intensifies as more defects were created on the surface of HOPG. The C1s curve of the sputtered HOPG at the take-off angle of 20° (sampling depth about 2.6 nm) showed a higher sp^3 peak intensity compared with that at 90° (sampling depth about 7.5 nm). This result indicates that sp^3 defects which were created by sputtering a defect-free HOPG surface mainly concentrated on the top surface. The atomic ratio of sp^3 carbons to sp^2 carbons in the sputtered HOPG samples determined by XPS was used to estimate the amounts of sp^3 defects. For the HOPG sample, the ratio was close to zero. As the sputtering dose increased, the ratio gradually increased. Note

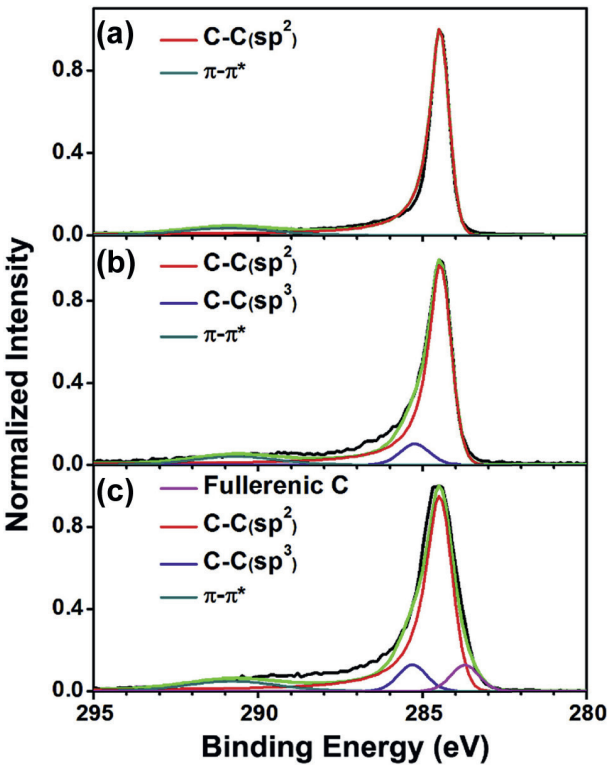

Figure 4.
XPS C1s normalized spectra of (a) HOPG after 500°C annealing, (b) graphene on a SiO_2/Si wafer after washing with acetone and annealing at 500°C, and (c) HOPG after 500°C annealing followed by Ar^+ sputtering with a sputtering dose of 5.0 × 10^{15} ions cm^{-2}. The black (—) and green (—) lines represent the experimental and curve-fitted spectra, respectively. All spectra were obtained at 500°C at a take-off angle of 20° [28].

that sputtering creates defects but at the same time also removes the defects from the surface. As a result, the ratio eventually reached a constant value when the rate of defect generation equaled the rate of defect removal.

The defects in graphene can also be characterized using ToF-SIMS [28]. A comparison between the ToF-SIMS spectra of graphene and HOPG shows similar ions, including C_x^+, C_xH^+, C_x^-, and C_xH^- (**Figure 5**). The typical fragment ions of graphene and HOPG can be categorized into several types. The C_x^+ and C_x^- ion series are the type that mainly comes from the direct breaking up of the sp^2 areas of graphene and HOPG surfaces. The H-containing fragment ions (C_xH^+ and C_xH^-) form another type of typical fragment ions of graphene and HOPG. The C_xH^+ and C_xH^- ions contain at least one hydrogen which would normally be absent from a defect-free graphene or HOPG surface. Their presence in the spectra suggests that they were created *via* direct ejection of the carbons at or near the defect areas of the graphene and HOPG surfaces. Since graphene has many more defects on its surface, the probability of formation of the C_xH^+ and C_xH^- ions in graphene is higher, leading to their higher normalized intensities. Another major difference between the spectra of graphene and HOPG is that $C_xH_2^{+\cdot}$ ions are present in the positive ion spectrum of graphene but absent in the spectrum of clean HOPG. Therefore, it was suspected that the $C_xH_2^{+\cdot}$ ions might be generated at or near a defect in graphene. To further determine the origin of $C_xH_2^{+\cdot}$ ions, ion bombardment was carried out to create defects on a HOPG surface.

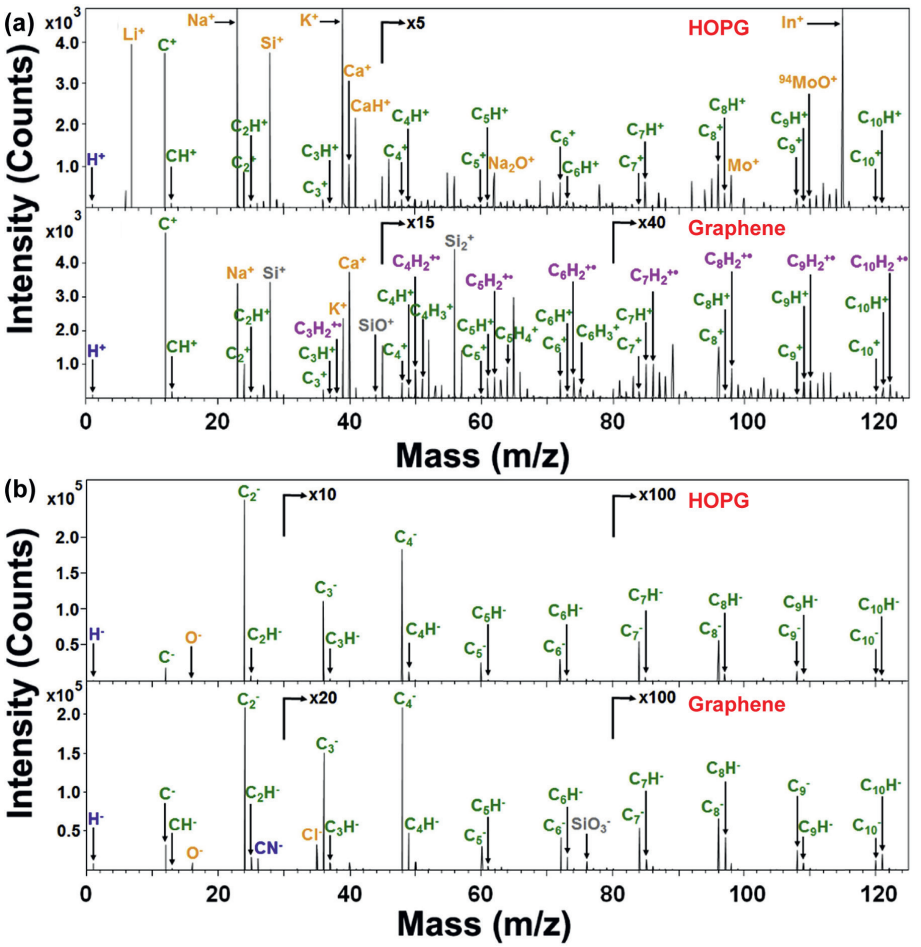

Figure 5.
ToF-SIMS (a) positive and (b) negative ion spectra of HOPG after annealing at 500°C and graphene on a SiO_2/Si wafer after washing with acetone and annealing at 500°C. All spectra were obtained at 500°C [28].

A detailed examination of the positive ion spectra of ion-bombarded HOPG surfaces reveals the presence of the $C_xH_2^{+\cdot}$ ions, confirming that these ions originated from the defects created on the sputtered HOPG surfaces. Therefore, the $C_xH_2^{+\cdot}$ ions can be used as an indicator for the existence of defects in graphene and graphite surfaces.

Studies have shown that defects on graphite and graphene surfaces can be repaired under a carbon atmosphere, a noble gas atmosphere, or in a vacuum [31–33]. The repairs can improve their thermal and electrical conductivities and enhance their mechanical strength. Xie *et al.* revealed that the defects created on the surface of HOPG by ion bombarding can be repaired through high-temperature annealing [34]. Both XPS and ToF-SIMS were applied to monitor the creation and repair of defects in a HOPG surface. The ratio of sp^3 to sp^2 carbons was calculated from XPS results for the HOPG surface before and after sputtering as well as the sputtered HOPG surface after annealing under Ar at different temperatures. These results are shown in **Figure 6a**. This ratio is close to zero for the HOPG and increases to about 0.09 after a dose of 5.8×10^{15} ions cm^{-2} sputtering. After annealing at either 500 or 650°C, the ratio remains the same, but annealing at 800°C reduces the ratio to about zero. Therefore, defects on the surface of

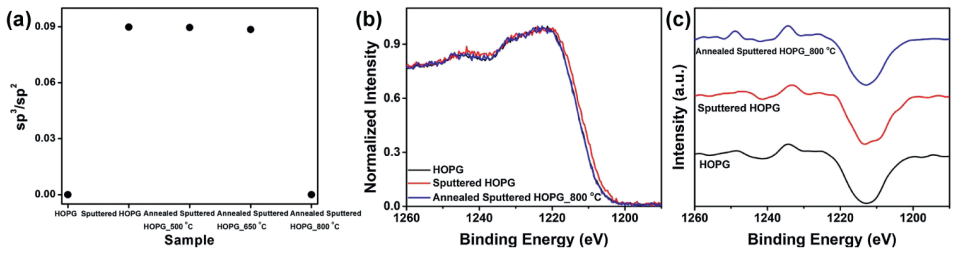

Figure 6.
(a) The ratio of sp^3 to sp^2 carbons in the fresh HOPG sample, HOPG after Ar^+ sputtering at a dose of 5.8 × 10^{15} ions cm^{-2} and after annealing in Ar at different temperatures. (b) C KLL spectra of the fresh, sputtered, and annealed HOPGs and (c) their first derivatives obtained at 500°C [34].

the sputtered HOPG can be repaired by annealing at 800°C in Ar. The ratio of the sp^3 to sp^2 carbons can be estimated using the distance between the most positive maximum and the most negative minimum of the first derivative of an XPS C KLL spectrum which is referred to as the D parameter [35, 36]. For HOPG, this value varies from 21.2 to 23.1 eV [35, 36]. As shown in **Figure 6b** and **c**, the calculated D parameters are 21.3 and 20.1 eV for the fresh and sputtered HOPG, respectively. The decrease of the D value implies an increase in the number of sp^3 carbons on the surface. After annealing at 800°C in Ar, the D value is 21.6 eV, which is similar to that of the fresh HOPG. The recovery of the D value for sputtered HOPG after annealing again implies the conversion of the sp^3 carbons which are present as defects on the sputtered sample to sp^2 carbons through annealing.

ToF-SIMS spectra were obtained from the surfaces of HOPG before and after Ar^+ sputtering and the sputtered HOPG sample after annealing under flowing Ar at different temperatures [34]. The normalized intensity of the $C_xH_2^{+\cdot}$ ions was used as an indicator to reveal the concentration of the defects on the HOPG surfaces. It is obvious that the intensity of these ions was close to zero for the fresh HOPG because it is a defect-free surface. Interestingly, the intensity of these ions for the sputtered HOPG increased, indicating the creation of defects; while the intensity of these ions for sputtered HOPG after annealing at 800°C was close to zero except for the $CH_2^{+\cdot}$ and $C_2H_2^{+\cdot}$ ions, suggesting the healing of these defects created by sputtering.

5. Reactions on the surfaces of graphene and graphite

The performances of different reactions on graphene and graphite such as catalysis, oxidation and reduction, as well as functionalization, are dependent on their surface properties, which are the primary areas of interest. N-doped carbon materials are promising catalysts that exhibit high electrocatalytic activity for the oxygen reduction reaction with high durability [37]. By using HOPG as a model, several types of N-doped HOPG model catalysts were created to investigate the active sites in the oxygen reduction reaction [38]. These N-doped HOPG models included clean-HOPG, Ar^+ ion sputtered HOPG and HOPG modified with different types of N such as pyridinic and graphitic N on the surface. The introduction of different types of N on the HOPG surface was verified by a least-square curve fitting analysis of XPS N1s spectra. The pyridinic N and graphitic N component peaks were assigned at 398.5 and 401.1 eV, respectively. The active sites of the N-doped HOPG surface were then subjected to oxygen reduction reaction and followed by XPS characterization. It was found that

the concentration of pyridinic N decreased, while the concentration of pyridonic N increased. This result suggests that the C atom next to pyridinic N is the active site, which reacts with the OH species formed during the oxygen reduction reaction, accompanied by the transformation of the pyridinic N to the pyridonic N.

Surface functionalization of graphene and graphite is also an essential process to enable them to be used for various applications owing to the changes of the surface chemistry such as hydrophobicity and hydrophilicity. For example, hydrogenation reaction is a common way to introduce C-H bonds on the surfaces of graphene and graphite by converting sp^2 carbons to sp^3 carbons [39]. Birch reduction has been used to convert localized sp^2 carbons to sp^3 carbons at the edges of the graphite surface without creating additional defects in the graphite structure [40, 41]. **Figure 7a** shows a comparison of C1s spectra of graphite powder and hydrogenated graphite powder and a curve-fitting analysis of the two spectra. From the XPS measurements of graphite and hydrogenated graphite powders annealed at 500°C, the binding energy of the C1s main peak of the hydrogenated graphite powder shifted by 0.4 eV toward the high-binding-energy compared to that of the graphite powder [42]. In the C1s spectrum of the graphite powder, only a dominant component peak representing sp^2 carbons and a small component peak representing sp^3 carbons are observed. The decrease and increase in the intensity of the sp^2 and sp^3 carbon component peaks, respectively, observed in the C1s spectrum of the hydrogenated graphite powder confirm the conversion of sp^2 to sp^3 carbons. However, one key disadvantage of using XPS in the above analysis is that XPS cannot detect H and exactly confirm the increase in the hydrogen concentration on a hydrogenated graphite powder surface. By contrast, ToF-SIMS is extremely sensitive to hydrogen and can be used for this purpose instead. Both the ToF-SIMS negative ion spectra of graphite and hydrogenated graphite powders show C_x^- and C_xH^- ion series; nevertheless, the major difference between these two spectra is the increase of normalized intensities of the H^- and C_xH^- ions after hydrogenation (**Figure 7b**), strongly indicating a higher concentration of hydrogen on the hydrogenated graphite powder surface.

Functionalization of graphene and graphite usually involves oxidation of their surfaces by different processes [43]. Graphene and graphite oxides are compounds consisting of carbon, oxygen and hydrogen with different ratios, obtained by

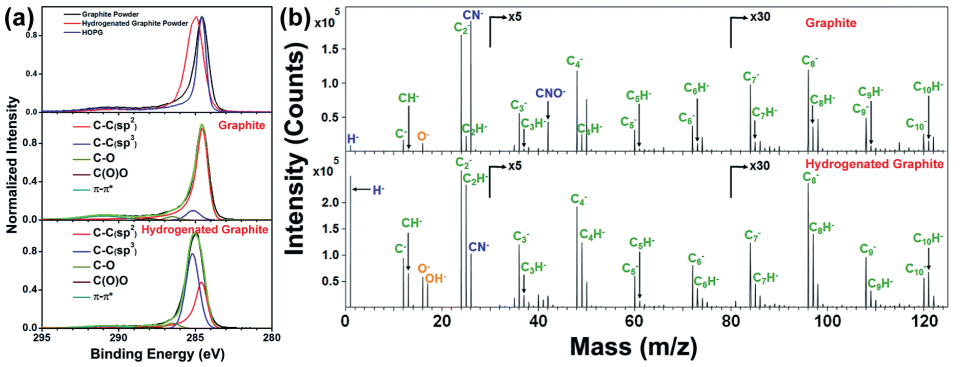

Figure 7.
(a) A comparison of the XPS C1s spectra of the HOPG, graphite powder and hydrogenated graphite powder, XPS C1s curve-fitting results for graphite powder and hydrogenated graphite powder after annealing at 500°C. The black (—) and green (—) lines represent the experimental and curve-fitted spectra, respectively. (b) ToF-SIMS negative ion spectra of graphite powder and hydrogenated graphite powder after annealing at 500°C [42].

treating graphite with strong oxidizers. One common method to produce graphene and graphite oxides is the modified Hummers' method (MHM) [44, 45]. The oxidation results in incorporation of hydroxyl and epoxy groups into the basal plane and carboxyl groups at the edges of graphene and graphite [46]. The existence of these functional groups, of which the chemical states and concentrations, can be determined by XPS. One of the key difficulties to differentiate between hydroxyl and epoxy groups is due to their similar C1s binding energies. To solve this problem, chemical derivatization XPS has been commonly used. Trifluoroacetic anhydride (TFAA) chemical derivatization has been applied to quantify the hydroxyl groups on different surfaces [47, 48]. TFAA mainly reacts with the hydroxyl groups, leading to the formation of CF_3 and ester carbons with identical concentrations on the surface (**Figure 8a**). After the TFAA derivatization, the peak, which originally corresponds to epoxy and hydroxyl groups, becomes mainly associated with the epoxy groups. Following this ideal, graphite oxide powder was first prepared using the MHM. The surface of this resulting graphite oxide powder was analyzed by XPS and the results show that the surface mainly consists of C (74.4 at%) and O (25.2 at%) [49]. After the labeling of the hydroxyl groups with TFAA, a small decrease of the C-O concentration is observed as shown in **Figure 8b**, and only 1.4 at% of F was detected. According to the reaction mechanism, the reaction between one TFAA molecule and one hydroxyl group introduces three F atoms on surface, this means that the carbons representing the hydroxyl groups should be less than 0.5 at% and the C-O component peak in the C1s spectrum of graphite oxide powder is mostly due to epoxy groups on the surface.

The oxygen-containing functional groups on the surfaces of graphene and graphite oxides can be further modified with different molecules through covalent or noncovalent bonds. Theoretical calculations have shown that the epoxy groups on graphene and graphite oxide surfaces play an important role in the reactions with different gases, such as oxidizing SO_2 to SO_3 at room temperature [50]. Based on the XPS result showing that graphite oxide powder prepared using the MHM contains epoxy groups, the reaction between the graphite oxide powder prepared by MHM and SO_2 was carried out [49]. The reaction between the graphite oxide powder and SO_2 produced about 3.8 at% of S on its surface. A comparison of the spectra (**Figure 9a** and **b**) of

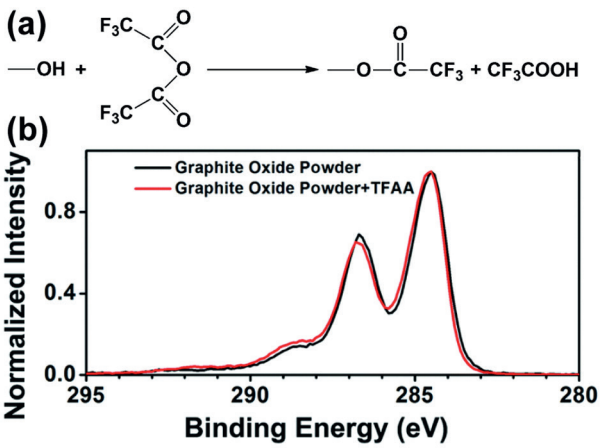

Figure 8.
(a) Reaction mechanism between TFAA and the hydroxyl group on a surface. (b) A comparison of C1s spectra of graphite oxide powder before and after the reaction with TFAA at 25°C [49].

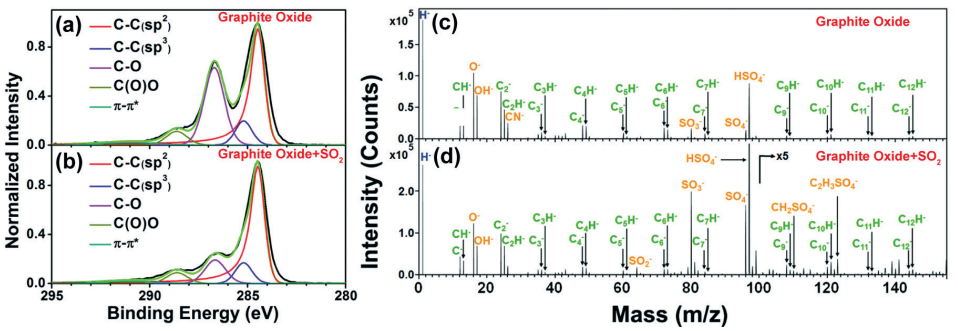

Figure 9.
XPS C1s normalized spectra of graphite oxide powder (a) before and (b) after the reaction with SO_2 obtained at 25°C. The black (—) and green (—) lines represent the experimental and curve-fitted spectra, respectively. ToF-SIMS negative ion spectra of graphite oxide powder (c) before and (d) after the reaction with SO_2 obtained at 25°C [49].

graphite oxide powder before and after the reaction shows that the C-O peak decreases while peak representing the carboxyl group almost stays the same after the reaction, suggesting that the SO_2 mainly reacts with the epoxy groups to produce the C-O-SO_3H groups. ToF-SIMS spectra of graphite oxide powder before and after the reaction with SO_2 were acquired. The C_x^- and C_xH^- ion series representing the graphite peaks are the dominant components in the ToF-SIMS negative ion spectrum of graphite oxide powder (**Figure 9c**). After the reaction between the graphite oxide powder and SO_2, the sulfate-related peaks, such as HSO_4^- and SO_4^-, become the dominant peaks in the spectrum (**Figure 9d**). The changes can also be seen from the increase of normalized ion intensities of HSO_4^-, SO_4^- and SO_3^- ions after the reaction with SO_2. In addition, the intensities of $CH_2SO_4^-$ and $C_2H_3SO_4^-$ ions also increase, indicating that most of the SO_2 had reacted at and attached to the oxidation sites on the surface of the graphite oxide powder. In summary, the epoxy groups on the surface of the graphite oxide powder are responsible for the oxidation of SO_2 into bisulfate.

6. Conclusions

Graphene and graphite have been widely used in various applications owing to their special properties and structures. In particular, the surface properties of graphene and graphite are vital to the performance of many products utilizing these materials. XPS and ToF-SIMS are two main surface analysis techniques that have been used extensively and successfully to study the composition, structure, cleanliness, defects, and reactions of graphene and graphite surfaces. XPS is widely used to yield quantitative elemental and chemical state information of graphene and graphite surfaces. ToF-SIMS provides chemical composition and detailed molecular structure information of graphene and graphite surfaces with high sensitivity. A combination of XPS and ToF-SIMS has been shown to provide complementary information allowing a full and in-depth understanding of graphene and graphite surfaces, which facilitates the transition from fundamental research to practical applications.

Surface Analysis of Graphene and Graphite
DOI: http://dx.doi.org/10.5772/.108203

References

[1] Geim AK, Novoselov KS. The rise of graphene. Nature Materials. 2007;**6**:183-191

[2] Schwierz F. Graphene transistors. Nature Nanotechnology. 2010;**5**:487-496

[3] Lin Y-M, Valdes-Garcia A, Han S-J, Farmer DB, Meric I, Sun Y, et al. Wafer-scale graphene integrated circuit. Science. 2011;**332**:1294-1297

[4] Nair RR, Blake P, Grigorenko AN, Novoselov KS, Booth TJ, Stauber T, et al. Fine structure constant defines visual transparency of graphene. Science. 2008;**320**:1308-1308

[5] Balandin AA, Ghosh S, Bao W, Calizo I, Teweldebrhan D, Miao F, et al. Superior thermal conductivity of single-layer graphene. Nano Letters. 2008;**8**:902-907

[6] Wang Y, Chen X, Zhong Y, Zhu F, Loh KP. Large area, continuous, few-layered graphene as anodes in organic photovoltaic devices. Applied Physics Letters. 2009;**95**:063302

[7] Liu J, Bao S, Wang X. Applications of graphene-based materials in sensors: A review. Micromachines. 2022;**13**:184

[8] Seo G, Lee G, Kim MJ, Baek S-H, Choi M, Ku KB, et al. Rapid detection of COVID-19 causative virus (SARS-CoV-2) in human nasopharyngeal swab specimens using field-effect transistor-based biosensor. ACS Nano. 2020;**14**:5135-5142

[9] Chang H, Bard AJ. Observation and characterization by scanning tunneling microscopy of structures generated by cleaving highly oriented pyrolytic graphite. Langmuir. 1991;**7**:1143-1153

[10] Mándi G, Teobaldi G, Palotás K. Contrast stability and 'stripe' formation in scanning tunnelling microscopy imaging of highly oriented pyrolytic graphite: The role of STM-tip orientations. Journal of Physics. 2014;**26**:485007

[11] Yang S, Tsai P, Kooij ES, Prosperetti A, Zandvliet HJW, Lohse D. Electrolytically generated nanobubbles on highly orientated pyrolytic graphite surfaces. Langmuir. 2009;**25**:1466-1474

[12] Lu X, Huang H, Nemchuk N, Ruoff RS. Patterning of highly oriented pyrolytic graphite by oxygen plasma etching. Applied Physics Letters. 1999;**75**:193-195

[13] Chan C-M, Weng L-T. Applications of X-ray photoelectron spectroscopy and static secondary ion mass spectrometry in surface characterization of copolymers and polymers blends. Reviews in Chemical Engineering. 2000;**16**:341-408

[14] Chan C-M, Weng L-T. Surface characterization of polymer blends by XPS and ToF-SIMS. Materials. 2016;**9**:655

[15] Abidi IH, Weng L-T, Wong CPJ, Tyagi A, Gan L, Ding Y, et al. New approach to unveiling individual atomic layers of 2D materials and their heterostructures. Chemistry of Materials. 2018;**30**:1718-1728

[16] Mattevi C, Kim H, Chhowalla M. A review of chemical vapour deposition of graphene on copper. Journal of Materials Chemistry. 2011;**21**:3324-3334

[17] Li X, Cai W, An J, Kim S, Nah J, Yang D, et al. Large-area synthesis of high-quality and uniform graphene films on copper foils. Science. 2009;**324**:1312-1314

[18] Khomyakov PA, Giovannetti G, Rusu PC, Brocks G, van den Brink J, Kelly PJ. First-principles study of the interaction and charge transfer between graphene and metals. Physical Review B. 2009;**79**:195425

[19] Xie W, Haider Abidi I, Luo Z, Weng L-T, Chan C-M. Characterization of the interaction between graphene and copper substrate by time-of-flight secondary ion mass spectrometry. Applied Surface Science. 2021;**544**:148950

[20] Suk JW, Kitt A, Magnuson CW, Hao Y, Ahmed S, An J, et al. Transfer of CVD-grown monolayer graphene onto arbitrary substrates. ACS Nano. 2011;**5**:6916-6924

[21] Li X, Zhu Y, Cai W, Borysiak M, Han B, Chen D, et al. Transfer of large-area graphene films for high-performance transparent conductive electrodes. Nano Letters. 2009;**9**:4359-4363

[22] Pirkle A, Chan J, Venugopal A, Hinojos D, Magnuson CW, McDonnell S, et al. The effect of chemical residues on the physical and electrical properties of chemical vapor deposited graphene transferred to SiO_2. Applied Physics Letters. 2011;**99**:122108

[23] Lin Y-C, Jin C, Lee J-C, Jen S-F, Suenaga K, Chiu P-W. Clean transfer of graphene for isolation and suspension. ACS Nano. 2011;**5**:2362-2368

[24] Xie W, Weng L-T, Ng KM, Chan CK, Chan C-M. Clean graphene surface through high temperature annealing. Carbon. 2015;**94**:740-748

[25] Wang X, Dolocan A, Chou H, Tao L, Dick A, Akinwande D, et al. Direct observation of poly(methyl methacrylate) removal from a graphene surface. Chemistry of Materials. 2017;**29**:2033-2039

[26] Lupina G, Kitzmann J, Costina I, Lukosius M, Wenger C, Wolff A, et al. Residual metallic contamination of transferred chemical vapor deposited graphene. ACS Nano. 2015;**9**:4776-4785

[27] Batzill M. The surface science of graphene: Metal interfaces, CVD synthesis, nanoribbons, chemical modifications, and defects. Surface Science Reports. 2012;**67**:83-115

[28] Xie W, Weng L-T, Ng KM, Chan CK, Chan C-M. Defects of clean graphene and sputtered graphite surfaces characterized by time-of-flight secondary ion mass spectrometry and X-ray photoelectron spectroscopy. Carbon. 2017;**112**:192-200

[29] Doniach S, Sunjic M. Many-electron singularity in X-ray photoemission and X-ray line spectra from metals. Journal of Physics C: Solid State Physics. 1970;**3**:285-291

[30] Yang DQ, Sacher E. s-p hybridization in highly oriented pyrolytic graphite and its change on surface modification, as studied by X-ray photoelectron and Raman spectroscopies. Surface Science. 2002;**504**:125-137

[31] Kholmanov IN, Edgeworth J, Cavaliere E, Gavioli L, Magnuson C, Ruoff RS. Healing of structural defects in the topmost layer of graphite by chemical vapor deposition. Advanced Materials. 2011;**23**:1675-1678

[32] Zion E, Butenko A, Kaganovskii Y, Richter V, Wolfson L, Sharoni A, et al. Effect of annealing on Raman spectra of monolayer graphene samples gradually disordered by ion irradiation. Journal of Applied Physics. 2017;**121**:114301

[33] Huang Q, Li J, Liu R, Yan L, Huang H. Surface morphology and microstructure evolution of IG-110

graphite after xenon ion irradiation and subsequent annealing. Journal of Nuclear Materials. 2017;**491**:213-220

[34] Xie W, Weng L-T, Yeung KL, Chan C-M. Repair of defects created by Ar^+ sputtering on graphite surface by annealing as confirmed using ToF-SIMS and XPS. Surface and Interface Analysis. 2018;**50**:851-859

[35] Lesiak B, Zemek J, Houdkova J, Kromka A, Oacute ZA. Electron spectra line shape analysis of highly oriented pyrolytic graphite and nanocrystalline diamond. Analytical Sciences. 2010;**26**:217-222

[36] Mezzi A, Kaciulis S. Surface investigation of carbon films: From diamond to graphite. Surface and Interface Analysis. 2010;**42**:1082-1084

[37] Dai L, Xue Y, Qu L, Choi H-J, Baek J-B. Metal-free catalysts for oxygen reduction reaction. Chemical Reviews. 2015;**115**:4823-4892

[38] Guo D, Shibuya R, Akiba C, Saji S, Kondo T, Nakamura J. Active sites of nitrogen-doped carbon materials for oxygen reduction reaction clarified using model catalysts. Science. 2016;**351**:361-365

[39] Nikitin A, Näslund L-Å, Zhang Z, Nilsson A. C-H bond formation at the graphite surface studied with core level spectroscopy. Surface Science. 2008;**602**:2575-2580

[40] Yang Z, Sun Y, Alemany LB, Narayanan TN, Billups WE. Birch reduction of graphite. Edge and interior functionalization by hydrogen. Journal of the American Chemical Society. 2012;**134**:18689-18694

[41] Pekker S, Salvetat JP, Jakab E, Bonard JM, Forró L. Hydrogenation of carbon nanotubes and graphite in liquid ammonia. The Journal of Physical Chemistry B. 2001;**105**:7938-7943

[42] Xie W, Ng KM, Weng L-T, Chan C-M. Characterization of hydrogenated graphite powder by X-ray photoelectron spectroscopy and time-of-flight secondary ion mass spectrometry. RSC Advances. 2016;**6**:80649-80654

[43] Zhu Y, Murali S, Cai W, Li X, Suk JW, Potts JR, et al. Graphene and graphene oxide: Synthesis, properties, and applications. Advanced Materials. 2010;**22**:3906-3924

[44] Dimiev AM, Tour JM. Mechanism of graphene oxide formation. ACS Nano. 2014;**8**:3060-3068

[45] Poh HL, Šaněk F, Ambrosi A, Zhao G, Sofer Z, Pumera M. Graphenes prepared by Staudenmaier, Hofmann and Hummers methods with consequent thermal exfoliation exhibit very different electrochemical properties. Nanoscale. 2012;**4**:3515-3522

[46] Dreyer DR, Park S, Bielawski CW, Ruoff RS. The chemistry of graphene oxide. Chemical Society Reviews. 2010;**39**:228-240

[47] Rinsch CL, Chen X, Panchalingam V, Eberhart RC, Wang J-H, Timmons RB. Pulsed radio frequency plasma polymerization of allyl alcohol: Controlled deposition of surface hydroxyl groups. Langmuir. 1996;**12**:2995-3002

[48] Chilkoti A, Ratner BD, Briggs D. Plasma-deposited polymeric films prepared from carbonyl-containing volatile precursors: XPS chemical derivatization and static SIMS surface characterization. Chemistry of Materials. 1991;**3**:51-61

[49] Xie W, Weng L-T, Chan C-K, Yeung KL, Chan C-M. Reactions of SO_2 and NH_3 with epoxy groups on the surface of graphite oxide powder. Physical Chemistry Chemical Physics. 2018;**20**:6431-6439

[50] Cen W, Hou M, Liu J, Yuan S, Liu Y, Chu Y. Oxidation of SO_2 and NO by epoxy groups on graphene oxides: The role of the hydroxyl group. RSC Advances. 2015;**5**:22802-22810

Chapter 5

Growth of Diamond Thin Film and Creation of NV Centers

Yaping Ma, Junbo Chen and Chenhui Wang

Abstract

Nitrogen-vacancy (NV) center is one type of special defects in diamonds. NV center not only can be used as sensors for temperature, stress detection, magnetic field, etc., but also has potential applications for quantum computing due to its unique physical properties. Therefore, the growth of diamond and creation of NV centers are significant for the future technologies. In this chapter, some methods for growing diamond thin film are introduced first, including traditional high-pressure-high-temperature (HPHT) and chemical vapor deposition (CVD) methods. The second part will focus on the current commonly used approaches to create NV centers. Inter-growth and post-growth processes are mainly utilized for the creation of NV centers during and after the growth of thin film, respectively.

Keywords: diamond growth, NV center, physical properties, high-pressure-high-temperature, chemical vapor deposition, growth mechanism, inter-growth, post-growth

1. Introduction

Diamond, composed of carbon elements, is an allotrope of graphene. Diamond, which is the hardest substance on earth, possesses high electron and hole mobility, the highest known thermal conductivity, extremely low thermal coefficient of thermal expansion, and a wide band gap and optical transparency window spanning from the near ultraviolet to the far infrared (IR), and chemical inertness, which make it a unique and desirable solid-state material for several forefront technological applications, especially in the quantum field [1, 2].

In 1963, it was discovered that diamond nanoparticles can be synthesized by the detonation of carbon-based explosives [2]. Since then, a new pathway has been opened to synthesize diamonds. High-temperature-high-pressure, chemical vapor deposition (CVD), and other methods for synthesizing diamond are being developed. It was not until 1965 that Dyer et al. discovered the nitrogen-vacancy center (NV center) with good optical properties and long coherence time of electron spin to rapidly push diamond to the research upsurge, including catalysis, biomedicine, quantum computing, etc [3]. The negatively charged NV centers in diamond have great potential applications in quantum sensing and quantum communication due to their unique long coherence time.

Nowadays, the method of synthesizing nitrogen-doped diamond has been developed rapidly. In the synthesis process of diamond, high-pressure-high-temperature (HPHT) and chemical vapor deposition methods will be introduced. After diamond synthesis, femtosecond laser, electron irradiation, and ion implantation methods can be used for nitrogen doping. However, the current approaches still cannot synthesize NV centers with high permutations. Not only that, the concentration of NV centers is not very high, and the coherence time is only on the order of milliseconds [4]. Therefore, we have to face a lot of challenges to overcome, and the NV centers still requires further studies.

2. Physical properties of NV center in diamond and their potential applications

The NV center is a unique defect in diamond, made up of a substitutional nitrogen atom (N) and a vacancy (V) at one of the closest neighboring sites of the diamond crystal lattice (**Figure 1a**) [6]. The neutral state NV0 and the negatively charged state NV-, which have extremely different optical and spin characteristics, are the two distinct varieties of this defect that have been discovered so far [7, 8]. Only the negatively charged state of the defect (NV^-) is interesting for quantum computing and sensing, since it can provide a spin triplet ground level which can be initialized, coherently manipulated with long coherence time and readout by pure optical techniques. The followings will focus on the negative charge defect NV^- (denoted as NV center defect).

This C_{3v} symmetry defect behaves like an artificial atom nested in the diamond matrix and exhibits a broadband photoluminescence (PL) emission with a zero-phonon line at 1.945 eV (λ_{ZPL} = 637 nm), making it possible to detect individual NV center using optical confocal microscopy at room temperature [9, 10]. Furthermore, the NV centers exhibit perfect photostability without photobleaching or blinking, which can enable the construction of very reliable single-photon sources operating at room temperature and be applied in biology, where NV defects are used as fluorescent labels [11–13]. In addition, the ground level with a spin triplet state $^3A_2$, whose sublevels are divided in energy by spin–spin interaction into a singlet state of spin projection $m_s = 0$ and a doublet $m_s = \pm 1$, separated by D = 2.87 GHz in the absence of a magnetic field, is a crucial characteristic of the NV center (**Figure 1b**). Here, m_s stands for the spin projection along the intrinsic quantization axis of the NV defect, which corresponds to the axis connecting the nitrogen and the vacancy ([111] crystal axis) [14]. The NV defect can be optically excited through spin-conserving transitions to a spin triplet ^3E excited state, which is an orbital doublet with a zero-field splitting D_{es} = 1.42 GHz at room temperature, exhibiting the same quantization axis and gyromagnetic ratio as in the ground level [15]. After optically excited in the ^3E level, the NV center can relax to ground level through two various transition routes, including the same radiative transition path producing a broadband red PL and another transition path involving non-radiative intersystem crossing (ISC) to singlet states (**Figure 1b**). Since non-radiative ISCs to the ^1E singlet state are highly spin-selective, whereas optical transitions are mostly spin-conserving ($m_s = 0$), the shelving rate from the $m_s = 0$ sublevel is substantially less than those from $m_s = \pm 1$. Furthermore, the NV defect prefers to decay from the lowest $^1A_1$ singlet state toward the ground state $m_s = 0$ sublevel [16, 17]. Consequently, these spin-selective processes use optical pumping

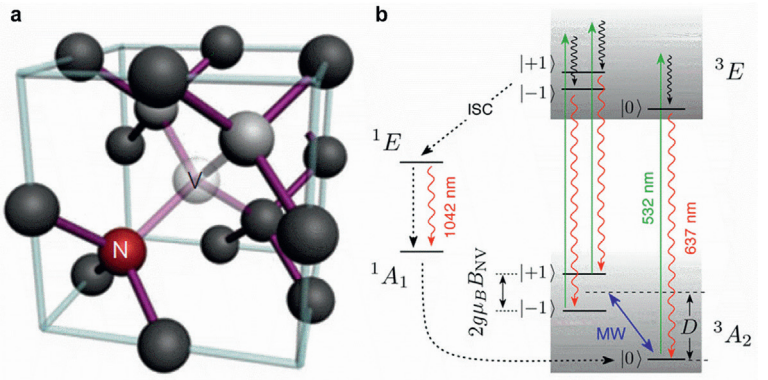

Figure 1.
(a) Atomic structure of the NV defect in diamond. (b) Schematic diagram of energy levels in NV defect. Spin conserving optical transitions from the $^3A_2$ spin triplet ground state to the ^3E excited state are shown with solid arrows. The dashed arrows indicate spin selective intersystem crossing (ISC) involving the singlet states ^1E and $^1A_1$. The infrared (IR) transition occurring at 1042 nm between the singlet states is also shown. Reproduced with permission from ref. [5]. Copyright 2014 IOP Publishing Ltd.

to achieve substantial electron spin polarization into $m_s = 0$. Moreover, due to the non-radiative ISCs, the PL intensity of the NV center will become higher when the state is $m_s = 0$ populated. Indeed, by providing a resonant microwave (MW) field, a single NV defect that was initially prepared in the $m_s = 0$ state by optical pumping can be driven to the $m_s = \pm 1$ spin state, leading to a decrease in the PL signal. This property has been widely applied recently in the context of diamond-based quantum information processing, where the NV defect is investigated as a solid-state spin qubit [18].

Neglecting the hyperfine interaction with nearby nuclear spins in the diamond lattice, the spin Hamiltonian of the level can be written as:

$$H = \left(hD + + d^{\parallel}E_z\right)\left[S_z^2 - \frac{S(S+1)}{3}\right] + g\mu_B \boldsymbol{B}\cdot\boldsymbol{S} - d^{\perp}\left[E_x\left(S_xS_y + S_yS_x\right) + E_y\left(S_x^2 - S_y^2\right)\right] \quad (1)$$

where z is the NV defect quantization axis, h is the Planck constant, d is the ground triplet state permanent electric dipole moment, E is the electric field, μ_B is the Bohr magneton, $g \approx 2.0$ is the electron g-factor, B is the applied magnetic field, S is the electron spin operator, and S_x, S_y, and S_z are the Pauli matrices [19]. The axial zero-field splitting parameter D is ~2.87 GHz resulting from spin–spin interaction between the two unpaired electrons of NV defect [5]. The measured axial ($d^{\parallel}/h$) and non-axial ($d^{\perp}/h$) components of the ground triplet-state permanent electric dipole moment are ~0.35 ± 0.02 and 17 ± 3 Hz cm V^{-1}, respectively [19]. In addition, the axial splitting parameter D is related to the temperature due to the combination effects of thermal expansion and electron–phonon interactions [20]. Therefore, the NV center in diamond offers unique possibilities to be employed as a nanoscale sensor for detection and imaging of magnetic fields, electric fields, and temperatures (**Figure 2**). For instance, the measurement principle for magnetometry applications of NV defect is comparable to that of optical magnetometers based on the precession of spin-polarized atomic gases [22].

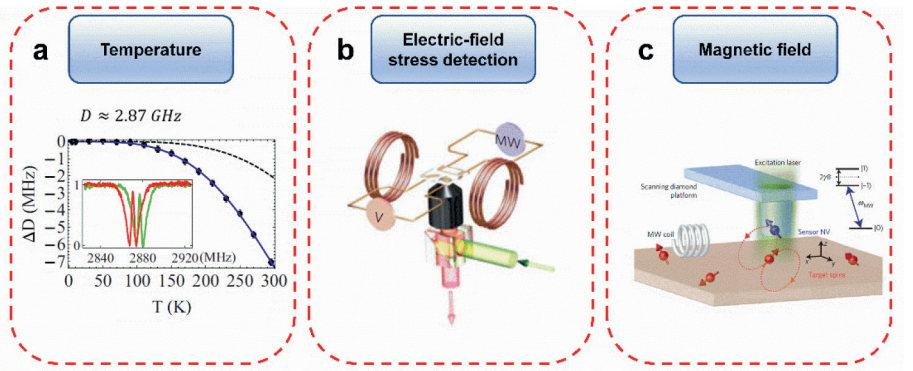

Figure 2.
The possible applications of NV defect in the detection or imaging of temperature, electric fields, and magnetic fields. (a) Reproduced with permission from ref. [20]. Copyright 2014 American Physical Society. (b) Reproduce with permission from ref. [19]. Copyright 2011 Nature Publishing Group. (c) Reproduced with permission from ref. [21]. Copyright 2013 Nature Publishing Group.

The applied magnetic field is evaluated through the observation of Zeeman shifts of the NV defect electron spin sublevels. In fact, the Zeeman effect occurs when a magnetic field is applied near the NV defect, lifting the degeneracy of $m_s = \pm 1$ spin sublevels and causing the emergence of two resonance lines in the ESR spectrum. Therefore, a single NV defect can act as a magnetic field sensor with an atomic-sized detecting volume [23, 24].

Additionally, the NV defect in diamond holds great promise for quantum communication applications, and its special structure enables spin states to be measured at room temperature [25]. Weakness of spin-orbit coupling and high Debye temperature of diamond ensure long spin–lattice relaxation time for NV-electron spins, [26, 27] making NV defect in diamond a promising candidate for quantum computing and quantum communication. After a single NV center in diamond absorbs a photon (532 nm), NV center will relax to emit a photon (637 nm). Subsequently, the emitted photon can be captured to optically readout the spin state. After a certain period of time, the NV center is reset, allowing the aforementioned processes to be repeated. Therefore, the controlled generation of single photons based on NV defect in diamond is significant for applications in quantum communication [28, 29]. Moreover, room-temperature quantum entanglement with the lifetime of milliseconds between two single NV defect spins in diamond can be realized for the future room-temperature quantum device [30].

3. Growth methods of diamond

There are two commonly used methods to grow diamond crystals, including high-pressure-high-temperature (HPHT) and chemical vapor deposition (CVD) methods. The phase diagram of carbon in **Figure 3** demonstrates that diamond is stable in the HPHT region. The HPHT methods are carried out under conditions that are in the diamond region of the phase diagram, while the CVD methods are conducted under circumstances corresponding to the graphite phase.

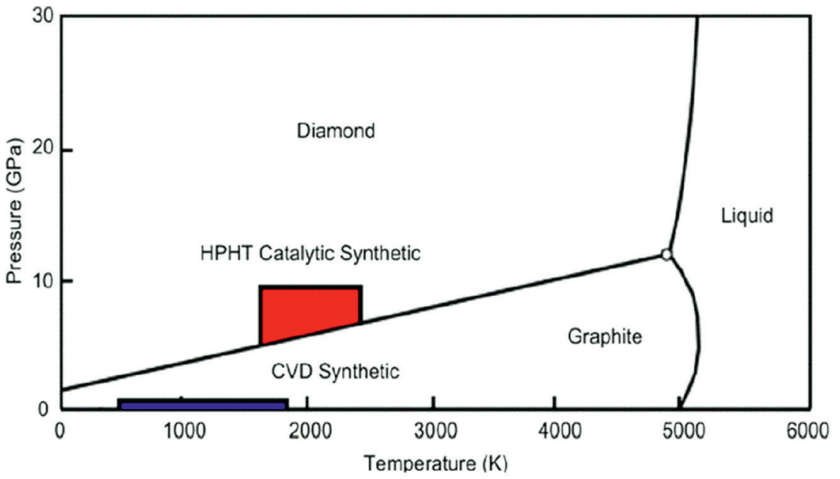

Figure 3.
Phase diagram for carbon revealing the pressure and temperature regions with HPHT and CVD synthesis can occur. It is notable that CVD is a nonequilibrium process. Reproduced with permission from ref. [31]. Copyright 2020 American Chemical Society.

3.1 HPHT

Nature is the source of theoretical reference for cultivating diamonds under high-temperature and high-pressure environments. In fact, by placing diamond seed crystals in a high-temperature and high-pressure environment that simulates the formation of natural diamonds, the carbon atoms are adsorbed from the carbon source onto the seed crystals to grow diamond single crystals [32, 33].

Since Strong and Wentorf from G.E. company successfully grew large diamond crystals by temperature-gradient approach in 1971, [34] the growth technology of gem-quality diamond has gradually become mature and commercialized. HPHT methods can be categorized into the solubility-gradient, temperature-gradient, no-catalyst conversion, and shock compression approaches. In fact, HPHT methods are widely used to grow diamond in industry. In the solubility-gradient approach, diamond powders can be prepared by solving graphite in a molten metal (Fe, Ni, or Co, etc.) under HPHT conditions [35]. However, it is difficult to prepare high-quality single-diamond crystals with dimensions greater than 1 mm by the solubility-gradient approach. The temperature-gradient approach to grow large diamond crystals is illustrated in **Figure 4**. First, the carbon source is usually placed at high temperature, and the crystal seed is placed at low temperature. The growth process of diamond single crystals is the dissolution and recrystallization of diamond. As the carbon concentration in the solvent metal catalyst depends on the temperature, there is a temperature difference (20–50°C) between the high-temperature and the low-temperature ends, which causes the carbon to diffuse from the high-temperature end to the low-temperature end and precipitate on the crystal seed, leading to the epitaxial growth of the diamond crystals [34, 36]. However, in the production process at high temperature and high pressure, a very critical step is to stimulate the carbon source such as graphite and other materials required for diamond growth to release free carbon atoms. Under normal conditions, this can only be achieved at a temperature of 2000°C and the pressure of several MPa, which is much more stringent than the natural diamond formation conditions in nature.

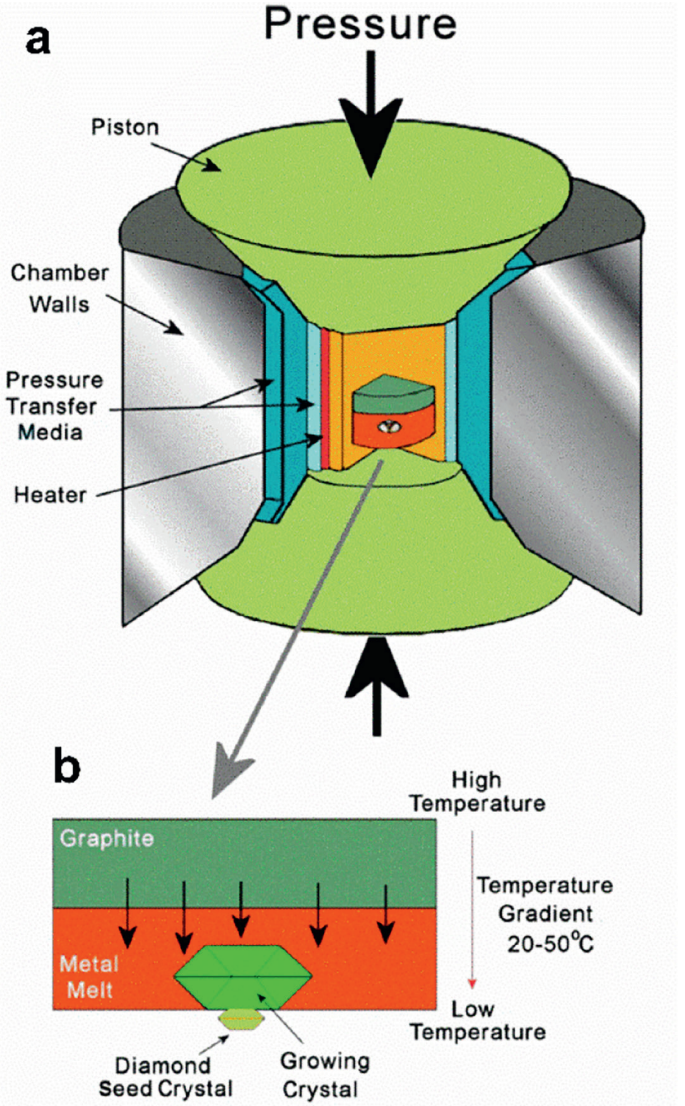

Figure 4.
Schematic diagram of (a) an HPHT press that applies high pressures and temperatures to a cell holding graphite, a metal melt, and a diamond seed crystal. These circumstances cause (b) the graphite to dissolve in the metal and precipitate on the seed crystal, therefore spreading the diamond lattice. Reproduced with permission from ref. [31]. Copyright 2020 American Chemical Society.

Therefore, to avoid the stringent conditions in HPHT method, metal catalysts are utilized in the synthesis of diamond, because the adding catalysts can efficiently reduce the phase transition activation energy of diamond, resulting in the decrease of the temperature from more than 2000°C to the actual 1200–1500°C. However, due to the utilization of metal catalysts in HPHT method, there will be a small amount of nearly undetectable metal impurities in the diamond, which make the diamond possess some unique physical properties, such as a certain weak magnetism.

3.2 CVD

Chemical vapor deposition (CVD) for diamond growth generally needs the use of plasma, which can be generated by various plasma sources, including microwave, DC, or RF plasma. The gas source containing methane (CH_4) gas diluted with H_2 gas can be transformed to CH_3 and H radicals for the diamond growth.

Figure 5a shows the principle of CVD diamond growth method [31]. The microwave or DC heating can lead to the generation of H and CH_3 radicals. H radicals play an important role in the CVD process. The roles of H radicals are as follows: (1) the H radicals can etch the graphite phase on the diamond surface to let diamond continuously grow; (2) the H radicals can terminate with dangling bonds on the diamond surface to maintain the sp^3 hybridization of the surface carbon atoms; (3) the H radicals can react with CH_4 molecules to produce CH_3 radicals; and (4) the H radicals can react with diamond surface H to activate the surface bond. The current realization of the reaction mechanism for CVD diamond growth [38] shown in **Figure 5b** illustrates that two carbon atoms for a dimer structure with H-terminated bonds on the diamond surface first. After one of surface H atoms reacts with an H radical to desorb to produce the surface dangling bond, a CH_3 radical from the vapor phase will adsorb on the reactive dangling bond to form a bond with the surface C atom. Then the H radical of CH_3 radical desorbs and breaks the dimer bond. Finally, the CH_2 radical forms the bond with the other surface C atom.

The preparation of diamond by hot filament (DC-plasma) CVD is one of the most widely used methods at present (**Figure 6**). It has the characteristics of simple preparation process, cheap equipment, and mature technology. In the production process of diamond, there are many parameters that affect the quality of diamond film, including filament type, methane concentration (CH_4/H_2 ratio), substrate temperature, distance between substrate and filament, nitrogen pollution, carbon source selection, etc. One of the important influencing factors is the C:H ratio, which can influence the concentration of activated CH_3 and H radicals. As shown in the scanning electron microscopy (SEM) images as shown in **Figure 7**, with the increase of methane concentration in a certain range, the grain size and surface roughness of diamond decreased, and cauliflower-like particles appeared on the surface.

The microwave plasma CVD (MPCVD) method is similar to the hot filament CVD (HFCVD) method, in which the gas molecules are transformed into active

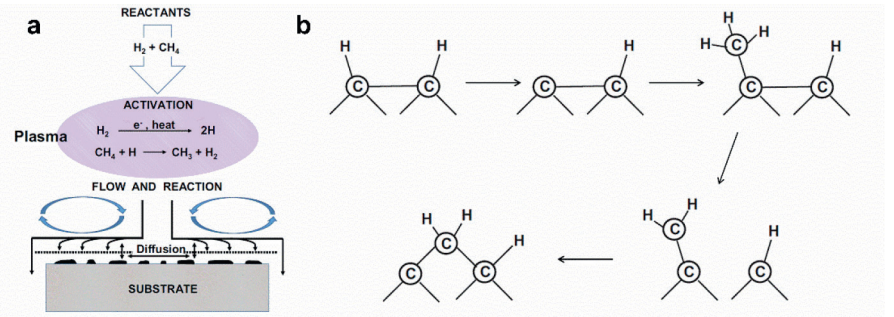

Figure 5.
(a) Principle of plasma CVD diamond growth, and (b) the mechanism of surface chemical reaction of CVD diamond growth. Reproduced with permission from ref. [37]. Copyright 2016 Elsevier Ltd.

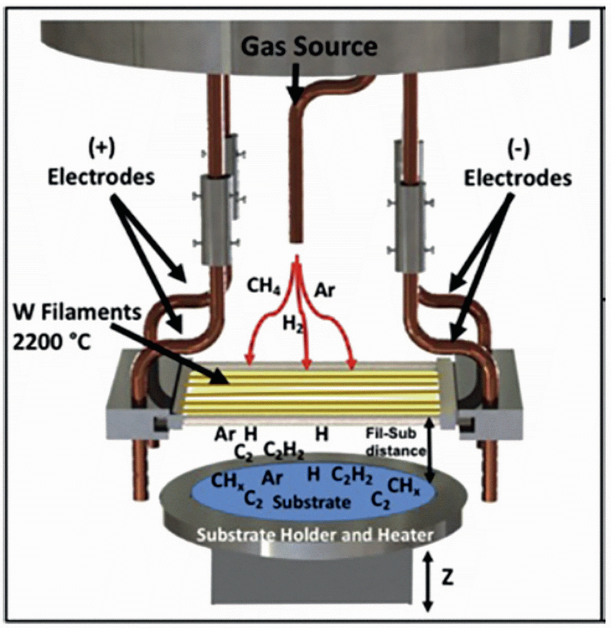

Figure 6.
Setup of polycrystalline diamond growth by hot filament CVD (HFCVD). Reproduced with permission from ref. [39]. Copyright 2017 Microscopy Society of America.

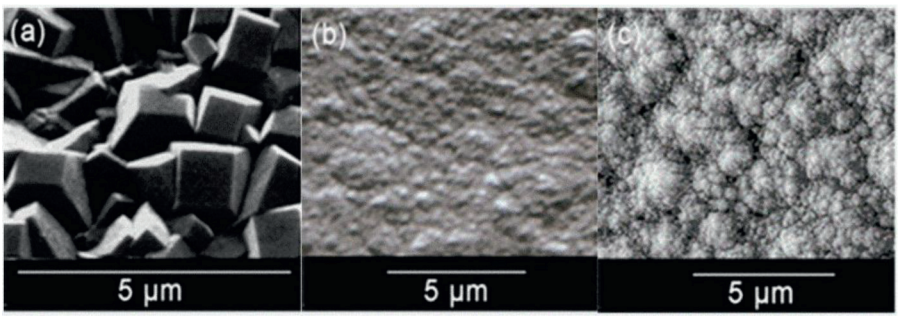

Figure 7.
(a–c) Examples of different morphologies of undoped polycrystalline CVD diamond films grown using different C:H ratios in the source gas: (a) faceted microcrystalline diamond typically grown under standard deposition conditions, with <2% CH_4 in H_2, (b) smoother nanocrystalline diamond grown as before, but with >4% CH_4 in H_2, and (c) "cauliflower" nanocrystalline diamond grown with >4% CH_4 in H_2. Reproduced with permission from ref. [31]. Copyright 2020 American Chemical Society.

carbon-containing groups and H atoms by injecting energy. The plasma density of MPCVD is higher than that of HFCVD so that high-purity diamond can be prepared. Due to the limitation of microwave wavelength and microwave resonator, a large-area uniform film cannot be obtained. Therefore, MPCVD is not suitable for industrial production. In order to further improve the quality and growth rate of diamond, the improvement and innovation of microwave cavity have become the focus of research. The stability of microwave frequency and the singleness of microwave energy will still be the direction that needs to be overcome in the future. With the development of GaN devices, the third-generation semiconductor solid-state microwave source

will possibly replace the magnetron and become an inevitable choice for the modularization and miniaturization of high-power and high-stability microwave sources. In addition, the addition of multi-beam energy coupling excitation plasma such as radio frequency, laser, and other energy will also open a new platform for MPCVD equipment.

Despite the polycrystalline diamond grown by CVD techniques, the growth of ultrathin diamond film has also attracted extensive attention. In the past years, theoretical calculations based on density functional studies have predicted the chemically induced transformation of multilayer graphene into a diamond-like film [40, 41]. Recently, in experiment, the fluorination of graphene sheets in Bernal-stacked bilayer graphene generated by CVD over a single-crystal CuNi(111) surface can cause the creation of interlayer carbon–carbon bonds, resulting in a fluorinated diamond monolayer [42].

4. Creation methods of NV defect in diamond

The development of diamond NV centers has been relatively mature so far. Not only can NV centers be formed during diamond growth (inter-growth methods), but also ions, electrons, and laser beams can be used to obtain holes after diamond growth and then combine with nitrogen atoms to form NV centers (post-growth methods).

4.1 Inter-growth methods

The formation of NV centers in diamond can be realized during the growth of diamond by CVD (inter-growth). By adding a nitrogen gas source in the mixed gas source, the NV centers can possibly be created during the diamond growth. There are several advantages to grow NV defect by inter-growth method: (1) by adjusting the gas-phase environment and growth conditions, the NV defect concentration of the diamond film can be controlled within 200 ppb, ideally suitable for optical and electronic applications; [43] (2) The NV centers by this method can not only achieve a high concentration, but also the lifetime of electron spin coherence in ground state can reach the order of milliseconds. However, the inter-growth method by CVD to create NV defect has obvious drawbacks, like the uncontrollable formation site of NV defect, which needs further investigations. By optimizing the nitrogen concentration in the range of 0.2–20 ppm and E-beam irradiation conditions to study the formation of NV defect in CVD-grown diamond, the spin–spin coherence times of 45.5–549 μs for CVD diamond containing 168–1 ppb NV centers can be achieved [44]. In addition, with low growth temperature to enhance the nitrogen incorporation and with N_2O as a dopant gas for diamond growth by CVD on [113]-oriented substrate, the obtained nitrogen-doped diamond combines a high NV defect creation yield and long coherence time of several tens of μs together with a partial preferential orientation, which are desirable requirements for diamond-based sensors (**Figure 8**) [45].

4.2 Post-growth methods

4.2.1 Ion implantation method

The NV centers can be generated by nitrogen ion implantation after the formation of diamond film. Nitrogen ion implantation provides an NV positioning accuracy that

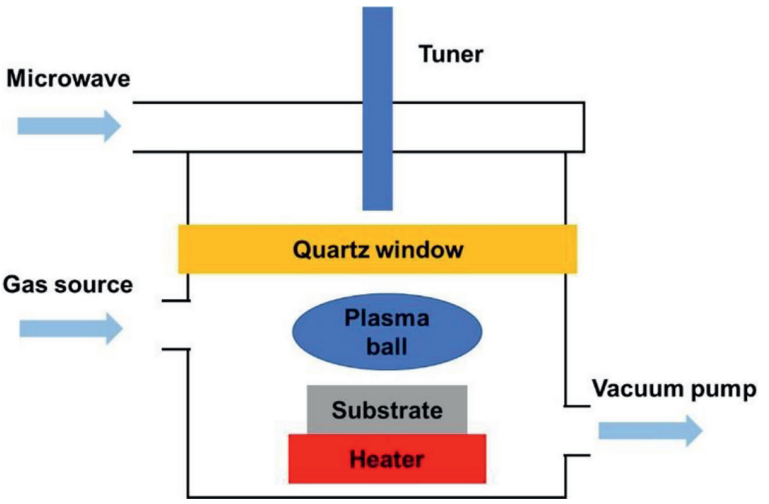

Figure 8.
Schematic illustration for the creation of NV defect in diamond by CVD.

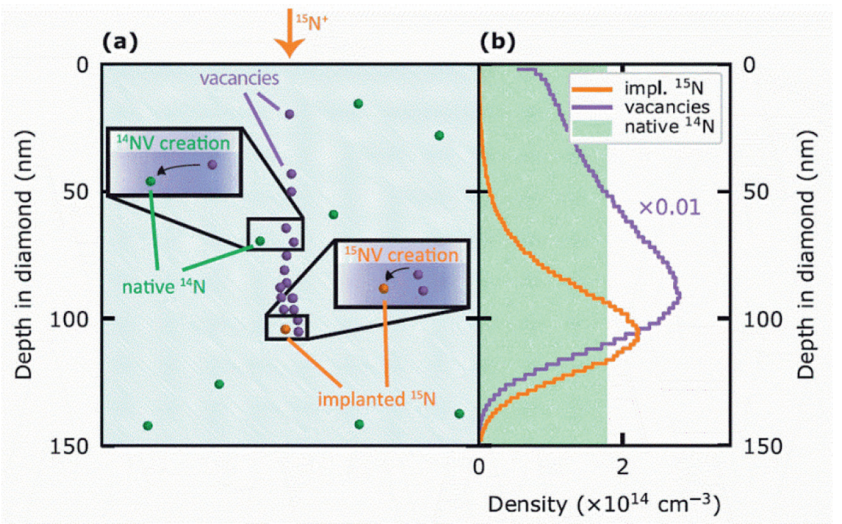

Figure 9.
The creation of NV defect via nitrogen ion implantation. (a) Schematic illustration of implanted $^{15}N^+$ leaving a trail of vacancies until settling into a final position. Vacancies mobilized by annealing can bind a nitrogen atom (implanted or native) to form an NV defect, and (b) a SRIM simulation using the parameters in sample shows the distribution of implanted nitrogen and created vacancies. Reproduced with permission from ref. [47]. Copyright 2019 American Physical Society.

enables the integration with on-chip photonic devices [46]. Furthermore, this method can create a single NV center or a new NV defect coupling with the nearby NV defect. However, in the process of bombarding diamond with nitrogen ions, severe lattice damage in diamond is inevitable, resulting in damaging the ground state of NV defect and weakening the spin coherence time. Fortunately, it has been found that high-temperature annealing can recover part of the damaged lattice. In order to distinguish NV defects formed by implanted nitrogen atoms from the NV defects formed by

native ^{14}N atoms, ^{15}N isotope atoms were used to create NV defect by ion implantation and annealing procedure (**Figure 9**) [47, 48]. It is observed that NV centers formed by implanted 15 N atoms exhibit broadened optical linewidth (>1 GHz) and higher strain than that formed by native ^{14}N atoms (<500 MHz). The poor optical coherence of NV centers formed from implanted nitrogen is not resulted from an intrinsic effect related to the diamond or isotope, but the influence of lattice damage by ion bombardment [47]. Meanwhile, a mass-produced NV color center array with positioning accuracy of tens of nanometers can be achieved by using nitrogen ion implantation [49].

4.2.2 Femtosecond laser irradiation method

The femtosecond laser irradiation used to generate NV defects can cause strong damage to diamond, even more leading to graphitization. In 2017, Chen et al. used a single-pulse laser writing to controllably generate NV centers on the diamond surface without the occurrence of macroscopic crystal graphitization, which promoted the development of femtosecond laser irradiation for NV defect generation [50].

The principle of the femtosecond laser method shown in **Figure 10a** is that electron beam, generated by ionizing the air due to the strong electric field formed by the propagation of the femtosecond laser, can lead to the generation of vacancies in diamond. After annealing process, the produced vacancies can combine with nitrogen atoms to form NV defects [53]. Compared with ion implantation, the NV defect generated by femtosecond laser irradiation method possesses a narrower optical linewidth and a longer decoherence time. The NV color centers in diamond exhibit a narrow optical linewidth of 13.05 ± 0.2 MHz and a long decoherence time of 445 ± 27.6 μs [51].

4.2.3 Electron beam irradiation method

The principle of electron beam irradiation technique is to use electron beam to irradiate diamond to generate vacancies, which can bind with nitrogen atoms to form NV defects after high-temperature annealing, as shown in **Figure 10b**. The concentration and depth of the generated NV defects can be controlled by adjusting the energy

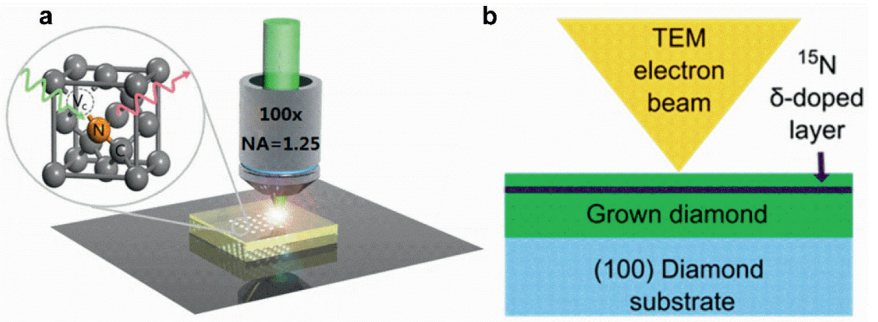

Figure 10.
(a) Schematic of the preparation of NV defect in diamond using femtosecond laser irradiation. Reproduced with permission from ref. [51]. Copyright 2022 AIP Publishing, and (b) Schematic of the generation of NV defect in diamond by electron beam irradiation in a transmission electron microscope (TEM). Reproduced with permission from ref. [52]. Copyright 2016 American Chemical Society.

of electron beam, the irradiation time, and the distance between the diamond and the electron beam gun. In 2017, a TEM-based method was used to create localized NV defect with coherence time exceeding 1 ms [52].

Due to the high sensitivity and high spatial resolution of TEM-based technique, it is well suited for the creation of NV defects. By using electron beam irradiation with the energy of 200 keV followed by high-temperature annealing at 1200°C, a surface density of ~2500 μm^{-2} of NV defects in diamond can be achieved. This technique can enable the given arbitrary in-depth control of NV centers.

5. Conclusions

In this chapter, we have summarized the potential applications of NV defect in diamond, including sensors for the detection of temperature, electric and magnetic fields as well as quantum communication and computing. Furthermore, the growth methods of diamond are introduced, such as HPHT and CVD methods. For the creation of NV defects in diamond, NV centers can be generated during the grow of diamond by adding nitrogen gas source in the mixed gas source. Additionally, NV defects can also be obtained after diamond growth, notably ion implantation, femtosecond laser irradiation, and electron beam irradiation methods.

Acknowledgements

This work is financially supported from the Start-up Foundation of Henan University (Grant No.: CX3050A0970531).

Conflict of interest

The authors declare no conflict of interest.

Appendices and nomenclature

NV	nitrogen vacancy
HPHT	high-pressure high temperature
CVD	chemical vapor deposition
ISC	intersystem crossing
PL	photoluminescence
MPCVD	microwave plasma CVD
HFCVD	hot filament CVD

DOI: http://dx.doi.org/10.5772/.108159

References

[1] Ismagilov R, Malykhin S, Puzyr A, Loginov A, Kleshch V, Obraztsov A. Single-crystal diamond needle fabrication using hot-filament chemical vapor deposition. Materials. 2021;**14**:2320

[2] Mochalin V, Shenderova O, Ho D, Gogotsi Y. The properties and applications of nanodiamonds. In: Balogh LP, editor. Nano-Enabled Medical Applications. 1st ed. New York: Taylor & Francis; 2020. pp. 313-350. DOI: 10.1201/9780429399039.ch11

[3] Dyer H, Raal F, Du Preez L, Loubser J. Optical absorption features associated with paramagnetic nitrogen in diamond. Philosophical Magazine. 1965;**11**:763

[4] Siyushev P, Nesladek M, Bourgeois E, Gulka M, Hruby J, Yamamoto T, et al. Photoelectrical imaging and coherent spin-state readout of single nitrogen-vacancy centers in diamond. Science. 2019;**363**:728

[5] Rondin L, Tetienne J-P, Hingant T, Roch J-F, Maletinsky P, Jacques V. Magnetometry with nitrogen-vacancy defects in diamond. Reports on Progress in Physics. 2014;**77**:056503

[6] Balasubramanian G, Neumann P, Twitchen D, Markham M, Kolesov R, Mizuochi N, et al. Ultralong spin coherence time in isotopically engineered diamond. Nature Materials. 2009;**8**:383

[7] Mita Y. Change of absorption spectra in type-Ib diamond with heavy neutron irradiation. Physical Review B. 1996;**53**:11360

[8] Gaebel T, Domhan M, Wittmann C, Popa I, Jelezko F, Rabeau J, et al. Photochromism in single nitrogen-vacancy defect in diamond. Applied Physics B. 2006;**82**:243

[9] Davies G, Hamer M. Optical studies of the 1.945 eV vibronic band in diamond. Proceedings of the Royal Society of London. A. Mathematical and Physical Sciences. 1976;**348**:285

[10] Gruber A, Drabenstedt A, Tietz C, Fleury L, Wrachtrup J. Scanning confocal optical microscopy and magnetic resonance on single defect centers. Science. 2012;**2012**:276

[11] Faklaris O, Joshi V, Irinopoulou T, Tauc P, Sennour M, Girard H, et al. Photoluminescent diamond nanoparticles for cell labeling: Study of the uptake mechanism in mammalian cells. ACS Nano. 2009;**3**:3955

[12] Mohan N, Chen C-S, Hsieh H-H, Wu Y-C, Chang H-C. In vivo imaging and toxicity assessments of fluorescent nanodiamonds in Caenorhabditis elegans. Nano Letters. 2010;**10**:3692

[13] Wu T-J, Tzeng Y-K, Chang W-W, Cheng C-A, Kuo Y, Chien C-H, et al. Tracking the engraftment and regenerative capabilities of transplanted lung stem cells using fluorescent nanodiamonds. Nature Nanotechnology. 2013;**8**:682

[14] Loubser JH, Van Wyk J. Optical Spin-polarisation in a Triplet State in Irradiated and Annealed Type 1b Diamonds. United Kingdom: DIN-Mitt; 1977

[15] Fuchs G, Dobrovitski V, Hanson R, Batra A, Weis C, Schenkel T, et al. Excited-state spectroscopy using single spin manipulation in diamond. Physical Review Letters. 2008;**101**:117601

[16] Robledo L, Bernien H, Van Der Sar T, Hanson R. Spin dynamics in the optical

cycle of single nitrogen-vacancy centres in diamond. New Journal of Physics. 2011;**13**:025013

[17] Tetienne J, Rondin L, Spinicelli P, Chipaux M, Debuisschert T, Roch J, et al. Magnetic-field-dependent photodynamics of single NV defects in diamond: An application to qualitative all-optical magnetic imaging. New Journal of Physics. 2012;**14**:103033

[18] Childress L, Hanson R. Diamond NV centers for quantum computing and quantum networks. MRS Bulletin. 2013;**38**:134

[19] Dolde F, Fedder H, Doherty MW, Nöbauer T, Rempp F, Balasubramanian G, et al. Electric-field sensing using single diamond spins. Nature Physics. 2011;**7**:459

[20] Doherty MW, Acosta VM, Jarmola A, Barson MS, Manson NB, Budker D, et al. Temperature shifts of the resonances of the NV− center in diamond. Physical Review B. 2014;**90**:041201

[21] Grinolds MS, Hong S, Maletinsky P, Luan L, Lukin MD, Walsworth RL, et al. Nanoscale magnetic imaging of a single electron spin under ambient conditions. Nature Physics. 2013;**9**:215

[22] Budker D, Romalis M. Optical magnetometry. Nature Physics. 2007;**3**:227

[23] Taylor JM, Cappellaro P, Childress L, Jiang L, Budker D, Hemmer P, et al. High-sensitivity diamond magnetometer with nanoscale resolution. Nature Physics. 2008;**4**:810

[24] Degen C. Scanning magnetic field microscope with a diamond single-spin sensor. Applied Physics Letters. 2008;**92**:243111

[25] Childress L, Gurudev Dutt M, Taylor J, Zibrov A, Jelezko F, Wrachtrup J, et al. Coherent dynamics of coupled electron and nuclear spin qubits in diamond. Science. 2006;**314**:281

[26] Astner T, Gugler J, Angerer A, Wald S, Putz S, Mauser NJ, et al. Solid-state electron spin lifetime limited by phononic vacuum modes. Nature Materials. 2018;**17**:313

[27] Jarmola A, Acosta V, Jensen K, Chemerisov S, Budker D. Temperature- and magnetic-field-dependent longitudinal spin relaxation in nitrogen-vacancy ensembles in diamond. Physical Review Letters. 2012;**108**:197601

[28] Kurtsiefer C, Mayer S, Zarda P, Weinfurter H. Stable solid-state source of single photons. Physical Review Letters. 2000;**85**:290

[29] Prawer S, Greentree AD. Diamond for quantum computing. Science. 2008;**320**:1601

[30] Dolde F, Jakobi I, Naydenov B, Zhao N, Pezzagna S, Trautmann C, et al. Room-temperature entanglement between single defect spins in diamond. Nature Physics. 2013;**9**:139

[31] Ashfold MN, Goss JP, Green BL, May PW, Newton ME, Peaker CV. Nitrogen in diamond. Chemical Reviews. 2020;**120**:5745

[32] Kanda H, Akaishi M, Yamaoka S. New catalysts for diamond growth under high pressure and high temperature. Applied Physics Letters. 1994;**65**:784

[33] Liu X, Jia X, Guo X, Zhang Z, Ma HA. Experimental evidence for nucleation and growth mechanism of diamond by seed-assisted method at high pressure and high temperature. Crystal Growth & Design. 2010;**10**:2895

[34] Strong H, Wentorf R. The growth of large diamond crystals. Naturwissenschaften. 1972;**59**:1

[35] Bovenkerk H, Bundy F, Hall H, Strong H, Wentorf R. Preparation of diamond. Nature. 1959;**184**:1094

[36] Sumiya H, Satoh S. High-pressure synthesis of high-purity diamond crystal. Diamond and Related Materials. 1996;**5**:1359

[37] Kasu M. Diamond epitaxy: Basics and applications. Progress in Crystal Growth and Characterization of Materials. 2016;**62**:317

[38] Garrison BJ, Dawnkaski EJ, Srivastava D, Brenner DW. Molecular dynamics simulations of dimer opening on a diamond {001}(2x1) surface. Science. 1992;**255**:835

[39] Arellano-Jimenez M, Alcantar-Peña J, Aguilar JO, Yacaman M, Auciello O. Polycrystalline diamond films produced by hot-filament chemical vapor deposition. Microscopy and Microanalysis. 2017;**23**:2272

[40] Barboza AP, Guimaraes MH, Massote DV, Campos LC, Barbosa Neto NM, Cancado LG, et al. Room-temperature compression-induced diamondization of few-layer graphene. Advanced Materials. 2011;**23**:3014

[41] Kvashnin AG, Chernozatonskii LA, Yakobson BI, Sorokin PB. Phase diagram of quasi-two-dimensional carbon, from graphene to diamond. Nano Letters. 2014;**14**:676

[42] Bakharev PV, Huang M, Saxena M, Lee SW, Joo SH, Park SO, et al. Chemically induced transformation of chemical vapour deposition grown bilayer graphene into fluorinated single-layer diamond. Nature Nanotechnology. 2020;**15**:59

[43] Tallaire A, Collins A, Charles D, Achard J, Sussmann R, Gicquel A, et al. Characterisation of high-quality thick single-crystal diamond grown by CVD with a low nitrogen addition. Diamond and Related Materials. 2006;**15**:1700

[44] Luo T, Lindner L, Langer J, Cimalla V, Vidal X, Hahl F, et al. Creation of nitrogen-vacancy centers in chemical vapor deposition diamond for sensing applications. New Journal of Physics. 2022;**24**:033030

[45] Balasubramanian P, Osterkamp C, Brinza O, Rollo M, Robert-Philip I, Goldner P, et al. Enhancement of the creation yield of NV ensembles in a chemically vapour deposited diamond. Carbon. 2022;**194**:282

[46] Schröder T, Mouradian SL, Zheng J, Trusheim ME, Walsh M, Chen EH, et al. Quantum nanophotonics in diamond. JOSA B. 2016;**33**:B65

[47] van Dam SB, Walsh M, Degen MJ, Bersin E, Mouradian SL, Galiullin A, et al. Optical coherence of diamond nitrogen-vacancy centers formed by ion implantation and annealing. Physical Review B. 2019;**99**:161203

[48] Chu Y, de Leon NP, Shields BJ, Hausmann B, Evans R, Togan E, et al. Coherent optical transitions in implanted nitrogen vacancy centers. Nano Letters. 2014;**14**:1982

[49] Feng F, Wang J, Zhang W, Zhang J, Lou L, Zhu W, et al. Efficient generation of nanoscale arrays of nitrogen-vacancy centers with long coherence time in diamond. Applied Physics A. 2016;**122**:1

[50] Chen Y-C, Salter PS, Knauer S, Weng L, Frangeskou AC, Stephen CJ, et al. Laser writing of coherent colour centres in diamond. Nature Photonics. 2017;**11**:77

[51] Gao S, Yin S-Y, Liu Z-X, Zhang Z-D, Tian Z-N, Chen Q-D, et al.

Narrow-linewidth diamond single-photon sources prepared via femtosecond laser. Applied Physics Letters. 2022;**120**:023104

[52] McLellan CA, Myers BA, Kraemer S, Ohno K, Awschalom DD, Bleszynski Jayich AC. Patterned formation of highly coherent nitrogen-vacancy centers using a focused electron irradiation technique. Nano Letters. 2016;**16**:2450

[53] Gao S, Duan Y-Z, Tian Z-N, Zhang Y-L, Chen Q-D, Gao B-R, et al. Laser-induced color centers in crystals. Optics & Laser Technology. 2022;**146**:107527

Chapter 6

Ab Initio Study of the Electronic and Energy Properties of Diamond Carbon

Abdellah Sellam, Abdelaziz Koumina, Abderrahim Bakak, Abdellah Hadaoui, El Kebir Hlil and Rodolphe Heyd

Abstract

In this chapter, we present a study on the electronic properties of diamond carbon, using band structure and density of states calculations. The calculations are based on the use of the grid-based projector-augmented wave (GPAW) and atomic simulation environment (ASE) methods. The main results of our work are the optimization of diamond energy (to −17.57 eV) and the calculation of the gap with the PBE (Perdew, Burke, and Ernzerhof) and the functional hybrid PBE0 hybrid functional, which is about 5.368 eV (the closest value to the value found in the literature). We were also able to reproduce the experimental value of the lattice constant of diamond to within 0.2% for PBE0 and 0.4% for PBE. Our results contribute to the study of the electronic properties of diamond using GPAW and ASE simulation, which is a set of Python modules, designed to facilitate the setup, execution, and analysis of atomic/electronic calculations. This tight integration of ASE and GPAW should be exploited in future research of the electronic properties of diamond, which is one of the most promising materials for the integrated electronic and photonic, radio, optoelectronic, and quantum devices industry. This chapter provides interesting information for the theoretical and experimental communities working in this field.

Keywords: diamond, density of state, band structure, grid-based projector-augmented wave (GPAW), atomic simulation environment (ASE), PBE

1. Introduction

Carbon is a unique element that appears in many different configurations of electronic states [1]. Materials such as graphite, graphene, carbon nanotubes, and diamond have basically the same chemical composition but a different crystal structure. This is called allotropy of carbon (see **Figure 1** [2, 3]). Carbon has six electrons occupying the $1s^2$, $2s^2$, and $2p^2$ orbitals. The $1s^2$ electrons are two strongly bound core electrons, while the $2s^2$ and $2p^2$ electrons are weakly bound valence electrons. The valence electrons give rise to the 2s, $2p_x$, $2p_y$, and $2p_z$ orbitals in the crystal phase. These orbitals are important for the formation of covalent bonds in carbon materials. Since the energy difference between the upper 2p and lower 2s orbitals is relatively small compared to other group 4

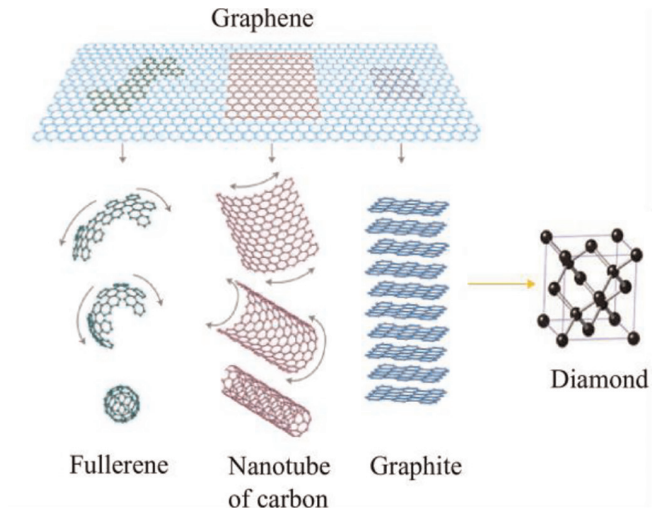

Figure 1.
Different allotropic forms of carbon [2, 3].

elements such as silicon (Si), the electron wave functions can easily mix with each other, which is called hybridization [4]. In sp^n hybridization, the (n + 1) bonds are responsible for the local structure. Thus, in sp. hybridization, a one-dimensional chain structure is formed, which is called carbyne. Carbyne [5] is a chain of carbon atoms held together by alternating double or single and triple atomic bonds. This makes it a true zero-dimensional material, unlike graphene atomic sheets that have a top and bottom, or hollow nanotubes that have an inside and outside. According to calculations by Liu et al., carbyne has twice the tensile stiffness of graphene and carbon nanotubes and nearly three times that of diamond.

An sp^2 hybridization forms a two-dimensional planar structure called graphene. In sp^3 hybridization, a regular three-dimensional tetrahedral structure is formed, which is known as diamond.

In graphite, in addition to the three in-plane bonds, out-of-plane π orbitals are formed with highly delocalized electrons that contribute primarily to electrical and thermal conductivity. The interaction of the free π electrons with light makes graphite appear black. In addition, the weak van der Waals interaction between the graphite sheets makes the graphite flexible and cleavable, as the graphene sheets can easily move relative to each other. A carbon nanotube can be viewed as a rolled-up graphite sheet and thus a one-dimensional structure. The bonds in the nanotubes are essentially of the sp^2 type. However, the circular curvature causes quantum confinement and $\sigma - \pi$ hybridization in which the three σ bonds are slightly out of plane. In this part, we are interested in the study of diamond.

Diamond has a crystal structure consisting of a face-centered cubic lattice of which one tetrahedral site out of two is occupied by a carbon atom, as represented in **Figure 2** [6].

The elementary lattice cell of diamond has carbon atoms, and its parameter is 3.57 Å. The shortest distance between two carbon atoms, that is, the distance corresponding to the quarter of the diagonal of the mesh is 1.54 Å, which makes the crystal lattice of diamond very dense (1.76×1023 atoms cm^{-3}) in comparison with other materials. The compactness of its structure, associated with the high energies of the carbon-carbon bonds ($E_{(C\text{-}C)}$ = 360 kJ mol^{-1}), is at the origin of diamond mechanical properties, which are well known (see **Table 1**) [6].

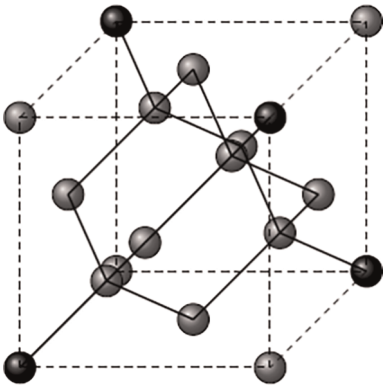

Figure 2.
Elementary crystal lattice cell of diamond [6].

Property	Unit	Silicon	Diamond
Density	$g\ cm^{-3}$	2.33	3.52
Melting point	K	1687	3773
Hardness	GPa	8.5	57–101
Coefficient of thermal expansion	K^{-1}	2.6×10^{-6}	1.0×10^{-6}
Young's modulus	GPa	130–180	1050–1200
Thermal conductivity	$W\ m^{-1}\ K^{-1}$	148	2500
Prohibited bandwidth GAP	eV	1.12	5.45
Electron mobility	$cm^2\ V^{-1}\ s^{-1}$	1350	4500

Table 1.
Some physical properties of diamond compared to silicon.

Its high hardness, estimated at 7000 kg mm^{-2} (Knoop hardness) [6], makes diamond the most resistant material. This characteristic allows it to be used in many mechanical applications such as cutting, drilling, or polishing. Its very high Young's modulus makes it advantageous for applications involving microelectromechanical system oscillators (MEMS)-type resonators [6]. In addition to its high thermal conductivity [7], which is five times greater than that of copper, diamond is used as a heat sink for electronic or optoelectronic components such as power transistors and laser diodes. More recently, it has been used for the realization of optical windows for high-power lasers or X-ray tubes; it is the combination of its optical, mechanical, and thermal properties, which is decisive [6].

Diamond is a three-dimensional crystalline material. Because of its structure, it is considered one of the most promising materials for the integrated electronic and photonic, radio, optoelectronic, and quantum device industry.

Following our publications on the electronic and magnetic structures of graphite using the Korringa-Kohn Rostoker (KKR) method [8] and on the electronic properties of the adsorption of CO and N_2 molecules on graphene and on a graphite plate using

GPAW and ASE [7], we decided to set up a simulation system based on GPAW and ASE to study the electrical and energetic properties of diamond. The main results of our work are the optimization of diamond energy, as well as the calculation of the density of state and the band structure.

2. Calculation methods

In this chapter, we present a real-space implementation of the PAW method in the open-source software package GPAW [9]. Note that there are several software packages that currently implement the PAW method using a plane-wave basis [10–12]. The PAW method [13, 14] is formally an all-electron method that provides an exact transformation between smooth pseudo wave functions and all-electron wave functions. While in practice the PAW method resembles pseudo potential methods, it remedies several shortcomings of conservative norm or ultra-smooth pseudopotentials.

The GPAW code is built on top of the ASE [3], which is a set of Python modules designed to facilitate the setup, execution, and analysis of atomistic/electronic calculations. This tight integration of ASE and GPAW should be maintained in the future. Interest in ASE has grown considerably over the past few years, to the point where ASE now supports about 12 different force and energy calculators.

There are of course several other open-source projects focused on DFT and time-dependent (TDDFT), such as abinit, quantum espresso and KKR [15], and Octopus. How does GPAW fit into this code market? The main feature that distinguishes GPAW from its competitors is the combination of a real-space description with the PAW method. The PAW method allows an accurate description of essentially all electrons in the frozen core, leading to smooth pseudo wave functions even for transition metals. The real-space description allows for easy and highly scalable parallelization due to the real-space decomposition, which allows for accurate calculations even for large systems.

Among the features currently implemented in GPAW, we can mention the calculation of static response functions using density-functional perturbation theory and the more general calculations of dynamic response functions in TDDFT. Force calculations as well as adiabatic and Ehrenfest dynamics are also implemented in TDDFT. In addition, work is underway to expand the number of atomic configurations to include all elements up to atomic number 86 [16].

In this work, we present density of states and band structure calculations of diamond using the PAW method as implemented in the GPAW package (https://wiki.fysik.dtu.dk/gpaw).

Traditionally [17], software packages for this type of simulation have been implemented in compiled languages, where Fortran in its various iterations has been the most popular choice. Although interpreted dynamic languages, such as Python, can increase the efficiency of the programmer, they cannot directly compete with the raw performance of compiled languages.

However, by using an interpreted language along with a compiled language, it is possible to benefit from most of the productivity-enhancing features while still achieving good numerical performance. This approach has been implemented in the GPAW electronic structure simulation software, using a combination of Python and C programming languages.

3. Results and discussions

3.1 Optimization of the diamond structure

The diamond unit cell contains two carbon atoms located at (0.0, 0.0, 0.0) and (0.25 a, 0.25 a, 0.25 a). After optimization, the CC bond length was found to be 1.55 Å. Relaxation of all model systems was performed using an 8 × 8 × 8 Monkhorst-Pack grid sampling, used during Brillouin zone integrations (512 k-points in the irreducible part of the Brillouin zone). **Tables 2** and **3** shows the results of the diamond structure optimization.

Other results provided by GPAW:
C-setup:
Name: Carbon.
Z: 6.
Valence: 4.
Core: 2.
Charge: 0.0.
Cutoffs: 0.64(comp), 1.14(filt), 1.14(core), lmax = 2.

3.2 Electronic band structure of diamond

Figure 3 shows the electronic band structure of diamond, whose unit cell is composed of two carbon atoms, located at the positions shown in Section 3.1. The band structure is plotted along the high-symmetry line ΓXWKL of the Brillouin zone. The x-axis represents the kpts = {'path' = 'ΓXWKL', 'npoints' = 60}, with 16 bands,

Diamond energy	−17.57 eV
Diamond atomization energy	−17.57 eV
Experimental bond length (GPAW and ASE):	
Diamond energy	−17.57 eV
Bond length	1.55 Å
PBE energy minimum	
Diamond energy	−17.57 eV
Bond length	1.55 Å

Table 2.
Optimization of the diamond structure.

Valence states	Energy (eV)	Radius (Å)
2s (2.00)	−13.751	0.635
2p (2.00)	−5.284	0.635
*s	13.461	0.635
*p	21.927	0.635
*d	0.000	0.635

Table 3.
Valence states, energy, and radius.

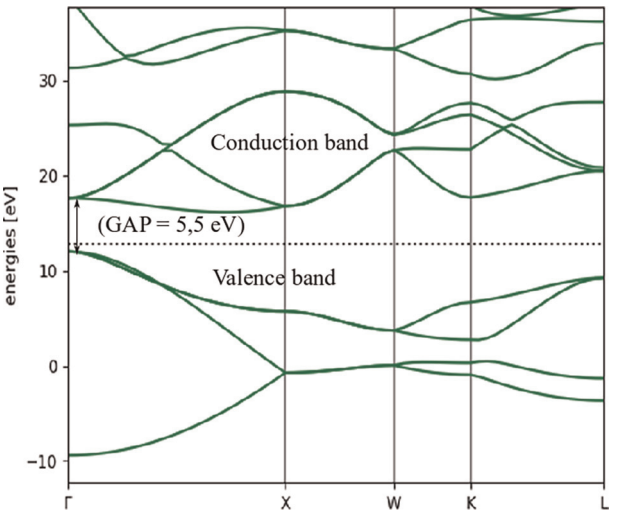

Figure 3.
Band structure of diamond.

512 k-points: 8 × 8 × 8 Monkhorst-Pack grid, 60 k-dots in the irreducible part of the Brillouin zone and Coarse grid: 12 × 12 × 12 grid as well as the fine grid: 24 × 24 × 24 grid. The ordinate axis represents the energy in (eV). It is clear from **Figure 3** that diamond is an insulator with a non-zero band gap since the valence and conduction bands do not meet at the k-point. This corresponds to a zero density of state when plotting the density of state as a function of energy. The band structure is then characterized by a nonlinear dispersion of the bands in the vicinity of the Fermi energy, whereas in graphene, for example, there is a linear dispersion of the bands in the vicinity of the Fermi energy [7].

Next, we calculated the electronic band structure of diamond along the high-symmetry directions in the Brillouin zone [18]. Appendix 1 lists the calculation steps.

First, we performed a standard ground state calculation and saved the results in a . gpw file. As we are dealing with a small bulk system, the plane-wave mode is the most appropriate here.

Next, we calculated the eigenvalues along a high-symmetry path in the Brillouin zone `kpts={'path': 'GXWKL', 'npoints': 60}`.

See `ase.dft.kpoints.special_points` for the definition of the special points for a face-centered cubic (FCC) lattice.

For the band structure calculation, we fixed the density to the previously calculated ground state density, and as we wanted to calculate all k-points, we did not use symmetry (`symmetry='off'`).

Finally, we platted the band structure using ASE's band-structure tool (`ase.spectrum.band_structure.BandStructure`):

3.3 Density of state of diamond

As mentioned, the lattice constant used for the calculations is a = 3.57 Å, and the void used in the three-dimensional (3D) structures along the axes is equal to 0 Å.

The convergence criteria used imply a total energy change of 0.0005 eV/electron, a maximum integral of absolute density change of 0.0001 electrons, and a maximum integral of absolute eigenstate change of 4.10^{-8} $(eV)^2$. We also used an $8 \times 8 \times 8$ Monkhorst-Pack grid and 512 k-points in the irreducible part of the Brillouin zone. In addition, the following parameters were considered:

- Densities: coarse grid: $12 \times 12 \times 12$ grid
- Fine grid: $24 \times 24 \times 24$ grid;
- Total loading: 0.000000;
- Density mixing: method (separate);
- Backend (pulay);
- Linear mixing parameter (0.05);
- Mixing with 5 old densities and damping of long-wave oscillations (50)
- Hamiltonian: XC and Coulomb potentials evaluated on a $24 \times 24 \times 24$ grid using the PBE EC function; number of atoms (2);
- Number of atomic orbitals (8);
- Number of bands in the calculation (8);
- Number of valence electrons (8).

After initialization and convergence of the graphene structure, we obtained the following results (see **Table 4**):

Figure 4 plots the density of state obtained from this calculation. The calculated electronic density of state shows that diamond is a semi-metal with a non-zero gap E_g equal to 5.5 eV, which is in agreement with other calculations [19]. The electronic spectrum near the Fermi energy has a linear form. This behavior allows diamond to

Kinetic	+16.220681 eV
Potential	−15.352109 eV
External	+0.000000 eV
XC	−19.079831 eV
Entropy (-ST)	−0.000000 eV
Local	+0.041249 eV
=	
Free energy	−18.170010 eV
Extrapolated	−18.170010 eV

Table 4.
Results obtained after initialization and convergence of the graphene structure.

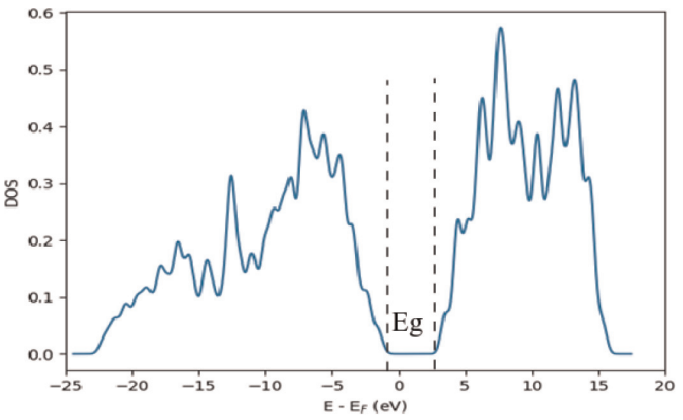

Figure 4.
Density of state (DOS) of diamond.

offer many applications in biosensors [20] and in devices for power electronics [21], because electrons have a high mobility in diamond at Dirac point of 4500 $cm^2\ V^{-1}\ s^{-1}$. Diamond is a wide-band-gap isolator. It is intrinsically insulating but can become semiconductor, then metallic and superconductor if it is suitably doped. This doping, which can be of type n or p, is obtained by the substitution of a carbon atom by a donor (n) or acceptor (p) atom, respectively.

3.4 PBE0 and PBE calculations for diamond

PBE is a GGA function introduced by Perdew, Burke, and Ernzerhof, in which all parameters other than those of its local spin density component are fundamental constants [22, 23]. Adamo and Barone [24] realized a new hybrid Hartree–Fock /DFT model derived from the PBE GGA, called PBE0, in which the HF exchange contribution is also fixed *a priori* [24]. The PBE0 approach is obtained by casting the PBE function in a hybrid scheme, in which the HF ratio is fixed a priori. The integer function can be expressed as follows:

$$E_{xc}^{PBE0} = E_{xc}^{PBE} + \frac{1}{4}\left(E_x^{HF} - E_x^{PBE}\right) \quad (1)$$

Where E_{xc}^{PBE} and E_x^{PBE} are the correlation and GGA exchange contributions, respectively, and $E_x^{HF}$is the HF exchange [25]. It can be interesting to examine the two approaches of PBE and PBE0 to determine the lattice constant of diamond as well as its gap value.

3.4.1 Diamond lattice constant as a function of the number of k-points

In this section, we perform a non-self-consistent PBE0 calculation based on a self-consistent PBE to represent the variation of the diamond lattice constant as a function of k-point number.

We use a Monkhorst-Pack k-point grid [26], which is essentially a uniformly spaced grid in the Brillouin zone. Another less commonly used scheme is the Chadi-Cohen k-point grid [27, 28]. Monkhorst-Pack grids are specified as n1 × n2 × n3 grids,

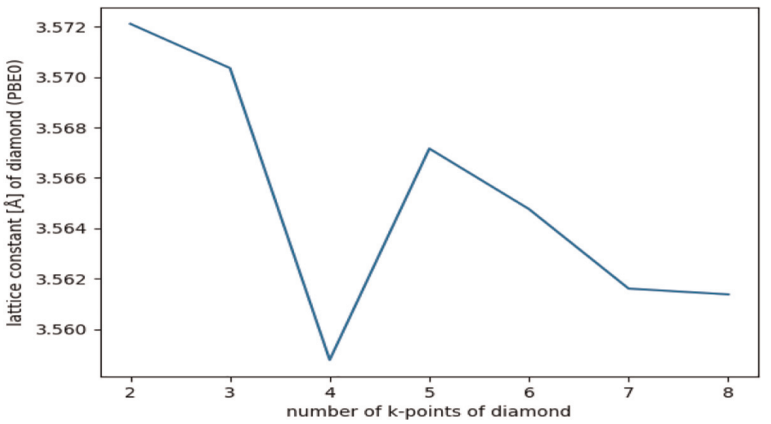

Figure 5.
Calculation of the diamond lattice constant in the case of PBE0.

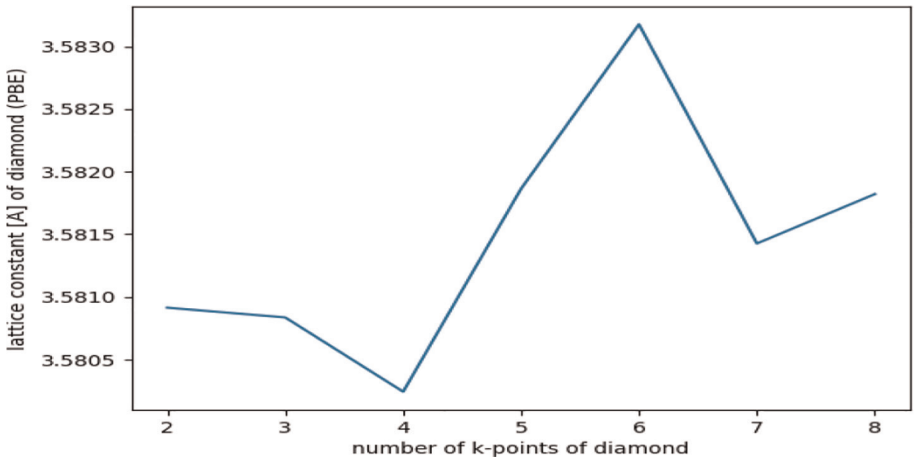

Figure 6.
Calculation of the diamond lattice constant in the case of PBE.

and the total number of k-points is n1-n2-n3. The computational cost is linear with respect to the total number of k-points, so a computation on a $4 \times 4 \times 4$ grid will be about 8 times more expensive than that on a $2 \times 2 \times 2$ grid. Therefore, we again seek to strike a balance between convergence and ease of computation [28]. Below we examine the k-point convergence of diamond carbon. **Figure 5** presents the results of the PBE0 calculation, **Figure 6** presents the results of the PBE calculation, and **Figure 7** presents the results of the PBE0 and PBE calculation.

To plot the three figures, we need a grid of at least $8 \times 8 \times 8$ k-points to achieve a convergence level of at least 0.002 Å for PBE0 and 0.0005 Å for PBE. We find a lattice constant between 3.560 and 3.562 Å in the case of PBE0 and between 3.5815 and 3.5820 Å in the case of PBE. PBE and PBE0 do not converge to the same lattice constant, so they do not give the same results. PBE0 was found to perform better than the PBE function in reproducing the experimentally found geometric features (a = 3.567 Å) [29].

The convergence of the k-points is not always monotonic as in this example, and sometimes very dense grids (e.g., up to $20 \times 20 \times 20$) are required for highly

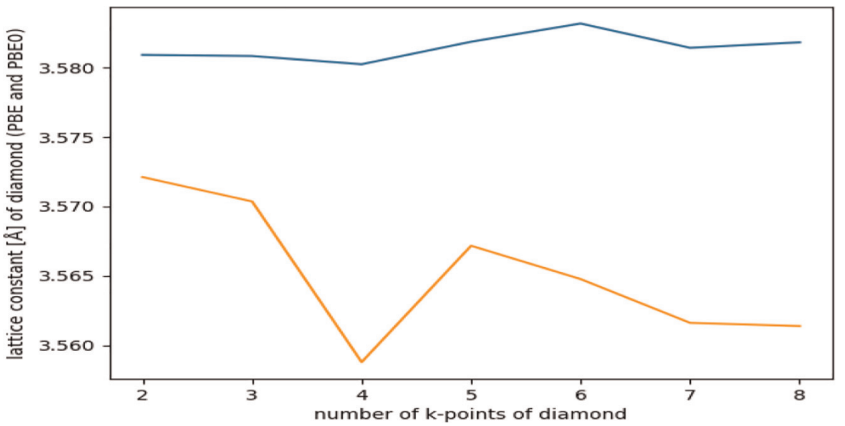

Figure 7.
Calculation of the diamond lattice constant in the case of PBE0 and PBE.

k -points	PBE(Γ- Γ)	PBE(Γ-X)	PBE0(Γ- Γ)	PBE0(Γ-X)
2	5.003	2.996	7.653	5.368
4	5.099	3.133	7.184	5.005
6	5.109	3.151	7.102	4.937
8	5.108	3.147	7.080	4.913

Table 5.
Resulting Γ- Γ and Γ-X gaps obtained for PBE and PBE0 in eV.

convergent properties such as the density of states in smaller unit cells. Oscillations in the lattice constant are typical, and it can be difficult to achieve high levels of convergence. Best practice is to use the same k-point sampling grid in the calculations when possible and dense (high number of k-points) otherwise. It is important to verify convergence in these cases. The larger the unit cells, the smaller the number of k-points required. For example, if a 1 × 1 × 1 fcc unit cell shows convergent results in a 12 × 12 × 12 k-point grid, then a 2 × 2 × 2 fcc unit cell would show the same level of convergence with a 6 × 6 × 6 k-point grid. In other words, doubling the unit cell vectors results in a halving of the number of k-points [28].

Sometimes k-points are described as k-points per reciprocal atom. For example, a 12 × 12 × 12 k-point grid for a primitive fcc unit cell corresponds to 1728 k-points per reciprocal atom. A 2 × 2 × 2 fcc unit cell has eight atoms (i.e., 0.125 reciprocal atoms), and thus, a 6 × 6 × 6 k-point grid has 216 k-points, (216/0.125 = 1728 k-points per reciprocal atom) [28].

In this k-point convergence study, we use an 8 × 8 × 8 k-point grid on a unit cell containing two atoms, resulting in 1024 k-points per reciprocal atom.

3.4.2 PBE and PBE0 diamond bands

In this section, we present the calculation of band gap width of diamond, using the PBE and PBE0 calculation. We use an 8 × 8 × 8 Monkhorst-Pack grid (resolution of 512 k-points and 29 k-points in the irreducible part of the Brillouin zone). **Table 5** presents the resulting Γ- Γ and Γ-X gaps obtained for PBE and PBE0 in eV:

4. Conclusions

We have presented here a study of the electronic properties of diamond carbon, namely the band structure and the density of states. These calculations were based on the GPAW and ASE methods. The GPAW code is built on top of the ASE, which is a set of Python modules, and designed to facilitate the configuration, execution, and analysis of atomic/electronic calculations. We performed a comparative study of PBE and PBE0 approximations on lattice constant and diamond gap calculations. Regarding the lattice constant of diamond, we were able to reproduce the experimental value to within 0.2% for PBE0 and within 0.4% for PBE. We also calculated the diamond gap and found that our results are comparable with other experimental and theoretical results. Results show that the hybrid PBE0 was performed better than PBE in reproducing the geometrical and electronic characteristics of diamond. We also optimized diamond structure and found that the calculated band structure and density of states were in agreement with other methods. This chapter provided information for the theoretical and experimental communities working on electronic properties of diamond, which is considered one of the most promising materials for the integrated electronic and photonic, radio, optoelectronic, and quantum device industry.

A. Python code used to calculated

```
from ase.build import bulk
from gpaw import GPAW, PW, FermiDirac
# Perform standard ground state calculation (with plane wave basis)
c = bulk('C', 'diamond', 3.57)
calc = GPAW(mode=PW(500),
      xc='PBE',
kpts=(8, 8, 8),
    random=True, # random guess (needed if many empty bands required)
occupations=FermiDirac(0.01),
txt='Cd_gs.txt')
c.calc = calc
c.get_potential_energy()
calc.write('Cd_gs.gpw')
# Restart from ground state and fix potential:
calc = GPAW('Cd_gs.gpw',
 nbands=16,
 fixdensity=True,
      symmetry='off',
 kpts={'path': 'GXWKL', 'npoints': 60},
 convergence={'bands': 8})
calc.get_potential_energy()
# Plots the dispersion relationships
bs = calc.band_structure()
bs.plot(filename='bandstructure-diamond.png', show=True, emin=-25, emax=25.0)
plt.savefig('bandstructure-diamond.png')
plt.show ()
```

References

[1] Hermann S. Growth of carbon nanotubes on different substrates/ catalysts for advanced interconnects in integrated circuits [thesis]. 2011

[2] Stanislaus, Okwundu O, Aniekwe EU, Nwanno CE. Unlimited potentialsof carbon: different structures and uses (a review). Metallic Materials. Engineering. 2018;**24**(3):145-171. DOI: 10.30544/388

[3] Geim A, Novoselov K. The rise of graphene. Nature Materials. 2007;**6**:183. DOI: 10.1038/nmat1849

[4] Saito R, Dresselhaus G, Dresselhaus MS. Physical Properties of Carbon Nanotubes. London: Imperial College Press; 1998

[5] Shanan Abed M.. Preparation and characterization of carbon nanotubes composite [thesis]. 2014. DOI: 10.13140/ RG.2.2.32922.18883

[6] Candice B. Development of diamond photonic crystals: Modeling, technology and application to biosensing [thesis]. In: Institute of Fundamental Electronics - CNRS UMR 8622. Paris-Sud University; 2015

[7] Sellam A, Heyd R, Hlil EK, Koumina A, Hadaoui A. Ab initio studies of the electronic structure induced by the CO and N_2 adsorptions on graphene and on graphite slab. Materials Today: Proceedings. 2022;**62**:6287-6297. DOI: 10.1016/j.matpr.2022.03.354

[8] Sellam A, Hlil e K, Heyd R, Koumin A. An ab initio investigation of the electronic and magnetic properties of graphite and nickel-doped graphite. European Physical Journal Applied Physics. 2021;**94**:10401. DOI: 10.1051/ epjap/2021200217

[9] Berger C, Song ZM, Li TB, Li XB, Ogbazghi AY, Feng R, et al. Ultrathin epitaxial graphite: 2D electron gas properties and a route toward graphene-based nanoelectronics. The Journal of Physical Chemistry. B. 2004; **108**(52):19912-19916. DOI: 10. 1021/ jp040650f

[10] Li XS, Cai WW, An JH, Kim S, Nah J, Yang DX, et al. Large-area synthesis of high-quality and uniform graphene films on copper foils. Science. 2009;**324**(5932):1312-1314. DOI: 10.1126/science.1171245

[11] Stankovich S, Dikin DA, Dommett GHB, Kohlhaas KM, Zimney EJ, Stach EA, et al. Graphene-based composite materials. Nature. 2006;**442**:282-286. DOI: 10.1038/ nature04969

[12] Watcharotone S, Dikin DA, Stankovich S, Piner R, Jung I, Dommett GHB, et al. Graphene-silica composite thin films as transparent conductors. Nano Letters. 2007;**7**: 1888-1892

[13] Morozov SV, Novoselov KS, Katsnelson MI, Schedin F, Elias DC, Jaszczak JA, et al. Giant intrinsic carrier mobilities in graphene and its bilayer. Physical Review Letters. 2008;**100**: 016602. DOI: 10.1103/ PhysRevLett.100.016602

[14] Dikin DA, Stankovich S, Zimney EJ, Piner RD, Dommett GHB, Evmenenko G, et al. Preparation and characterization of graphene oxide paper. Nature. 2007;**448**:457-460. DOI: 10.138/nature06016

[15] Wallace PR. The band theory of graphite. Physics Review. 1947;**71**:622

[16] Castro Neto AH, Peres NMR, Novoselov KS, Geim AK. The electronic properties of graphene. Reviews of Modern Physics. 2009;**81**:109″U162

[17] Velez E. Graphene epitaxial on SiC (dopingand functionalization) [thesis]. University Pierreet Marie Curie Paris, VI, France. NNT: 2014PA066449. 2014. Available from: https://tel.archivesouvertes.fr [Accessed: 7 March 2015]

[18] Available from: https://wiki.fysik.dtu.dk/gpaw/tutorialsexercises/electronic/bandstructures/bandstructures.html#bandstructures

[19] Djafari Rouhani M, Lannoo M, Lenglart P. Electronic states of the neutral gap in covalent diamond solids. Journal de Physique. 1970;**31**:597. DOI: 10.1051/jphys:01970003107059700

[20] Ruffinatto S. Carbon nanotubes brown on diamond, new composite material for bioelectronic [Theses]. Universite de Grenoble. 2012 . (Cite en page 3)

[21] Nebel CE, Rezek B, Shin D, Uetsuka H, Yang N. Diamond for biosensor applications. Journal of Physics D: Applied Physics. 2007;**40**(20):6443. (Cite en page 3)

[22] Perdew JP, Burke K, Ernzerhof M. Generalized Gradient Approximation Made Simple. Physical Review Letters. 1996;**77**:3865

[23] Perdew JP, Burke K, Ernzerhof M. Generalized Gradient Approximation Made Simple. Physical Review Letters. 1997;**78**:1396

[24] Adamo C, Barone V. Toward reliable density functional methods without adjustable parameters: The PBE0 model. The Journal of Chemical Physics. 1999; **110**:6158

[25] Vetere V, Adamo C, Maldivi P. Performance of the 'parameter free' PBE0 functional for the modeling of molecular properties of heavy metals. Chemical Physics Letters. 2000;**325**(29): 99-105

[26] Monkhorst HJ, Pack JD. Special points for brillouin-zone integrations. Physical Review B. 1976;**13**:5188-5192. DOI: 10.1103/PhysRevB.13.5188

[27] Chadi DJ, Cohen ML. Special points in the brillouin zone. Physical Review B. 1973;**8**:5747-5753. DOI: 10.1103/PhysRevB.8.5747

[28] Kitchin J. Modeling materials using density functional theory (2012–2016). GNU Free Documentation License Version 1.3. 2008. p. 87

[29] Donohue J. The Structure of Elements. New York: Wiley; 1974